Uncertainty quantification tools for multiphase gas-solid flow simulations using MFIX

by

Xiaofei Hu

A dissertation submitted to the graduate faculty

in partial fulfillment of the requirements for the degree of

DOCTOR OF PHILOSOPHY

Major: Chemical Engineering

Program of Study Committee:

Rodney O. Fox, Co-major professor

Alberto Passalacqua, Co-major professor

Baskar Ganapathysubramanian

James C. Hill

R. Dennis Vigil

Iowa State University

Ames, Iowa

2014

TABLE OF CONTENTS

LIST OF TABLES

LIST OF FIGURES

ACKNOWLEDGEMENTS

I would like to take this opportunity to express my gratefulness to those who helped me conducting research and preparing this dissertation during these years. First of all, my sincerest gratitude to my major professor, Dr. Rodney O. Fox for his guidance and support. His insights and knowledge inspired me often. His trust and support gave me an opportunity to continue to do the research I like. His passion for science and his serious scientific attitude influenced me very much not only throughout these years but also in my future. Next, my deepest thankfulness to my co-advisor, Dr. Alberto Passalacqua for his patience and encouragements since I joined the group. His guidance helped me start quickly and smoothly on this project. His encouragements and support gave me strength and confidence to accomplish tough tasks and to complete my Ph.D. program. Then I would like to thank my committee members for their efforts: Dr. James C. Hill, Dr. R. Dennis Vigil, and Dr. Baskar Ganapathysubramanian. Next, I would also like to thank my group members and colleagues for their help: Dr. Bo Kong, Dr. Wei Bai, Dr. Yanxiang Shi, Dr. Cansheng Yuan, Michael Baker, Ehsan Madadi Kandjani, Nithin Somalatha Panicker, Xi Gao, and Zhenping Liu. Lastly, I would like to acknowledge the financial support from the U. S. Department of Energy. This work has been supported by the University Coal Research Program (UCR) of the U. S. Department of Energy under the award number DOE-UCR DE-FE0006946.

I would also like to take this chance to express my love to my family and friends. To my family, especially to my parents, for their unconditional love. They were always giving me hope and supporting me no matter what situation I was in or what decision I made. Then to my dearest friends for our invaluable friendship. They helped me become a better person. Their encouragements and supports were so precious especially when I was in hard times. Without them, I would not have the chance to describe how grateful I am here.

ABSTRACT

Computational fluid dynamics (CFD) has been widely studied and used in the scientific community and in the industry. Various models were proposed to solve problems in different areas. However, all models deviate from reality. Uncertainty quantification (UQ) process evaluates the overall uncertainties associated with the prediction of quantities of interest. In particular it studies the propagation of input uncertainties to the outputs of the models so that confidence intervals can be provided for the simulation results. In the present work, a non-intrusive quadrature-based uncertainty quantification (QBUQ) approach is proposed. The probability distribution function (PDF) of the system response can be then reconstructed using extended quadrature method of moments (EQMOM) and extended conditional quadrature method of moments (ECQMOM). The method is first illustrated considering two examples: a developing flow in a channel with uncertain viscosity, and an oblique shock problem with uncertain upstream Mach number. The error in the prediction of the moment response is studied as a function of the number of samples, and the accuracy of the moments required to reconstruct the PDF of the system response is discussed. The approach proposed in this work is then demonstrated by considering a bubbling fluidized bed as example application. The mean particle size is assumed to be the uncertain input parameter. The system is simulated with a standard two-fluid model with kinetic theory closures for the particulate phase implemented into MFIX. The effect of uncertainty on the disperse-phase volume fraction, on the phase velocities and on the pressure drop inside the fluidized bed are examined, and the reconstructed PDFs are provided for the three quantities studied. Then the approach is applied to a bubbling fluidized bed with two uncertain parameters. Contour plots of the mean and standard deviation of solid volume fraction, solid phase velocities and gas pressure are provided. The PDFs of the response are reconstructed using EQMOM with appropriate kernel density functions. The simulation results are compared to experimental data provided by the 2013 NETL small-scale

challenge problem. Lastly, the proposed procedure is demonstrated by considering a riser of a circulating fluidized bed as an example application. The mean particle size is considered to be the uncertain input parameters. Contour plots of the mean and standard deviation of solid volume fraction, solid phase velocities, and granular temperature are provided. Mean values and confidence intervals of the quantities of interest are compared to the experiment results. The univariate and bivariate PDF reconstructions of the system response are performed using EQMOM and ECQMOM.

CHAPTER 1. INTRODUCTION AND LITERATURE REVIEW

1.1 Introduction

Computational fluid dynamics (CFD) has been widely studied and used in the scientific community and in the industry. Various models were proposed to solve problems in different areas. However, all models deviate from reality. Sources of discrepancy between simulations and reality can be divided into three categories [16, 58]: assumptions and simplifications made to derive a mathematical model that represents the reality, numerical errors introduced by solving the mathematical models numerically, and uncertain model input parameters that specify the physical characteristics of the simulated system, such as geometry of the system, initial and boundary conditions, and other key parameters that control the system. It is therefore important to study the differences between simulations and reality to make the computational approaches reliable. Code and solution verifications ensure the correct numerical algorithm is used to relatively accurately solve the mathematical equations [16, 94]. Validation process makes the models represent the true physical system [16, 94]. In CFD simulations, the simulation process is deterministic [24]. Mean values of uncertain input parameters are often used so that a single-point estimation is given as the output of the simulation, which is used for design or optimization of the system. Confidence intervals are not always provided for the simulation results [31]. It is thus necessary to study the effects of uncertain inputs on the simulation results. Uncertainty quantification (UQ) process evaluates the overall uncertainties associated with the prediction of quantities of interest. In particular it studies the propagation of input uncertainties to the outputs of the models [16]. The uncertainty in input parameters can be caused by difficulties in measurements of experimental data, inherent variability of the system, and lack of knowledge of the system [58], and can be divided into two categories: aleatory

uncertainty which arises from randomness in model parameters, and epistemic uncertainty due to lack of knowledge of the system [16, 24]. The uncertainty in the UQ study refers to aleatory uncertainty. Many UQ approaches, including polynomial chaos (PC), moment methods, and Monte Carlo methods have been applied to single phase CFD simulations [24, 50, 58, 73]. However, applications of UQ approaches to multiphase CFD simulations are very limited. Although applications of UQ approaches to flows in porous media are reported in literature [36,37,63], for more complex systems such as gas-solid flows, few works can be found [20,30–32,52]. The objectives of this project are to develop a non-intrusive quadrature-based uncertainty quantification (QBUQ) approach, and to apply it to multiphase gas-solid flow simulations.

The outline of this dissertation is as follows. Section 1.2 of Chapter 1 provides the literature review on theory of UQ approaches and applications of UQ to single phase and multiphase CFD simulations. Chapter 2 describes the QBUQ approach in detail. The approach is then tested on a developed channel flow with uncertain viscosity and an oblique shock problem with uncertain inlet Mach number. Chapter 3 discusses the implementation of the QBUQ approach into MFIX and the application of the QBUQ approach to a bubbling fluidized bed with uncertain particle size. Chapter 4 applies the QBUQ approach to a bubbling fluidized bed with two independent uncertain parameters, and compares the results with experimental data provided by the 2013 NETL small-scale challenge problem. Chapter 5 discusses the application of the QBUQ approach to a riser of a circulating fluidized bed with uncertain particle diameter. In the end, Chapter 6 summarizes the work and gives an outlook on future work.

1.2 Literature Review

In this dissertation, uncertainty quantification refers to the study of the propagation of input uncertainties to the outputs of the models. The uncertainty in the input parameters refers to aleatory uncertainty, and can be described in three ways, shown in Fig. 1.1 [24].

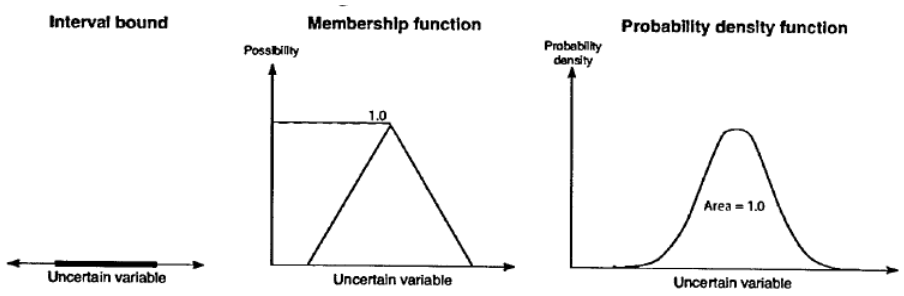

Figure 1.1 Three different ways to describe uncertainty of parameters [24].

The simplest way is to give upper and lower limit of the variable. Another way is to define a membership function on the uncertain variable, treated as a fuzzy set. Non-probabilistic UQ methods can be used if the uncertain parameters are described in these two ways, which are not discussed here. Probabilistic UQ approaches on which this work focuses are used when probability distribution function (PDF) of the uncertain parameters are defined.

1.2.1 Theory of uncertainty quantification

To illustrate the following methods, a random process $\kappa(\boldsymbol{\xi})$ with N random variables $\boldsymbol{\xi}$ is considered. A probability space $\mathcal{P}(\Omega, \mathfrak{F}, P)$ is defined by a sample space Ω, a sigma-algebra $\mathfrak{F}$ which is a non-empty collection of subsets of Ω, and a probability measure P on $(\Omega, \mathfrak{F})$.

1.2.1.1 Monte Carlo Methods

The basic idea of Monte Carlo methods is to generate a set of random realizations of the input variables $\boldsymbol{\xi}$, obtain the deterministic system response of the simulation for each sample κ_i $(i = 1, 2, \ldots, N)$, and evaluate the statistics of the response such as mean, variance, skewness, and kurtosis based on the solution set [24, 58, 109]. The convergence of Monte Carlo methods is independent of the dimensionality of the random variables, which is an advantage for problems with a large number of random input parameters. However, the convergence of the high order moments of Monte Carlo method is slow with respect to the number of samples, for instance the convergence of the standard deviation of the mean scales with $N^{-1/2}$. Therefore, a large number of samples may be required to achieve a given accuracy. Improvements to

the basic Monte Carlo methods are reported in the literature to reduce the required number of samples, including importance sampling Monte Carlo method [24], Latin hypercube Monte Carlo method [24, 58, 70], and quasi Monte Carlo method [58, 72]. In Walters and Huyse [109], the basic Monte Carlo method is tested on some simple CFD cases.

1.2.1.2 Moment methods

The foundation of moment methods is to write the moments of the simulation outputs as truncated Taylor series expansions about the mean value of the input parameters $\bar{\boldsymbol{\xi}}$ [24, 109]. Here approaches to obtain mean (μ) and variance (σ^2) of the system response at first-order and second-order accuracy are explained for one input parameter ξ. Extension to multi-variate problems is discussed later.

First-order, first moment (FOFM)

The first-order accurate estimation of the mean value of the response is actually the deterministic output of the simulation performed using the mean value of the uncertain input parameter $\bar{\xi}$, written as

$$\mu[\kappa(\xi)] = \kappa(\bar{\xi}). \tag{1.1}$$

Second-order, first moment (SOFM)

The second-order accurate estimation of the mean of the output requires an addition of a second derivative term, whose effect sometimes can be significant [24, 109].

$$\mu[\kappa(\xi)] = \kappa(\bar{\xi}) + \frac{1}{2}\sigma^2(\xi)\left.\frac{\partial^2\kappa}{\partial\xi^2}\right|_{\bar{\xi}}. \tag{1.2}$$

First-order, second moment (FOSM)

The variance of the output at first-order accuracy can be obtained by multiplying the variance of the input with a first derivative term,

$$\sigma^2[\kappa(\xi)] = \sigma^2(\xi)\left(\left.\frac{\partial\kappa}{\partial\xi}\right|_{\bar{\xi}}\right)^2. \tag{1.3}$$

Second-order, second moment (SOSM)

The second-order accurate estimation of the variance of the output also has a correction term related to the second derivative,

$$\sigma^2[\kappa(\xi)] = \sigma^2(\xi)\left(\left.\frac{\partial\kappa}{\partial\xi}\right|_{\bar{\xi}}\right)^2 + \frac{1}{2}\left[\sigma^2(\xi)\left.\frac{\partial^2\kappa}{\partial\xi^2}\right|_{\bar{\xi}}\right]^2. \tag{1.4}$$

Extension to multiple random variables

The extension of the method to multi-variate problems is straightforward with Taylor series expansions. In Walters and Huyse [109], mean and variance of the system response at first-order accuracy for a bivariate case ($\kappa(\boldsymbol{\xi}) = \kappa(\xi_1, \xi_2)$) are given as:

$$\mu[\kappa(\xi_1, \xi_2)] = \kappa(\bar{\xi_1}, \bar{\xi_2}), \tag{1.5}$$

$$\sigma^2[\kappa(\xi_1, \xi_2)] = \sigma^2(\xi_1)\left(\left.\frac{\partial\kappa}{\partial\xi_1}\right|_{\bar{\boldsymbol{\xi}}}\right)^2 + \sigma^2(\xi_2)\left(\left.\frac{\partial\kappa}{\partial\xi_2}\right|_{\bar{\boldsymbol{\xi}}}\right)^2 + 2\left(\left.\frac{\partial\kappa}{\partial\xi_1}\right|_{\bar{\boldsymbol{\xi}}}\right)\left(\left.\frac{\partial\kappa}{\partial\xi_2}\right|_{\bar{\boldsymbol{\xi}}}\right)\sigma_{12}(\xi_1, \xi_2), \tag{1.6}$$

where $\sigma_{12}(\xi_1, \xi_2)$ is the covariance defined as

$$\sigma_{12}(\xi_1, \xi_2) = \mu[\xi_1\xi_2 - \mu(\xi_1)\mu(\xi_2)]. \tag{1.7}$$

Since higher order moments are neglected in the moment methods, for input parameters with PDF deviating far from Gaussian distribution, the methods are no longer appropriate [24]. Applications of the moment methods to CFD simulations are reported in [47, 48, 89, 103, 109].

1.2.1.3 Polynomial chaos methods

The polynomial chaos (PC) UQ approach is a type of spectral method [58]. It estimates the system response with a truncated series,

$$\kappa(\boldsymbol{\xi}) = \sum_{i=0}^{\infty}\kappa_i\Psi_i(\boldsymbol{\xi}) \approx \sum_{i=0}^{Q}\kappa_i\Psi_i(\boldsymbol{\xi}), \tag{1.8}$$

where deterministic coefficients κ_i are called PC coefficients, and $\Psi_i(\boldsymbol{\xi})$ are Hermite polynomials in basic PC expansions, and can be extended to a class of orthogonal polynomials in generalized PC (GPC) expansions developed by Xiu and Karniadakis [115], based on the Askey scheme [2]. The PC coefficients κ_i can be determined as

$$\kappa_i = \frac{\langle\kappa(\boldsymbol{\xi}), \Psi_i(\boldsymbol{\xi})\rangle}{\langle\Psi_i(\boldsymbol{\xi}), \Psi_i(\boldsymbol{\xi})\rangle}, \tag{1.9}$$

where the inner product $\langle a, b\rangle$ with respect to the probability measure $p(\boldsymbol{\xi})$ is defined as

$$\langle a(\boldsymbol{\xi}), b(\boldsymbol{\xi})\rangle = \int_{\Omega} a(\boldsymbol{\xi}) b(\boldsymbol{\xi}) p(\boldsymbol{\xi}) \mathrm{d}\boldsymbol{\xi}. \tag{1.10}$$

With the PC coefficients κ_i, the statistics of the response $\kappa(\boldsymbol{\xi})$ can be determined [58]. In fact, the first coefficient κ_0 is the mean of the response. The variance of the response is calculated as

$$\sigma^2[\kappa(\boldsymbol{\xi})] = \sum_{i=1}^{Q} \kappa_i^2 \langle \Psi_i^2 \rangle. \tag{1.11}$$

The PC UQ methods can be either intrusive or non-intrusive. The intrusive approach reformulates the governing equations using Galerkin projection while the non-intrusive approach treats the computational model as a black box, and determines the PC coefficients involving different sampling strategies [73].

Intrusive approaches

The intrusive approaches determine the PC coefficients κ_i using a Galerkin approach. The general idea of the method is summarized in [50] as follows. The governing equations of the random process $\kappa(\boldsymbol{\xi})$ are defined as

$$\mathcal{M}(\kappa(\boldsymbol{\xi}), \boldsymbol{\xi}) = 0, \tag{1.12}$$

where $\mathcal{M}$ is a non-linear operator. The idea of the approach is to introduce the PC expansions of $\kappa(\boldsymbol{\xi})$ shown in Eq. 1.8 into the governing equations Eq. 1.12, then orthogonally project the reformulated equations onto the expansion basis:

$$\left\langle \mathcal{M}\left(\sum_{i=0}^{Q} \kappa_i \Psi_i(\boldsymbol{\xi}), \boldsymbol{\xi}\right), \Psi_j \right\rangle = 0, \quad j = 0, 1, \ldots, P. \tag{1.13}$$

The solutions of the system shown in Eq. 1.13 are the PC coefficients. Details on applying the method to different mathematical problems are described in [58].

Intrusive approaches are computationally efficient because only one set of mathematical problems needs to be solved, and have been applied to CFD simulations with reasonable complexity [50, 58, 73]. However, since it needs modifications to the computational models, for complex systems, the intrusive approach is challenging to implement.

Non-intrusive approaches

The procedure of non-intrusive PC UQ approaches is summarized in [73] as follows.

1. Generate n samples of $\boldsymbol{\xi}$, $\{\boldsymbol{\xi}^j\}_{j=1}^n$, using the selected sampling strategy.
2. Obtain simulation output κ^j for each sample $\boldsymbol{\xi}^j$.
3. Calculate PC coefficients κ_i explicitly using Eq. 1.9.
4. Write the system response κ in the series form $\kappa = \sum_{i=0}^{Q} \kappa_i \Psi_i(\boldsymbol{\xi})$ using the PC coefficients obtained in step 3.

The computational cost of the approach depends on the number of samples since for each sample the simulation is performed once. Therefore, an effective sampling strategy is crucial for non-intrusive UQ approach. Samples can be generated using random or deterministic sampling strategies.

Random sampling strategies use Monte Carlo based approaches to evaluate the inner product in Eq. 1.9. The method is discussed in Section 1.2.1.1 about its advantages and disadvantages. Applications of Monte Carlo method and Latin hypercube sampling with PC approach are reported in works done by Ghanem [35, 73], and Ghiocel and Ghanem [39, 73].

Deterministic sampling strategies, such as quadrature-based sampling strategy can significantly reduce the number of samples required to achieve the convergence of the moments of the system response [73]. For N independent random input parameters $\boldsymbol{\xi} = (\xi_1, \xi_2, \ldots, \xi_N)$, using N-dimensional Gaussian quadrature formulae with q quadrature nodes in each dimension, the PC coefficients κ_i can be calculated as

$$\kappa_i = \frac{1}{\langle \Psi_i^2 \rangle} \sum_{j_1=1}^{q} \cdots \sum_{j_N=1}^{q} \kappa(\xi_{j_1}, \ldots, \xi_{j_N}) \Psi_i(\xi_{j_1}, \ldots, \xi_{j_N}) \prod_{i=1}^{N} w_{j_i}, \tag{1.14}$$

where ξ_{j_i} and w_{j_i} are the j-th quadrature node and weight for parameter ξ_i. In Le Maître et al. [60], the non-intrusive PC UQ method using quadrature-based sampling is compared with intrusive PC UQ approach. Although this sampling strategy can reduce computational cost significantly, it becomes inefficient for problems with a high number of uncertain parameters because it suffers from the curse of dimensionality [58, 73]: the number of samples required increases exponentially with the number of the random input parameters. Improved approaches

can significantly reduce the number of samples required, including sparse grid approach proposed by Smolyak [58, 97] and adaptive sparse grid method [34, 58].

1.2.1.4 Stochastic collocation methods

Instead of estimating the Galerkin integrals to obtain PC coefficients, stochastic collocation methods rely on interpolation [58, 73]. In collocation method, the system response $\kappa(\boldsymbol{\xi})$ is approximated as $\tilde{\kappa}(\boldsymbol{\xi})$ with

$$\tilde{\kappa}\left(\boldsymbol{\xi}^{(i)}\right) = \kappa\left(\boldsymbol{\xi}^{(i)}\right), \quad 1 \leq i \leq m, \tag{1.15}$$

where $\boldsymbol{\xi}^{(i)}$ are the collocation points at which the approximation is exact. The approximated system response $\tilde{\kappa}(\boldsymbol{\xi})$ can be defined in terms of expansion as

$$\tilde{\kappa}(\boldsymbol{\xi}) = \sum_{i=1}^{m} \tilde{\kappa}_i \Phi_i(\boldsymbol{\xi}), \tag{1.16}$$

where the expansion coefficients $\tilde{\kappa}_i$ are determined by Eq. 1.15, and $\Phi_i(\boldsymbol{\xi})$ are the interpolation basis functions. The most popular choices of $\Phi_i(\boldsymbol{\xi})$ are based on polynomial interpolation [58]. Hosder et al. [46] apply the method to several CFD problems, using $P+1$ collocation points to determine $P+1$ expansion coefficients by solving a linear system of equations with Hermite polynomials as the basis functions.

The computational cost of stochastic collocation methods scales with the number of collocation points. Sparse grid methods can be used to reduce the number of collocation points required for problems with a large number of uncertain parameters [58]. Applications of sparse grid collocation methods are reported in [6, 67, 78, 111, 114], and some applications of adaptive approaches can be found in [27, 65, 76, 77].

1.2.1.5 Quadrature-based UQ methods

The UQ approach adopted in the present project is based on the direct quadrature method proposed by Yoon et al. [4, 119]. Moments of the system response are estimated directly using Gaussian quadrature formulae [42], instead of using PC expansions to represent the system response. With the set of moments, low order statistics of the response such as mean, variance,

skewness, and kurtosis can be calculated. In addition, the PDF of the system response can be reconstructed locally with the extended quadrature method of moments (EQMOM) [121] and the extended conditional quadrature method of moments (ECQMOM). The approach can be efficiently applied to problems with moderate number of uncertain parameters. With the reconstructed PDF of the system response, the probability of critical events can be evaluated, which is the key advantage of the method. In the following chapters, the method is discussed in detail, and applications of the method to simple CFD test cases, bubbling fluidized beds, and riser flows are presented.

1.2.2 Uncertainty quantification in computational fluid dynamics

Different UQ approaches discussed in above sections are applied to CFD simulations. Most of the applications of UQ analysis are to single phase CFD simulations. Applications of UQ approaches to multiphase CFD simulations are very limited. The following sections give some examples.

1.2.2.1 UQ in single phase CFD simulations

UQ approaches have been applied to various single phase flows, including compressible flows, incompressible flows, non-isothermal flows, and reacting flows. These applications are discussed below.

Compressible flows

Walters and Huyse [109] reviewed different UQ approaches such as Monte Carlo method, and moment methods. These approaches were implemented into several single phase CFD simulations, including an oblique shock wave problem with uncertain upstream Mach number and wedge angle, an expansion wave problem with uncertain upstream Mach number and the flow expansion angle, and a supersonic airfoil with uncertain thickness-to-chord ratio.

Mathelin et al. [69] applied the intrusive PC UQ approach to a flow in a quasi-one-dimensional nozzle with nozzle shape as the source of uncertainty. Results were compared with

those obtained by Monte Carlo methods. The method performed poorly for high non-linear cases, which made them develop a collocation method for complex non-linear problems [68].

Chen et al. [15] implemented an intrusive generalized PC UQ approach to an isentropic flow in a dual-throat nozzle with uncertain initial conditions. They discovered that the PC coefficients of the velocity field are smooth functions on spatial variable x, though the velocity field is discontinuous at the shock location. They concluded that the shock location can be predicted accurately when the variance of the uncertain initial condition is small. Otherwise, the convergence of the method is slow and many terms in the PC expansion are required.

Hosder et al. [46] applied a collocation method to an oblique shock problem, an expansion wave problem and a boundary layer problem. They used $P+1$ collocation points to determine $P+1$ expansion coefficients by solving a linear system of equations with Hermite polynomials as the basis functions.

Lockwood and Mavriplis [62] built a gradient-enhanced surrogate model to represent the relation between simulation outputs and input parameters. A Monte Carlo method was then applied for UQ analysis. The approach was applied to a hypersonic flow.

Incompressible flows

Le Maître et al. [56] first applied the intrusive PC UQ method to a 2D incompressible channel flow with uncertain viscosity. Results showed that a small number of terms in the PC expansion are required.

Xiu and Karniadakis [116] proposed the generalized PC UQ by using a class of orthogonal polynomials as basis functions. They applied the method to a channel flow with uncertain wall boundary conditions and a laminar flow around a circular cylinder with uncertain freestream condition.

Pereira et al. [85] applied the non-intrusive PC UQ approach on a blood flow in an idealized portal vein with uncertain blood viscosity. They concluded that a fast convergence can be obtained with second order polynomials because the contribution of the PC expansion mainly comes from the first term.

Non-isothermal flows

In Le Maître et al. [56], the intrusive PC UQ approach was also applied to a channel flow with uncertain viscosity caused by uncertain temperature, and the same channel flow evolving temperature field with uncertain inlet temperature. They extended the work to Rayleigh-Bénard flow in the Boussinesq limit, and found out the global PC expansion is not suitable for this case. Similar conclusions were reported in the work done by Asokan and Zabaras [3].

Wan and Karniadakis [110] proposed a multi-element generalized PC approach, and applied it to a heat transfer problem in a 2D channel. They concluded that the proposed local multi-element generalized PC approach is more efficient than the global generalized PC methods.

Reacting flows

Phenix et al. [87] first applied the PC UQ approach to a supercritical water hydrogen oxidation mechanism with uncertain reaction rate coefficients and species thermochemistry. Their results showed that compared with Monte Carlo method, PC UQ is more efficient, and second-order polynomials are enough to estimate the distributions of the response.

In Reagan et al. [91], a non-intrusive PC UQ approach was applied to two reaction cases: a homogeneous ignition studied in [87] previously, and flames in isothermal supercritical water oxidation. In their later work [92], Reagan et al. used PC to evaluate high-order sensitivities, providing confidence intervals for sensitivity coefficients.

Debusschere et al. [17] studied UQ on a electrochemical microchannel flow with protein labelling reactions. The system was relatively complex with coupled momentum equations, species conservation equations, and electrostatic field equations.

1.2.2.2 UQ in multiphase CFD simulations

UQ in multiphase flows was first proposed by Ghanem and Dham for flows in porous media [37] using Karhunen-Loève (KL) and PC expansions. The effect of uncertain hydraulic conductivity on the outputs was studied. This approach combined with Monte Carlo method was used by Ghanem [36] to study multiphase transport in random porous media. Lu and Zhang [63] studied the flows in heterogeneous porous media using three UQ approaches: Monte

Carlo method, moment methods, and moment-KL combined approach. The gain of efficiency with the proposed moment-KL approach was significant.

For much more complex multiphase flows, such as gas-solid multhiphase flows, the works reported are very limited. Gel et al. [31] built a surrogate model based on data-fitted response surface for a bubbling fluidized bed. Then forward propagation of input uncertainties was studied by using Monte Carlo method.

In another work done by Gel et al. [32], the uncertainty in the outputs of a circulating fluidized bed caused by spatial discretization, time averaging, uncertain input parameters, and surrogate model was studied. Results were shown in a probability box plot, which gave confidence intervals for the simulation outputs.

Gel et al. [30] constructed a surrogate model using an open source UQ toolbox, PSUADE, and then used a direct Monte Carlo-simulation-based approach to perform UQ analysis. The influences of heating rate, pressure, and temperature on coal devolatilization kinetics in gasifier modeling were studied.

In Donato and Pitchumani [20], a non-intrusive methodology called QUICKER was proposed. Five training points were chosen based on the distribution of the uncertain parameters. The output distribution was approximated by a modified lognormal distribution whose defining parameters were determined by the set of simulation results. The method was applied to a circulating fluidized bed and a turbulent fluidized bed.

Lane et al. [52] applied the statistical UQ approaches, such as sensitivity analysis and Bayesian calibration, to a bubbling fluidized bed with immersed horizontal tubes. Effects of six model parameters were studied, including particle-particle and particle-wall restitution coefficients, packed bed void fraction, friction angles for particle-particle and particle-wall interactions, and drag models.

CHAPTER 2. A QUADRATURE-BASED UNCERTAINTY QUANTIFICATION APPROACH WITH RECONSTRUCTION OF THE PROBABILITY DISTRIBUTION FUNCTION OF THE SYSTEM RESPONSE

Modified from a paper submitted to Computers and Fluids, 2014.

Xiaofei Hu, Alberto Passalacqua, Prakash Vedula, and Rodney O. Fox

A non-intrusive quadrature-based uncertainty quantification method is presented, which relies on Gaussian quadrature formulae to generate the set of samples and directly compute the approximated moments of the system response. These moments are used to reconstruct the distribution function of the values assumed by the system response, by means of the extended quadrature method of moments. The application of the method is then illustrated considering two examples: a developing flow in a channel with uncertain viscosity, and an oblique shock problem. The error in the prediction of the moment response is studied as a function of the number of samples, and the accuracy of the moments required to reconstruct the PDF of the system response is discussed.

2.1 Introduction

The quantification of uncertainty in computational fluid dynamics (CFD) has become of paramount importance due to the widespread adoption of CFD tools for design and optimization purposes in numerous fields of engineering. A number of applications of uncertainty quantification reported in the literature [56, 58, 60, 69, 73, 91, 94] rely on the polynomial chaos (PC) approach, where the random variables are represented as series of orthogonal polynomials.

However, when the objective of the uncertainty quantification (UQ) study is to evaluate the moments of the system response, such an approach can be replaced by the direct application of quadrature formulae, where the computational model becomes the integrand function [4, 119]. We propose here to use this approach to calculate the moments of the system response subject to uncertainty, and we illustrate a procedure to obtain a reconstructed form of the probability distribution function (PDF) of the system response from the computed moments. Such a distribution function allows the probability of critical events that may affect the system under consideration to be calculated, which is not possible with conventional UQ methods, since they do not provide direct access to the PDF of the system response.

Uncertainty quantification methods can be either intrusive or non-intrusive. The foundation of *intrusive* UQ methods is the introduction of the uncertainty directly into the computational model under consideration. This is typically achieved in the framework of the polynomial chaos (PC) methodology by reformulating the original model equations into equations for the strength of the modes of the polynomial chaos expansion [73]. While the intrusive approach is formally general, and computationally efficient, since it only requires the solution of one mathematical problem, the solution of the set of equations it originates can easily become challenging. In many practical applications it is then preferable to rely on *non-intrusive* methodologies, which perform the study of uncertainty propagation by computing the quantities of interest (modes of the PC expansion or moments of the system response) from the results of a set of multiple simulations performed using the original model. In this approach, the space of the uncertain input parameters of the model is sampled either with a statistical or deterministic sampling strategy, and samples are used to generate the set of simulations to be performed [58, 73]. It is clear that the key element of non-intrusive uncertainty quantification is the strategy used to sample the space of input parameters, in order to minimize the number of samples, without sacrificing the accuracy of the uncertainty propagation procedure. Samples can be generated using the Monte Carlo approach, which is convenient when the number of uncertain parameters of the model is large, but is also known for the slow convergence of the high-order moments as a function of the number of samples. Alternative strategies were developed to reduce the number of samples, like the Latin hypercube approach [73]. However these methods become

impractical for computationally intensive problems [73]. On the other hand, deterministic quadrature-based sampling strategies can significantly reduce the number of samples required to achieve convergence of the moments of the system response [73]. However, if the traditional Gauss quadrature approach is used, the number of samples required by these methods increases exponentially with the number of uncertain parameters, limiting the applicability of these methods to models with moderate dimensionality.

In this work we adopt the direct quadrature approach proposed in [4, 119], where moments of the system response are estimated directly using Gaussian quadrature formulae [42], rather than adopting the PC representation of the system response. This approach, which was shown by Yoon et al. [4,119] to be equivalent to stochastic collocation [26,67–69], significantly reduces the complexity of the procedure, and allows the number of samples required to predict the moments of a given order to be estimated based on assumptions on the functional order that correlates the uncertain input parameter and the output property of interest [4, 119]. The moments computed with the direct quadrature procedure can then be used to reconstruct the probability distribution function of the values of the model response. We achieve this result using the extended quadrature method of moments (EQMOM) [121], which allows the output PDF to be piecewise reconstructed using a basis of non-negative functions. EQMOM ensures that all the moments used to perform the reconstruction are reproduced correctly. Additionally, it presents key advantages with respect to other reconstruction methods based on entropy maximization [71, 101], which require the solution of multidimensional optimization problems of increasing difficulty for increasing number of moments. In this work we discuss in detail the case of β distributions. We then illustrate the proposed UQ procedure with reconstruction of the PDF of the response considering two example applications: a developing channel flow [56], and an oblique shock problem [46]. For each application, the convergence of the moments of the fluid velocity components (system response) is studied, the predicted system response obtained with the quadrature-based UQ approach is compared with the results predicted by the PC approach, and the PDF of the response is reconstructed at relevant locations of the computational domain.

2.2 Quadrature-Based Uncertainty Quantification Approach

The foundation of the quadrature-based uncertainty quantification approach consists in the direct evaluation of the moments of the system response by means of Gaussian quadrature formulae [4,119]. To illustrate the procedure, we consider a probability space $\mathcal{P}(\Omega, \mathfrak{F}, P)$ defined by a sample space Ω, a sigma-algebra $\mathfrak{F}$, and a probability measure P on $(\Omega, \mathfrak{F})$. We then define a set of N independent random variables $\boldsymbol{\xi}(\omega)$, being ω a random event. The n-th order moment of a random process $\kappa(\boldsymbol{\xi}, \mathbf{x})$ is defined as

$$m_n(\mathbf{x}) = \langle \kappa(\boldsymbol{\xi}, \mathbf{x})^n \rangle = \int_\Omega \kappa(\boldsymbol{\xi}, \mathbf{x})^n p(\boldsymbol{\xi}) \mathrm{d}\boldsymbol{\xi}, \tag{2.1}$$

where $p(\boldsymbol{\xi})$ depends on the probability measure P. In quadrature-based uncertainty quantification, the space Ω is sampled using Gaussian quadrature formulae [29], the computational model is evaluated in correspondence of each quadrature node, obtaining the corresponding abscissae, and the moments of the response are explicitly approximated in terms of the quadrature weights and abscissae. For sake of simplicity, in this chapter we limit the discussion to the one-dimensional case in terms of random variables, assuming N = 1. However, for generality of the formulation, we retain the dependency on the spatial coordinates. Under these assumptions, the integral in Eq. 2.1 can be approximated using a one-dimensional Gaussian quadrature formula with M nodes. Considering $p(\xi)$ as the weight function, the quadrature approximation of the moments is

$$m_n(\mathbf{x}) = \int_\Omega \kappa(\xi, \mathbf{x})^n p(\xi) \mathrm{d}\xi \approx \sum_{i=1}^{\mathrm{M}} w_i(\mathbf{x}) \kappa(\xi_i, \mathbf{x})^n, \tag{2.2}$$

being w_i the quadrature weights, ξ_i the quadrature nodes, and $\kappa(\xi_i, \mathbf{x})$ the corresponding abscissae.

Once the moments about the origin m_n are defined, it is possible to evaluate the conventional statistics of the response by converting them into central moments

$$\mu_n = \sum_{i=0}^{n} \binom{n}{i} (-1)^{n-i} m_i \mu^{n-i}, \tag{2.3}$$

being $\mu = m_1/m_0$ the mean. The variance is then given by

$$\sigma^2 = \frac{m_2}{m_0} - \mu^2, \tag{2.4}$$

while the skewness γ_1 and the kurtosis γ_2 are, respectively,

$$\gamma_1 = \frac{\mu_3}{\sigma^3} = \frac{m_3/m_0 - 3\mu m_2/m_0 + 2\mu^3}{\sigma^3}, \tag{2.5}$$

$$\gamma_2 = \frac{\mu_4}{\sigma^4} = \frac{m_4/m_0 - 4\mu m_3/m_0 + 6\mu^2 m_2/m_0 - 3\mu^4}{\sigma^4}. \tag{2.6}$$

In the next subsection we illustrate how to deal with the case of uniformly distributed random variables.

2.2.1 Uniformly distributed random variable

The case of a uniformly distributed random variable ξ leads to consider a distribution in the form

$$p(\xi) = \begin{cases} \frac{1}{b-a} & \xi \in [a, b], \\ 0 & \xi \in]-\infty, a[\bigcup]b, +\infty[. \end{cases} \tag{2.7}$$

In such a case, Eq. 2.2 leads to

$$m_n(\mathbf{x}) = \frac{1}{b-a} \int_a^b \kappa(\xi, \mathbf{x})^n \mathrm{d}\xi, \tag{2.8}$$

which can be calculated using a Gauss-Legendre quadrature formula, since the weight function is assumed to be the unit function. In order to use the well-known Gauss-Legendre quadrature, it is necessary to transform the interval $[a, b]$ into $[-1, 1]$, leading to

$$\begin{aligned} \int_a^b \kappa(\xi, \mathbf{x})^n \mathrm{d}\xi = \frac{b-a}{2} \int_{-1}^{1} \kappa \left(\frac{b-a}{2}\xi + \frac{a+b}{2}, \mathbf{x} \right)^n \mathrm{d}\xi \\ \approx \frac{b-a}{2} \sum_{i=1}^{\mathrm{M}} w_i(\mathbf{x}) \kappa \left(\frac{b-a}{2}\xi_i + \frac{a+b}{2}, \mathbf{x} \right)^n. \end{aligned} \tag{2.9}$$

Combining Eq. 2.9 and 2.8, we obtain the final result

$$m_n(\mathbf{x}) \approx \frac{1}{2}\sum_{i=1}^{\mathrm{M}} w_i(\mathbf{x})\kappa\left(\frac{b-a}{2}\xi_i + \frac{a+b}{2}, \mathbf{x}\right)^n, \tag{2.10}$$

where ξ_i are roots of the Legendre orthogonal polynomials, defined by the recurrence relation

$$\begin{aligned} &Q_{-1}(\xi) = 0 \\ &Q_0(\xi) = 1 \\ &(r+1)Q_{r+1}(\xi) = (2r+1)\xi Q_r(\xi) - rQ_{r-1}(\xi). \end{aligned} \tag{2.11}$$

Independently from the type of distribution under consideration, quadrature weights and nodes are determined by solving an eigenvalue problem, considering the Jacobi matrix whose coefficients depend on the recurrence relation that defines the orthogonal polynomials [29]. The procedure is summarized in Appendix A.

2.3 Properties of Quadrature-Based UQ

We summarize in this section a few properties of the quadrature-based uncertainty quantification procedure described in the previous section. These properties were discussed in detail elsewhere [4, 119] and discussed further in Appendix B.

2.3.1 Equivalence to stochastic collocation

The equivalence between the quadrature-based UQ procedure and stochastic collocation methods is immediately observed [4,119], for a one-dimensional space of uncertain parameters, by considering the approximated system response in terms of Lagrange polynomials given by the statistical collocation method

$$\kappa(\xi) = \sum_{i=1}^{M} \kappa_i L_i(\xi), \tag{2.12}$$

with the Lagrange polynomial L_i defined as

$$L_i = \prod_{\substack{j=1 \\ i\neq j}}^{\mathrm{M}} \frac{\xi - \xi_j}{\xi_i - \xi_j}. \tag{2.13}$$

The moments defined by Eq. 2.1 are then

$$m_n = \int_\Omega \left(\sum_{i=1}^{\mathrm{M}} \kappa_i \prod_{\substack{j=1 \\ i \neq j}}^{\mathrm{M}} \frac{\xi - \xi_j}{\xi_i - \xi_j} \right)^n p(\xi) \mathrm{d}\xi. \tag{2.14}$$

Approximating the integral with quadrature, and choosing the stochastic collocation points as the quadrature abscissae of an appropriate quadrature formula, the equivalence between stochastic collocations and quadrature-based UQ becomes apparent. This is because the expression of the moments of the system response obtained with Eq. 2.14 provides the same result given by Eq. 2.2:

$$m_n \approx \sum_{l=1}^{\mathrm{M}} w_l \left(\sum_{i=1}^{\mathrm{M}} \kappa_i \prod_{\substack{j=1 \\ i \neq j}}^{\mathrm{M}} \frac{\xi_l - \xi_j}{\xi_i - \xi_j} \right)^n = \sum_{l=1}^{\mathrm{M}} w_l \kappa(\xi_l)^n. \tag{2.15}$$

2.3.2 Polynomial chaos expansion and estimation of the required number of samples

The polynomial chaos approach [13, 38, 58, 73, 98, 115] approximates the system response with a truncated Fourier series

$$\kappa(\boldsymbol{\xi}) \approx \sum_{j=0}^{\mathrm{Q}} \kappa_j \Psi_j(\boldsymbol{\xi}), \tag{2.16}$$

being $\Psi_j(\boldsymbol{\xi})$ orthogonal polynomials to the random input variable, and

$$\kappa_j = \frac{\langle \kappa(\boldsymbol{\xi}), \Psi_j(\boldsymbol{\xi}) \rangle}{\langle \Psi_j(\boldsymbol{\xi}), \Psi_j(\boldsymbol{\xi}) \rangle}, \tag{2.17}$$

with $\langle a, b \rangle$ the inner product of the probability measure $p(\boldsymbol{\xi})$, defined as

$$\langle a(\boldsymbol{\xi}), b(\boldsymbol{\xi}) \rangle = \int_\Omega a(\boldsymbol{\xi}) b(\boldsymbol{\xi}) p(\boldsymbol{\xi}) \mathrm{d}\boldsymbol{\xi}.$$

The convergence of the PC series depends on the shape of the function $\kappa(\boldsymbol{\xi})$ [11, 73]. The moments of the system response are calculated using Eq. 2.16 to express $\kappa(\boldsymbol{\xi})$ in Eq. 2.1. If a one-dimensional case is considered, and the integrals involved in the definition of the inner product are approximated by the corresponding quadrature formulae, the moments of the system response can be found as [4, 119]

$$m_n \approx \sum_{l=1}^{\mathrm{M}} w_l \left[\sum_{j=0}^{\mathrm{Q}} \Psi_j(\xi_l) \left(\frac{\sum_{i=1}^{\mathrm{M}} w_i \kappa(\xi_i) \Psi_j(\xi_i)}{\langle \Psi_j, \Psi_j \rangle} \right) \right]^n. \tag{2.18}$$

Based on the properties of Gaussian quadrature formulae, it is possible to estimate the required number of samples to compute the moments of the system response exactly. Such estimates are rigorously derived [4, 119] in the case of a system response that is represented by polynomials (see Appendix B). In particular, for a one-dimensional space of the uncertain parameters, with a system response $\kappa(\xi)$ represented by a polynomial of order not higher than q, it can be shown that the number of samples M required to compute the Q-th order polynomial chaos approximation of the moment of order n using Eq. 2.18 is

$$M = \max\left(\frac{nq+1}{2}, \frac{q+Q+1}{2}\right). \tag{2.19}$$

In case the number of samples is insufficient to compute the desired moment exactly, if the random response is continuous and differentiable up to order q, with derivative of order $q+1$ defined on the support of the random variable ξ, it is possible to estimate the error affecting the estimated value of the moment by expanding the system response with a Taylor series (see Appendix B).

2.4 Reconstruction of the Response Probability Distribution Function

The set of moments of the model response to the uncertain input parameters can be used to reconstruct an approximated PDF of the values of the response using the extended quadrature method of moments [121].

Before illustrating the procedure to approximate the PDF of the model output, we briefly remind the reader of the conditions a set of real values has to satisfy in order to be a set of moments of a probability measure, which corresponds, for the case of $\xi \in [0, 1]$, to solving a Hausdorff problem [19] to determine when moments are realizable. Such a problem is defined considering a set of $2k+1$ scalars and the moment space $\mathcal{M}_{2k}$ of a probability measure with support on the closed interval $[0, 1]$

$$M_{2k} = \{m_0, m_1, m_2, ...m_{2k}\}. \tag{2.20}$$

The two Hankel determinants [19] are then defined as

$$\underline{H}_{2l} = \begin{vmatrix} m_0 & m_1 & \dots & m_l \\ m_1 & m_2 & \dots & m_{l+1} \\ \vdots & & & \vdots \\ m_l & m_{l+1} & \dots & m_{2l} \end{vmatrix}, \tag{2.21}$$

and

$$\overline{H}_{2l} = \begin{vmatrix} m_1 - m_2 & m_2 - m_3 & \dots & m_l - m_{l+1} \\ m_2 - m_3 & m_3 - m_4 & \dots & m_{l+1} - m_{l+2} \\ \vdots & & & \vdots \\ m_l - m_{l+1} & m_{l+1} - m_{l+2} & \dots & m_{2l-1} - m_{2l} \end{vmatrix}. \tag{2.22}$$

The set defined by Eq. 2.20 belongs to the moment space $\mathcal{M}_{2k}$ of a probability measure if and only if the determinants $\underline{H}_i$, and $\overline{H}_i$ are positive or null for $i = 1, \dots, 2k$ [19] (realizability condition):

$$M_{2k} \in \mathcal{M}_{2k} \Leftrightarrow \underline{H}_i \geq 0 \wedge \overline{H}_i \geq 0, i = 1, \dots, 2k. \tag{2.23}$$

The realizability condition expressed by Eq. 2.23 is a necessary condition to be able to proceed with the PDF reconstruction, and can be used to determine if the quality of the estimated moments is sufficient to ensure a successful reconstruction of the PDF of the model response $f(\kappa)$.

Assuming the moments of the system response computed with the quadrature-based UQ procedure satisfy the realizability condition given in Eq. 2.23, we define the reconstruction procedure for $f(\kappa)$ for the case of one uncertain parameter ξ, leaving the extension to multivariate problems to future work. The foundation of such a procedure is representing f as a weighted sum of a finite number N of non-negative functions [14, 121]

$$f_N(\kappa) = \sum_{i=1}^{N} \rho_i \delta_\sigma(\kappa, \kappa_i), \tag{2.24}$$

where we indicate with ρ_i the i-th quadrature weight used in the PDF reconstruction, to avoid confusion with the quadrature weights w_i used in the sampling procedure, κ_i is the i-th quadrature node used in the PDF reconstruction, and $\delta_\sigma(\kappa, \kappa_i)$ is a kernel density function depending on the parameter σ.

The choice of the functional form of δ_σ depends on the nature of the distribution that has to be reconstructed, and, in particular on the interval of definition (support) of such a distribution, which is determined by the parameter σ. If κ is defined in a bounded interval $[a, b]$, δ_σ can be set equal to a beta distribution, while if κ is positive and defined on $[0, +\infty[$, the gamma distribution represents an adequate choice. The case of a system response defined on the whole real set can be treated using a Gaussian distribution to define the kernel density function. The reconstruction procedure for beta distributions is illustrated in Section 2.4.1, while the interested reader can find the procedure for a gamma distribution [121] and for a Gaussian distribution [14] in the literature.

2.4.1 Beta kernel function

The beta kernel function is defined as [121]

$$\delta_\sigma(\kappa, \kappa_i) = \frac{\kappa^{\lambda_i - 1} (1 - \kappa)^{\phi_i - 1}}{B(\lambda_i, \phi_i)} \tag{2.25}$$

where $\lambda_i = \kappa_i/\sigma$, $\phi_i = (1 - \kappa_i)/\sigma$, κ is bounded in the interval $[0, 1]$, and $B(\lambda_i, \phi_i)$ is the beta function defined as $B(x, y) = \int_0^1 t^{x-1}(1 - t)^{y-1}\mathrm{d}t$. The distribution of the system response can be then represented as

$$f_N(\kappa) = \sum_{i=1}^{N} \rho_i \delta_\sigma(\kappa, \kappa_i) = \sum_{i=1}^{N} \rho_i \frac{\kappa^{\lambda_i - 1} (1 - \kappa)^{\phi_i - 1}}{B(\lambda_i, \phi_i)}, \tag{2.26}$$

where we have to use $2N + 1$ moments to determine $2N + 1$ unknowns (N quadrature weights ρ_i and quadrature nodes κ_i for $i = 1, \ldots, N$, and the parameter σ). This is achieved by first considering the n-th order integer moments of $\delta_\sigma(\kappa, \kappa_i)$, which can be written in a recursion form:

$$m_n^{(i)} = \frac{\kappa_i + (n - 1)\sigma}{1 + (n - 1)\sigma} m_{n-1}^{(i)} \text{ for } n > 0, \tag{2.27}$$

and $m_0^{(i)} = 1$. Thus the integer moments of the distribution function f can be expressed as

$$m_n = \sum_{i=1}^{N} \rho_i m_n^{(i)} = \sum_{i=1}^{N} \rho_i G_n(\kappa_i, \sigma),$$

with

$$G_n(\kappa_i, \sigma) = \begin{cases} 1 & n = 0 \\ \prod_{i=0}^{n-1} \dfrac{\kappa_i + i\sigma}{1 + i\sigma} & n \geq 1 \end{cases}. \tag{2.28}$$

A lower triangular system can be defined to find σ by re-writing these moments as [121]

$$m_n = \eta_n m_n^* + \eta_{n-1} m_{n-1}^* + \ldots + \eta_1 m_1^*,\ \eta_n \geq 0$$

where the non-negative coefficients η_n depend only on σ, and $m_n^* = \sum_{i=1}^{N} \rho_i \kappa_i^n$. This system can be written in the matrix form $\mathbf{A}(\sigma)\mathbf{m}^* = \mathbf{m}$ where $\mathbf{A}(\sigma)$ is a lower triangular matrix. The quadrature weights ρ_i and nodes κ_i can be found from the first $2N$ moments $(m_0^*, \ldots, m_{2N-1}^*)$ using the moment inversion algorithm, Wheeler algorithm [113,120]. The parameter σ is found using an iterative procedure [121]:

1. Guess σ
2. Compute the moments m_n^* from the system $\mathbf{A}(\sigma)\mathbf{m}^* = \mathbf{m}$
3. Use the Wheeler algorithm to find weights ρ_i and abscissae κ_i from $\mathbf{m}^*$
4. Compute m_{2N}^* using ρ_i and κ_i
5. Compute
$$J_N(\sigma) = m_{2N} - \eta_{2N} m_{2N}^* - \eta_{2N-1} m_{2N-1}^* + \ldots - \eta_1 m_1^*$$
6. If $J \neq 0$, compute a new guess for σ and iterate from 1.

A transformation and a normalization process are required in order to extend the approach presented above to the general bounded interval $[a, b]$. For such a purpose, let $\kappa = (b-a)\xi + a$, where $\xi \in [0, 1]$ with the distribution shown in Eq. 2.26. Then the normalized distribution for κ in the interval $[a, b]$ is

$$f_N(\kappa) = \frac{\sum_{i=1}^{N} \rho_i \frac{\left(\frac{\kappa-a}{b-a}\right)^{\lambda_i-1}\left(\frac{b-\kappa}{b-a}\right)^{\phi_i-1}}{B(\lambda_i,\phi_i)}}{\int_a^b \sum_{i=1}^{N} \rho_i \frac{\left(\frac{\kappa-a}{b-a}\right)^{\lambda_i-1}\left(\frac{b-\kappa}{b-a}\right)^{\phi_i-1}}{B(\lambda_i,\phi_i)} \mathrm{d}\kappa},$$

where the value of the integral in the denominator is

$$\int_a^b \sum_{i=1}^{N} \rho_i \frac{\left(\frac{\kappa-a}{b-a}\right)^{\lambda_i-1}\left(\frac{b-\kappa}{b-a}\right)^{\phi_i-1}}{B(\lambda_i,\phi_i)} \mathrm{d}\kappa = (b-a)\int_0^1 \sum_{i=1}^{N} \rho_i \frac{\xi^{\lambda_i-1}(1-\xi)^{\phi_i-1}}{B(\lambda_i,\phi_i)} \mathrm{d}\xi = b-a.$$

As a consequence, the final normalized distribution for κ in bounded interval $[a, b]$ is

$$f_N(\kappa) = \frac{1}{b-a} \sum_{i=1}^{N} \rho_i \frac{\left(\frac{\kappa-a}{b-a}\right)^{\lambda_i-1}\left(\frac{b-\kappa}{b-a}\right)^{\phi_i-1}}{B(\lambda_i,\phi_i)}, \tag{2.29}$$

where parameters λ_i and σ are determined by the methods described above. It is worth to mention that Eq. 2.29 can be used to determine the probability of critical events defined, for example, by a cut-off value of $\kappa > \kappa_{\text{cutoff}}$. This represents a key advantage of the proposed UQ procedure, because this type of calculation is not possible with conventional UQ methods, where the reconstructed form of the PDF of the system response is not readily available.

2.5 Applications

Two example applications were chosen to demonstrate the proposed UQ procedure with reconstruction of the PDF of the system response. The first is the channel flow problem considered in [56], due to its simplicity and to the availability of UQ results suitable for comparison. The second is an oblique shock problem involving a compressible flow, which presents discontinuities in the physical space, with a sudden spatial change in the values of the output variable [46]. The moments of the streamwise fluid velocity component are computed and their convergence as a function of the number of samples is studied. Low-order statistics of the streamwise velocity are reported, and the PDF of the system response at specific locations in the computational domain is reported. The accuracy of the reconstruction procedure is assessed by comparing the reconstructed distribution with the one obtained by directly sampling a large number of outputs obtained from the simulation.

2.5.1 Developing channel flow

The development of the flow in a channel considered in [56] with uncertain viscosity was chosen as the first example application of the quadrature-based uncertainty quantification approach introduced in the previous sections. Channel flow has also been considered as a test problem by other authors [74,116]. The channel under examination is schematically represented in Fig. 2.1.

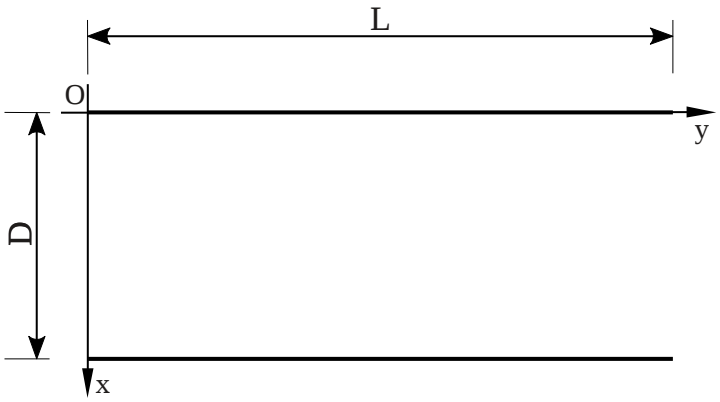

Figure 2.1 Schematic representation of the channel.

In the simulations, a ratio L/D = 6 and Reynolds number Re = 81.24 were used. The governing Navier-Stokes equations for the incompressible flow in the two-dimensional channel are:

$$\begin{aligned} &\frac{\partial \boldsymbol{u}}{\partial t} + (\boldsymbol{u} \cdot \nabla)\, \boldsymbol{u} = -\frac{1}{\rho}\nabla p + \nu \nabla^2 \boldsymbol{u} \\ &\nabla \cdot \boldsymbol{u} = 0 \end{aligned} \tag{2.30}$$

where $\boldsymbol{u}$ is the velocity field, p is the pressure, ρ is the density, and ν is the viscosity. A uniform velocity profile is assumed at the inlet of the channel, while fully developed flow is imposed at the outlet. No-slip boundary conditions are applied at the channel walls. The open-source package OpenFOAM [44,79,80] was used to perform the simulations, using a second-order finite volume scheme to discretize Eq. 2.30. The pressure-velocity coupling was achieved by means of the SIMPLE algorithm [25, 84]. The solution was assumed to be converged when the pressure and velocity residuals fell below 10^{-12}, as shown in Fig. 2.2.

As anticipated, in this study we assume that the numerical solution is not affected by numerical errors. As a consequence, careful attention was paid to determine the grid-independent solution, in order to minimize the numerical error. Three grid resolutions were considered to study the dependency of the solution on the spatial discretization (points along D $\times$ points along L): 32×128, 64×256, 128×512. Since the solution on the grid with 64×256 points satisfied the criterion of grid independence, differing of less than 5% from the solution on more refined grids, this grid resolution was adopted to perform the uncertainty quantification study.

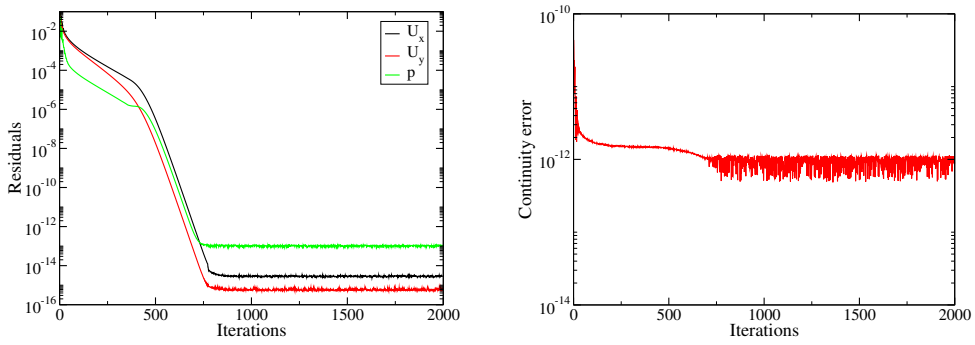

(a) (b)

Figure 2.2 History of (a) residuals for the channel flow simulation, and of (b) the continuity error on the 64×256 grid.

Fig. 2.2(b) shows the convergence history of the continuity error as a function of the number of iterations. At convergence, this error has order of magnitude of 10^{-12}.

A uniform distribution of the constant viscosity of the flow was assumed. The mean viscosity ν_0 was supposed to be 1, and the standard deviation of the viscosity was $0.3\nu_0$. Thus the flow viscosity assumed values in the interval $[0.7, 1.3]$. The procedure illustrated in Section 2.2.1 was then used to compute the moments of the system response, after producing the samples.

2.5.1.1 Convergence of the moments

The convergence of the moments of the streamwise fluid velocity is studied here, by considering the absolute value of the difference between the value of each moment computed with a given number of samples, and the value of the same moment computed with 1000 samples, which is assumed to be exact.

$$e_{\text{abs},n,i} = \left| m_{n,i} - m_{n,1000} \right| .$$

Seven sets of samples were considered, respectively with 3, 5, 10, 20, 40, 80 and 100 samples. The absolute errors for the moments of the axial component of the fluid velocity are reported in Tables 2.1, 2.2, and 2.3. All the set of samples ensure exact prediction of the zero-order moment, since its value is guaranteed to be exact by the quadrature representation. Additionally, we observe that twenty samples are sufficient to calculate the five moments with an accuracy higher than 10^{-8}, moments of order 5 to 9 are predicted with an absolute error of magnitude

10^{-8}. It is worth noticing that using a significantly higher number of samples does not lead to a significant reduction of the error affecting the highest order moments considered in this example.

Table 2.1 Absolute error of m_0, m_1, m_2 , m_3 as a function of the number of samples.

Samples	$e_{\text{abs},0,i}$	$e_{\text{abs},1,i}$	$e_{\text{abs},2,i}$	$e_{\text{abs},3,i}$
3	0	1.246×10^{-6}	3.532×10^{-6}	7.487×10^{-6}
5	0	1.415×10^{-8}	2.979×10^{-8}	4.703×10^{-8}
10	0	1.312×10^{-8}	2.625×10^{-8}	3.942×10^{-8}
20	0	1.779×10^{-9}	3.561×10^{-9}	5.346×10^{-9}
40	0	6.865×10^{-10}	1.398×10^{-9}	2.135×10^{-9}
80	0	2.781×10^{-10}	5.576×10^{-10}	8.387×10^{-10}
100	0	1.460×10^{-10}	2.928×10^{-10}	4.404×10^{-10}

Table 2.2 Absolute error of m_4, m_5, m_6 as a function of the number of samples.

Samples	$e_{\text{abs},4,i}$	$e_{\text{abs},5,i}$	$e_{\text{abs},6,i}$
3	1.407×10^{-5}	2.471×10^{-5}	4.153×10^{-5}
5	6.599×10^{-8}	1.023×10^{-7}	1.553×10^{-7}
10	5.260×10^{-8}	6.581×10^{-8}	7.905×10^{-8}
20	7.134×10^{-9}	8.926×10^{-9}	1.072×10^{-8}
40	2.899×10^{-9}	3.689×10^{-9}	4.508×10^{-9}
80	1.121×10^{-9}	1.405×10^{-9}	1.691×10^{-9}
100	5.888×10^{-10}	7.380×10^{-10}	8.880×10^{-10}

Table 2.3 Absolute error of m_7, m_8, m_9 as a function of the number of samples.

Samples	$e_{\text{abs},7,i}$	$e_{\text{abs},8,i}$	$e_{\text{abs},9,i}$
3	6.760×10^{-5}	1.073×10^{-4}	1.669×10^{-4}
5	2.294×10^{-7}	3.378×10^{-7}	5.017×10^{-7}
10	9.231×10^{-8}	1.056×10^{-7}	1.189×10^{-7}
20	1.252×10^{-8}	1.440×10^{-8}	1.650×10^{-8}
40	5.904×10^{-9}	8.629×10^{-9}	1.271×10^{-8}
80	1.978×10^{-9}	2.267×10^{-9}	2.557×10^{-9}
100	1.039×10^{-9}	1.190×10^{-9}	1.343×10^{-9}

Fig. 2.3 shows the filled contour plots of the velocity mean, showing a peak axial velocity of 1.5 m/s. The variance, skewness, and kurtosis of each velocity component are also reported in the figure.

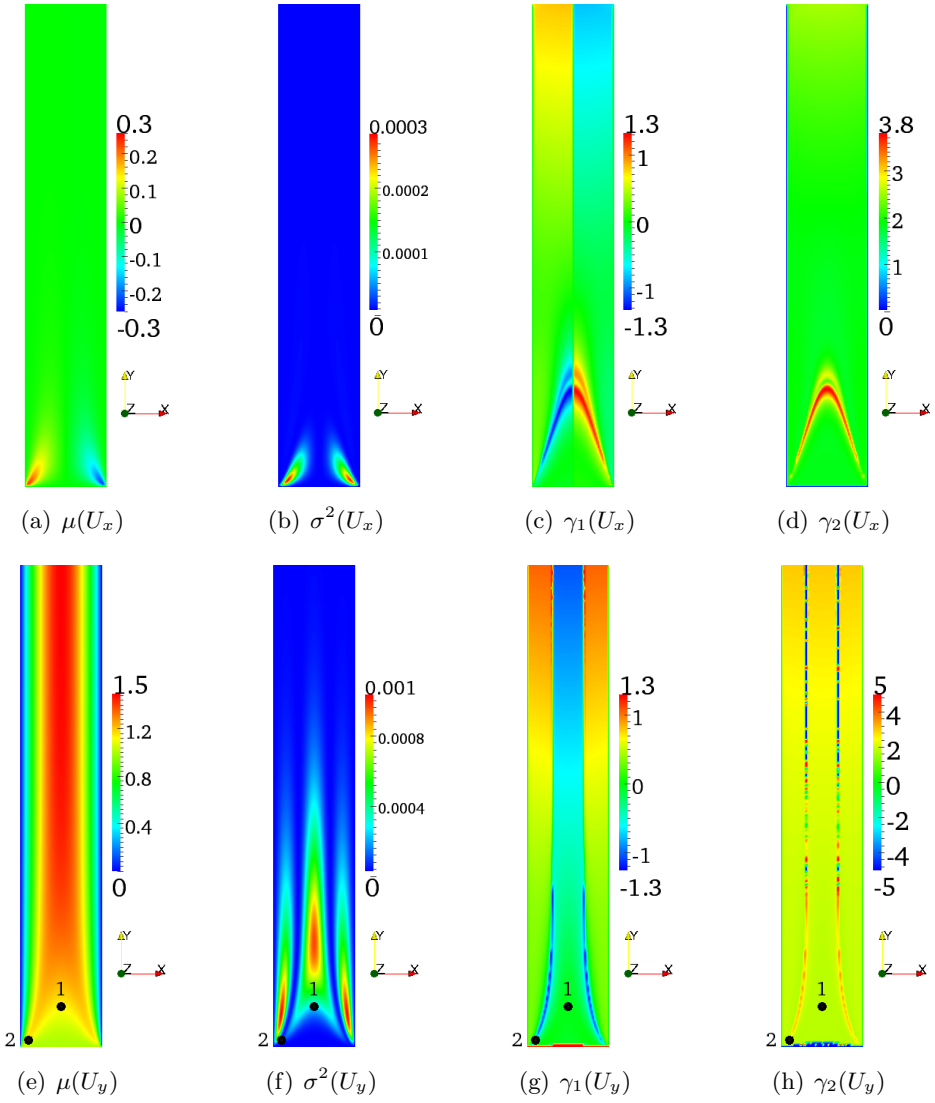

(a) $\mu(U_x)$ (b) $\sigma^2(U_x)$ (c) $\gamma_1(U_x)$ (d) $\gamma_2(U_x)$

(e) $\mu(U_y)$ (f) $\sigma^2(U_y)$ (g) $\gamma_1(U_y)$ (h) $\gamma_2(U_y)$

Figure 2.3 Contour plots of mean, variance, skewness, and kurtosis of the two velocity components: (a)-(d) spanwise, (e)-(h) streamwise. Two locations designated are the points where EQMOM is used to reconstruct the PDF of the system response.

2.5.1.2 Reconstructed distribution

The reconstructed distribution of the axial velocity is studied here with the method discussed in Section 2.4. Before proceeding with the application of the extended quadrature method of moment [66, 121] procedure, the samples are normalized so that the values of the system response are contained into the interval $[0, 1]$. This result is achieved by computing

$$\kappa_i = \frac{u_i - u_{min}}{u_{max} - u_{min}}.$$

and by computing the moments of κ according to Eq. 2.1. These moments are then used as input in β-EQMOM, and approximate distributions are calculated according to Eq. 2.29. This procedure is used to perform the EQMOM reconstruction in all the cases considered in this work.

Two sets of data at different locations were used to perform the reconstruction, one on the channel centerline (location 1), and the other near the wall (location 2). The approximate distributions, reported in Fig. 2.4 display two different profiles. The axial velocity at the location 1 presents a nearly uniform distribution, showing that the uniform distribution provided as input is propagated to the system response without significant changes. However, the axial velocity distribution at location 2 strongly deviates from uniform distribution.

The reconstructed distribution using EQMOM is also compared with the one obtained from 1000 samples by dividing the whole set of samples in 10 bins. Each bin is formed by a constant number of samples N_{bin}, equal for each bin, and the limiting values of each bin are determined to enforce this assumption, defining the bin width δ_{bin}. The weight attributed to each bin w_{bin} is calculated by summing the quadrature weights of the samples contained in the bin. The frequency of each bin is reported in the histograms, in which the height of each bar is computed as

$$h_i = \frac{1}{\sum_j w_{\text{bin},j} N_{\text{bin},j}} \frac{N_{\text{bin},i} w_{\text{bin},i}}{\delta_{\text{bin},i}} \tag{2.31}$$

The approximate distributions show good agreement with the histograms reconstructed from 1000 samples for all the considered conditions, which indicates four nodes are sufficient to reconstruct the axial velocity distribution for this case.

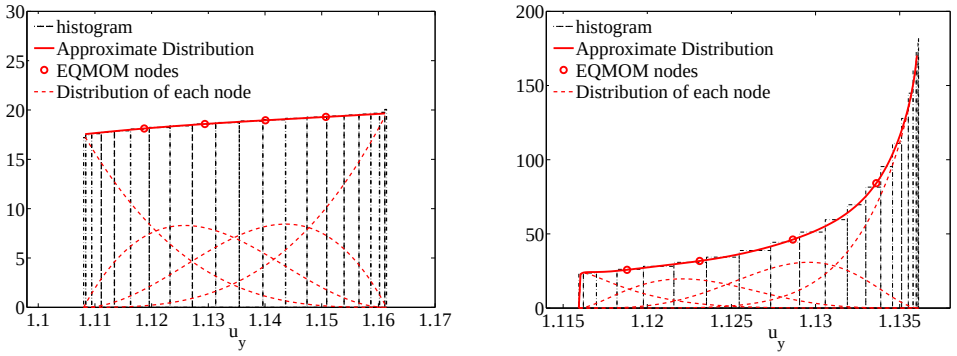

(a) central line (location 1)

(b) near wall (location 2)

Figure 2.4 Reconstructed distribution of the axial velocity.

2.5.1.3 Polynomial chaos expansion

The PC expansion of the axial velocity is determined here to compare with the quadrature-based UQ results. The system response can be expressed as in Eq. 2.32 [56],

$$u(\boldsymbol{\xi}) \approx \sum_{j=0}^{Q} u_j \boldsymbol{\Psi}_j(\boldsymbol{\xi}) \tag{2.32}$$

where $\boldsymbol{\Psi}_j$ is a basis of orthogonal polynomials corresponding to the input distribution, in this case for example Legendre polynomials for uniform distributions. The coefficients u_j can be calculated as Eq. 2.33 by projecting the response against each basis function [4, 119].

$$u_j = \frac{\langle u(\boldsymbol{\xi}), \boldsymbol{\Psi}_j(\boldsymbol{\xi}) \rangle}{\langle \boldsymbol{\Psi}_j(\boldsymbol{\xi}), \boldsymbol{\Psi}_j(\boldsymbol{\xi}) \rangle} \tag{2.33}$$

Following [56], a third order ($Q = 3$) polynomial chaos expansion of the axial velocity is reported here, and the four coefficients u_0, u_1, u_2, and u_3 are shown in Fig. 2.5. Once the polynomial chaos expansion function is obtained, the mean value of the system response is known, which is the value of the first polynomial chaos coefficient u_0. Compared the mean values of the axial velocity obtained by quadrature-based UQ procedure and PC expansion, shown in Fig. 2.3(e) and Fig. 2.5(a), the two contour plots show great agreement. The largest absolute value of this differences has magnitude equal to 10^{-5}, indicating quadrature-based UQ procedure is consistent with the PC expansion approach.

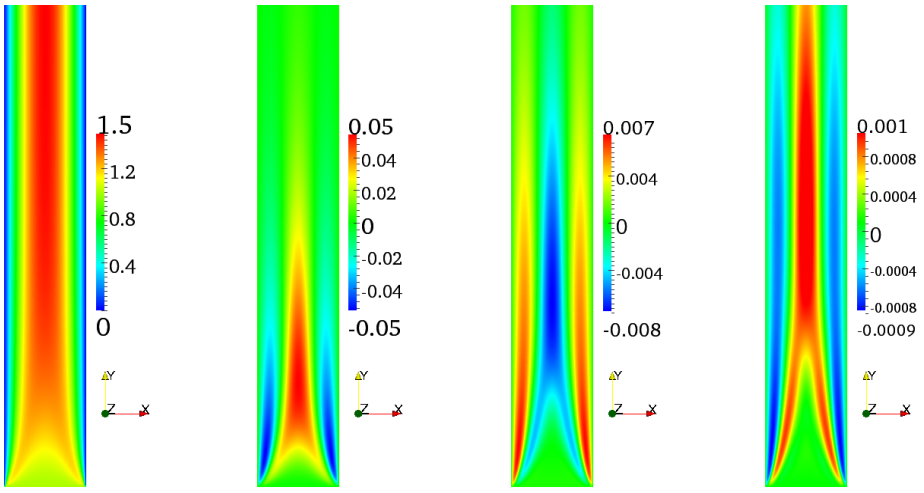

(a) u_0 (b) u_1 (c) u_2 (d) u_3

Figure 2.5 Contour plots of polynomial chaos expansion coefficients of the axial velocity.

2.5.2 Oblique shock problem

The second example application of the quadrature-based uncertainty quantification approach is a compressible flow with an uncertain Mach number over an inclined surface with an angle θ with respect to the horizontal. The problem is schematically represented in Fig. 2.6. The governing Euler equations are derived from Navier-Stokes equations for inviscid, compressible flow, shown in Eq. 2.34.

$$\begin{aligned} \frac{\partial \rho}{\partial t} + \nabla \cdot (\rho \boldsymbol{u}) &= 0 \\ \rho \frac{\partial \boldsymbol{u}}{\partial t} + \rho \boldsymbol{u} \cdot \nabla \boldsymbol{u} + \nabla p &= \boldsymbol{0} \end{aligned} \tag{2.34}$$

In the simulations, the flow was fed with a uniform inlet. A shock discontinuity is formed with an angle β with respect to the horizontal, which can be expressed by Eq. 2.35, related to the inlet Mach number, the ratio of the specific heats γ, and the angle θ.

$$\tan\theta = 2\cot\beta \frac{\mathrm{Ma}_1^2 \sin^2\beta - 1}{\mathrm{Ma}_1^2(\gamma + \cos 2\beta) + 2} \tag{2.35}$$

The case was simulated considering a computational grid of 640×320 cells which ensured grid independence with the rhoCentralFoam solver provided with open-source package OpenFOAM [79, 80].

A uniform distribution of the upstream Mach number was assumed. The mean Mach number was 3, and the standard deviation was 0.3. Thus the upstream Mach number was

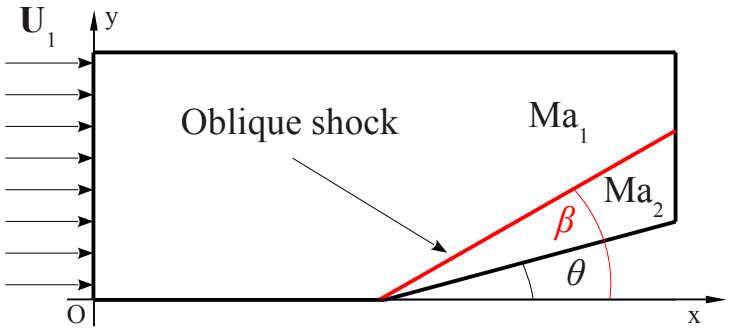

Figure 2.6 Schematic representation of the oblique shock problem.

in the interval $[2.7, 3.3]$. The method described in Section 2.2.1 was applied to calculate the moments of the system response based on the samples obtained from the numerical simulations.

2.5.2.1 Low-order statistics of the system response

The low-order statistics of the streamwise velocity are presented in this section. The moments computed with 20 samples are compared to the same moments computed with 100 samples, which are assumed exact in this case. The filled contour plots of the mean and variance of the horizontal velocity component are reported in Fig. 2.7. As expected, a shock discontinuity is observed with an angle with respect to horizontal. This angle is not a defined value, but it belongs to a range because of the uncertainty of the Mach number. The interval containing the shock can be calculated analytically from Eq. 2.35, while the interval predicted by the UQ procedure is determined by measuring the angular width of the horizontal velocity variance across the shock. Table 2.4 shows the angle range calculated from the analytical solution and measured in the UQ procedure, indicating that the estimation of the shock angle with the UQ procedure matches the analytical value with an error on the order of 0.1 degrees. Fig. 2.8 shows the absolute error of the mean and variance of the horizontal velocity component. Because of the shock discontinuity, the absolute errors in this region are in magnitude of 10^{-3}, while in other regions the absolute errors are nearly zero.

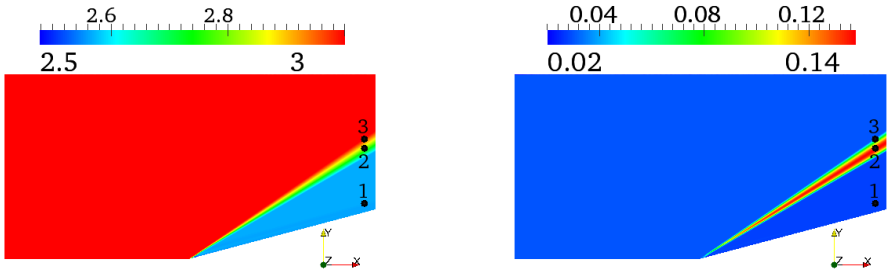

(a) (b)

Figure 2.7 Mean and variance of the horizontal velocity component: (a) $\mu(U_x)$, (b) $\sigma^2(U_x)$. Three locations designated are the points where EQMOM is used to reconstruct the PDF of the system response.

Table 2.4 Shock angles.

Ma_1	$\beta_{\mathrm{analytical}}$	β_{UQ}
2.7	34.78	34.32
3.3	30.27	30.50

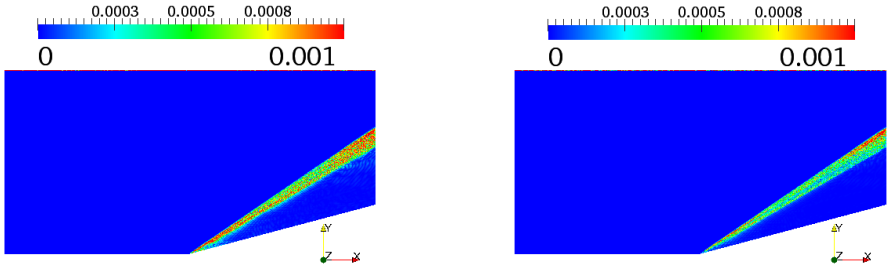

(a) (b)

Figure 2.8 Absolute error of (a) mean and (b) variance of the horizontal velocity component.

2.5.2.2 Reconstructed distribution

The reconstructed distribution of the horizontal velocity component is studied in this section. Three sets of data at different locations were used to perform the reconstruction, one below the shock (location 1), and two in the shock region (location 2 and 3). Approximate distributions are reported in Figs. 2.9 and 2.10. The uniform distribution provided as input is maintained nearly unchanged for the distribution of the horizontal velocity at location 1, while distributions of the horizontal velocity at location 2 and 3 significantly differ from the uniform. Distributions of the horizontal velocity in the shock region display step function profiles because of the shock discontinuity.

The effect of the number of EQMOM nodes on the reconstructed distribution was considered. The approximate distribution of the horizontal velocity below the shock region shows good consistency with the histogram, and increasing the number of EQMOM nodes does not significantly influence the quality of the reconstruction. The approximate distributions shown in Fig. 2.10 presents some oscillations, which is expected because of the steep discontinuity presented by the values of the distribution that is being reconstructed. The reconstruction of the distribution in the shock region improves when the number of EQMOM nodes increases, because this leads to a reduction of the oscillatory behaviour. However, increasing the number of EQMOM nodes requires higher order moments to be computed, whose accuracy decreases with the order due to truncation errors. Considering both the calculation accuracy and the shape of the approximate distributions, four nodes are adequate to reconstruct the horizontal velocity distribution for this case.

2.5.2.3 Polynomial chaos expansion

The four PC expansion coefficients of the horizontal velocity u_0, u_1, u_2, and u_3 are shown in Fig. 2.11. By substituting these coefficients into Eq. 2.32, the horizontal velocity for each sample can be recomputed and then the mean horizontal velocity can be obtained from the first coefficient u_0. Compared the mean horizontal velocity obtained by quadrature-based UQ procedure and PC expansion, shown in Fig. 2.7(a) and Fig. 2.11(a), the two contour plots

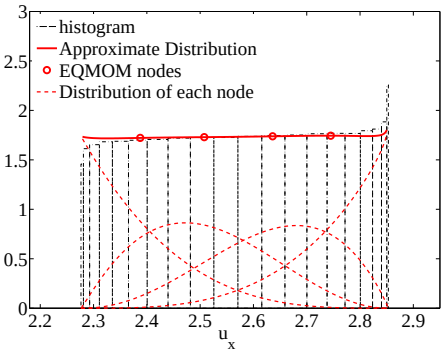

(a) location 1

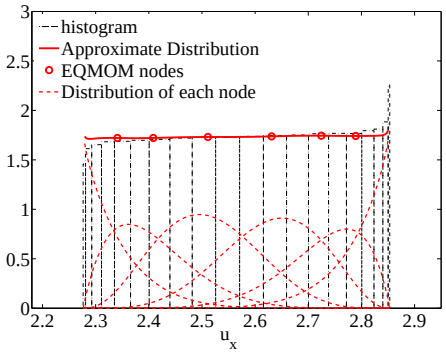

(b) location 1

Figure 2.9 Reconstructed distribution of the horizontal velocity below the shock region: (a) 4 EQMOM nodes, (b) 6 EQMOM nodes.

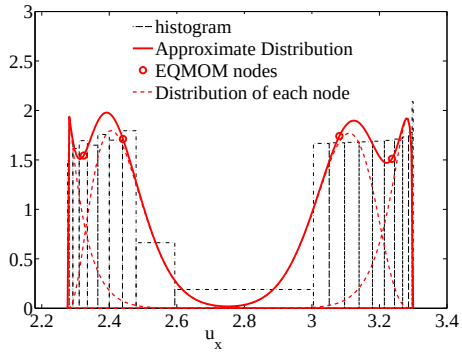

(a) location 2

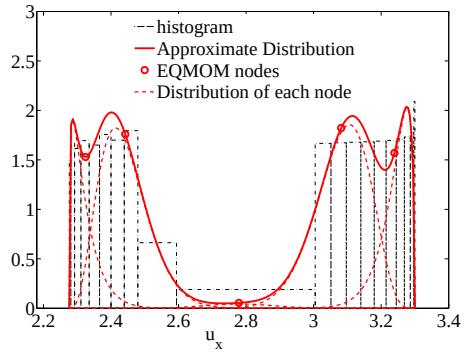

(b) location 2

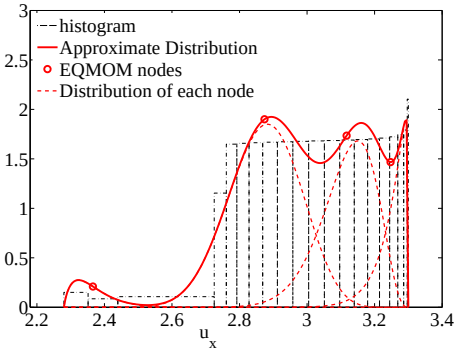

(c) location 3

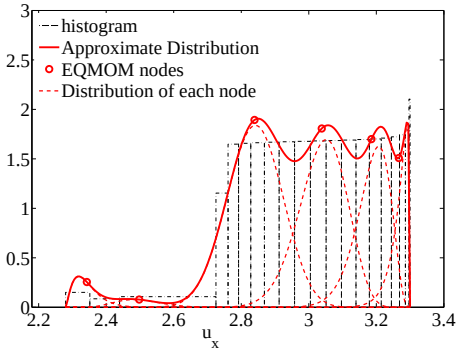

(d) location 3

Figure 2.10 Reconstructed distribution of the horizontal velocity in the shock region: (a) 4 EQMOM nodes, (b) 5 EQMOM nodes, (c) 4 EQMOM nodes, (d) 6 EQMOM nodes.

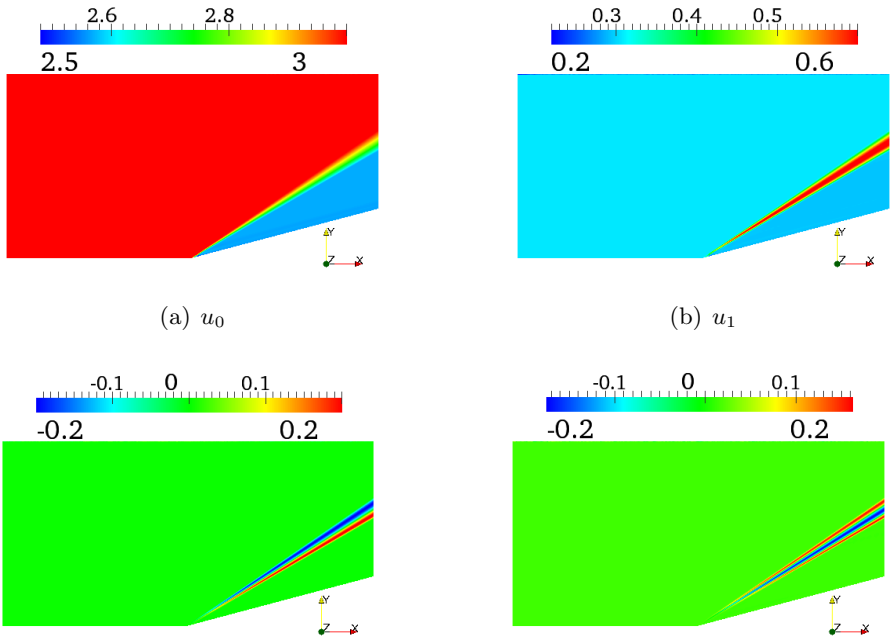

(a) u_0 (b) u_1

(c) u_2 (d) u_3

Figure 2.11 Contour plots of polynomial chaos expansion coefficients of the horizontal velocity.

show good agreement. Although the number of samples used in this case is not large (100 at most) and the shock discontinuity is formed, the absolute difference is still acceptable, with magnitude 1.0×10^{-3}.

2.6 Conclusions

A quadrature-based approach to perform uncertainty quantification and reconstruction of the distribution of values of the system response is introduced in this work, and developed for the case of problems with one uncertain parameter. The approach is demonstrated considering a developing channel flow and an oblique shock problem. The approach is successfully compared to the PC methodology, showing that the quadrature-based UQ procedure correctly reproduces the moments of the system response, without the necessity of proceeding to the application of the PC expansion. The reconstruction of the distribution function of the system response are performed successfully in both the cases, obtaining excellent results in the case of smooth distributions, and satisfactory results when discontinuities are present. The reconstruction

procedure illustrated in this work can be naturally extended to multi-variate problems, as it will be shown in future work.

CHAPTER 3. A QUADRATURE-BASED UNCERTAINTY QUANTIFICATION APPROACH WITH RECONSTRUCTION OF THE PROBABILITY DISTRIBUTION FUNCTION OF THE SYSTEM RESPONSE IN BUBBLING FLUIDIZED BEDS

In simulations of industrial systems, it is important to have an estimate of the distributions of errors due to uncertainty in the model parameters and input data. This can be accomplished by developing uncertainty quantification tools that can be combined with available CFD codes. A non-intrusive, quadrature-based, uncertainty quantification (QBUQ) method is presented in this chapter, and is demonstrated by considering a bubbling fluidized bed as example application. The particle size is assumed to be the uncertain input parameter. The system is simulated with a standard two-fluid model with kinetic theory closures for the particulate phase implemented into MFIX. The effect of uncertainty on the disperse-phase volume fraction, on the phase velocities, and on the pressure drop inside the fluidized bed are examined, and the reconstructed probability functions (PDFs) are provided for the three quantities studied.

3.1 Introduction

Gas-fluidized beds are widely applied to a variety of industrial operations and processes [8, 51, 118]. Computational fluid dynamics (CFD) is a useful tool to study and model gas-fluidized beds and to provide help for design and optimization of the process [105, 107]. In most of CFD simulations, the predicted results are deterministic values without considering the uncertainties caused by uncertain input parameters [31]. Therefore, studying the propagation of uncertainty in input parameters to simulation results becomes a necessity, which is the main objective of uncertainty quantification (UQ) process [16]. UQ approaches including polynomial

chaos (PC) methods, moment methods, and Monte Carlo methods have been applied to many kinds of single phase CFD simulations [24, 50, 58, 73], such as compressible flows [15, 46, 61, 62, 68,69,86,109], incompressible flows [54–56,74,85,116], non-isothermal flows [3,53,56,57,60,110], and flows with reactions [17,59,87,90–92]. However, for multiphase CFD simulations, a limited number of applications of UQ approaches are reported in the literature. Several works about the applications of UQ to flows in porous media are reported in literature [36,37,63]. For more complex system, such as gas-particle flows, few works can be found. Gel et al. built a surrogate model and performed UQ analysis in a bubbling fluidized bed [31] and a circulating fluidized bed [32]. Donato and Pitchumani proposed a UQ approach named QUICKER, and applied it to a a circulating fluidized bed and a turbulent fluidized bed [20].

UQ approaches can be either intrusive or non-intrusive. Intrusive UQ approach introduces the uncertainty into the governing equations, and only one set of model equations are solved. Hence, this method is usually computational efficient. However, for complex system, because a large amount of modifications to the governing equations are required, it is difficult to implement this method. Therefore, non-intrusive UQ approaches are often considered for complicated systems. Non-intrusive approaches treat the computational model as a black box. The space of the distribution of uncertain parameters is sampled first, and for each sample, the simulation is performed once. Therefore, the computational cost using non-intrusive UQ approaches scales up with the number of samples, and sampling strategy becomes essential. As described in Chapter 1, samples can be generated using random or deterministic sampling strategies. Random sampling strategies include the basic Monte Carlo method and its improvements such as importance sampling Monte Carlo method and Latin hypercube Monte Carlo method [24, 58]. The advantage of random sampling strategy is that it is efficient for problems with large amounts of uncertain input parameters, because the convergence of the method is independent of the number of random variables. However, the slow convergence of the higher order moments with respect to the number of samples results in a large number of samples required for a given accuracy, and therefore limits the implement of the method to computationally expensive problems [58]. On the other hand, the deterministic sampling strategies such as quadrature-based sampling strategy, can significantly reduce the number of

samples, hence reduce the computational time [73]. However, with increasing the number of random input parameters, the required number of samples increases exponentially, known as "the curse of dimensionality", which limits the applications of the method to problems with moderate number of random input variables [58, 73].

In this chapter, a non-intrusive quadrature-based uncertainty quantification (QBUQ) approach with reconstruction of the probability distribution function (PDF) of the system response, described in Chapter 2, is applied to a bubbling fluidized bed. A set of samples are generated for the PDF of the uncertain input parameter using Gaussian quadrature formulae [42]. The simulation results of each sample are used to directly estimate the moments of the system response by means of quadrature formulae [4, 119]. Then extended quadrature method of moments (EQMOM) [121] is used to reconstruct the PDF of the system response. With the QBUQ approach, not only confidence intervals for the system response can be provided, but the probability in particular of rare events can be evaluated as well. The remainder of this chapter is organized as follows. Section 3.2 gives an introduction to the numerical models used in this chapter to simulate the bubbling fluidized beds. Section 3.3 explains the theory of QBUQ and its implementation to an open source CFD code MFIX (Multiphase Flow with Interface eXchanges) (http://mfix.netl.doe.gov). Section 3.4 and Section 3.5 discuss the application of QBUQ to a bubbling fluidized bed. Section 3.6 concludes this chapter.

3.2 Numerical Models in Simulations of Bubbling Fluidized Beds

In simulations of bubbling fluidized beds, two kinds of models are mainly considered: Eulerian-Lagrangian models and Eulerian-Eulerian models [105, 107]. In Eulerian-Lagrangian models, the solid phase is represented by discrete particles. The motion of each particle is solved by Newton's second law, with a drag force closure for particle-gas interactions, and a collision model for particle-particle interactions. The fluid phase is continuous, and governed by Navier-Stokes equations with closures to account for interactions with discrete particle phase [18, 45, 106]. Although this discrete approach can describe the particle-particle and particle-wall interactions in a realistic way, it is usually computationally expensive, and hence limited to relatively small amount of particles and small scale reactors [18, 104, 105, 107]. In

Eulerian-Eulerian models, also known as two fluid models, both fluid and solid phases are treated as interpenetrating continua. This continuum approach is computationally more efficient than discrete method, and can be used to relatively large system. Both fluid and solid phases are governed by traditional Navier-Stokes equations with modifications to account for property exchange phenomena. The particle-gas interactions are described by drag force closures. Indirect properties such as solid pressure and viscosity which depend on closures are used to account for particle-particle interactions since discrete particles no longer exist [21, 45, 100, 105, 107]. The most widely used approach to obtain closures for particle-particle interactions is the kinetic theory of granular flows [40, 105, 107]. In this chapter, a bubbling fluidized bed is solved using an open-source multiphase CFD code MFIX developed by the U.S. Department of Energy's National Energy Technology Laboratory (NETL) with a two fluid model with kinetic theory closures for the solid phase.

3.2.1 Governing equations

The governing equations implemented into MFIX and used to solve the present bubbling fluidized bed are as follows [9, 99].

Continuity equations

Gas-phase continuity equation is

$$\frac{\partial}{\partial t}\left(\alpha_{\mathrm{g}}\rho_{\mathrm{g}}\right) + \nabla \cdot \left(\alpha_{\mathrm{g}}\rho_{\mathrm{g}}\mathbf{U}_{\mathrm{g}}\right) = 0, \tag{3.1}$$

where α_{g} is the gas volume fraction, ρ_{g} is the density of gas, and $\mathbf{U}_{\mathrm{g}}$ is the gas velocity field.

Solid-phase continuity equation is

$$\frac{\partial}{\partial t}\left(\alpha_{\mathrm{s}}\rho_{\mathrm{s}}\right) + \nabla \cdot \left(\alpha_{\mathrm{s}}\rho_{\mathrm{s}}\mathbf{U}_{\mathrm{s}}\right) = 0, \tag{3.2}$$

where α_{s} is the solid volume fraction with $\alpha_{\mathrm{g}} + \alpha_{\mathrm{s}} = 1$, ρ_{s} is the solid density, and $\mathbf{U}_{\mathrm{s}}$ is the solid velocity field.

Momentum equations

Gas-phase momentum equation is written as

$$\frac{\partial}{\partial t}\left(\alpha_{\mathrm{g}}\rho_{\mathrm{g}}\mathbf{U}_{\mathrm{g}}\right)+\nabla\cdot\left(\alpha_{\mathrm{g}}\rho_{\mathrm{g}}\mathbf{U}_{\mathrm{g}}\mathbf{U}_{\mathrm{g}}\right)=-\alpha_{\mathrm{g}}\nabla p_{\mathrm{g}}+\nabla\cdot\boldsymbol{\tau}_{\mathrm{g}}+\alpha_{\mathrm{g}}\rho_{\mathrm{g}}\mathbf{g}+K_{\mathrm{gs}}\left(\mathbf{U}_{\mathrm{s}}-\mathbf{U}_{\mathrm{g}}\right), \tag{3.3}$$

where p_{g} is the gas pressure, $\boldsymbol{\tau}_{\mathrm{g}}$ is the viscous stress tensor of the gas phase, $\mathbf{g}$ is the acceleration of gravity, and K_{gs} is the gas-solid drag coefficient.

Solid phase momentum equation is

$$\frac{\partial}{\partial t}\left(\alpha_{\mathrm{s}}\rho_{\mathrm{s}}\mathbf{U}_{\mathrm{s}}\right)+\nabla\cdot\left(\alpha_{\mathrm{s}}\rho_{\mathrm{s}}\mathbf{U}_{\mathrm{s}}\mathbf{U}_{\mathrm{s}}\right)=-\alpha_{\mathrm{s}}\nabla p_{\mathrm{g}}+\nabla\cdot\boldsymbol{S}_{\mathrm{s}}+\alpha_{\mathrm{s}}\rho_{\mathrm{s}}\mathbf{g}-K_{\mathrm{gs}}\left(\mathbf{U}_{\mathrm{s}}-\mathbf{U}_{\mathrm{g}}\right), \tag{3.4}$$

where $\boldsymbol{S}_{\mathrm{s}}$ is the solid phase stress tensor.

Gas-solid drag coefficient

Wen and Yu drag correlation [9, 112] for gas-solid interactions is used in the present work, and the drag coefficient is defined as

$$K_{\mathrm{gs}}=\frac{3}{4}C_D\frac{\rho_{\mathrm{g}}\alpha_{\mathrm{g}}\alpha_{\mathrm{s}}\left|\mathbf{U}_{\mathrm{s}}-\mathbf{U}_{\mathrm{g}}\right|}{d_{\mathrm{s}}}\alpha_{\mathrm{g}}^{-2.65}, \tag{3.5}$$

where

$$C_D=\begin{cases}\dfrac{24}{\mathrm{Re}}\left(1+0.15\,\mathrm{Re}\right)^{0.687} & \mathrm{Re}<1000\\ 0.44 & \mathrm{Re}\geq 1000\end{cases}, \tag{3.6}$$

with Reynolds number Re defined as

$$\mathrm{Re}=\frac{\rho_{\mathrm{g}}\alpha_{\mathrm{g}}\left|\mathbf{U}_{\mathrm{s}}-\mathbf{U}_{\mathrm{g}}\right|d_{\mathrm{s}}}{\mu_{\mathrm{g}}}, \tag{3.7}$$

where d_{s} is the particle diameter, and μ_{g} is the shear viscosity of gas.

Constitutive equations

Models of gas phase viscous stress tensor, solid phase stress tensor, and granular temperature shown below are applied in MFIX to close the momentum equations for both phases.

Gas phase viscous stress tensor

Gas phase stress tensor is defined as

$$\boldsymbol{\tau}_{\mathrm{g}} = \alpha_{\mathrm{g}}\mu_{\mathrm{g}}\left[\nabla\mathbf{U}_{\mathrm{g}} + (\nabla\mathbf{U}_{\mathrm{g}})^{\mathrm{T}}\right] + \alpha_{\mathrm{g}}\left(\lambda_{\mathrm{g}} - \frac{2}{3}\mu_{\mathrm{g}}\right)(\nabla\cdot\mathbf{U}_{\mathrm{g}})\,\mathbf{I}, \tag{3.8}$$

where λ_{g} is the bulk viscosity of gas which normally can be set to zero [10, 107], and $\mathbf{I}$ is the unit tensor.

Solid phase stress tensor

Two regimes, proposed by Johnson and Jackson [33, 49, 99] are used to describe the solid phase stress tensor $\boldsymbol{S}_{\mathrm{s}}$: plastic regime, and viscous regime. The model switches from one to another at a critical packing α_{g}^{*}, which is set to the packed bed void fraction. The solid phase stress tensor can be written as

$$\boldsymbol{S}_{\mathrm{s}} = \begin{cases} -p_{\mathrm{s}}^{\mathrm{p}}\mathbf{I} + \boldsymbol{\tau}_{\mathrm{s}}{}^{\mathrm{p}} & \alpha_{\mathrm{g}} \le \alpha_{\mathrm{g}}^{*} \\ -p_{\mathrm{s}}^{\mathrm{v}}\mathbf{I} + \boldsymbol{\tau}_{\mathrm{s}}{}^{\mathrm{v}} & \alpha_{\mathrm{g}} > \alpha_{\mathrm{g}}^{*} \end{cases}, \tag{3.9}$$

where superscript p represents plastic regime and v for viscous regime, p_{s} is the solids pressure, and $\boldsymbol{\tau}_{\mathrm{s}}$ is the granular stress tensor of solid phase.

The solids pressure in plastic regime is defined as

$$p_{\mathrm{s}}^{\mathrm{p}} = \alpha_{\mathrm{s}}p^{*}, \tag{3.10}$$

where $p^{*} = 10^{25}\left(\alpha_{\mathrm{g}}^{*} - \alpha_{\mathrm{g}}\right)^{10}$.

A model proposed by Schaeffer [95] is used to describe granular stress tensor in the plastic regime, written as

$$\boldsymbol{\tau}_{\mathrm{s}}{}^{\mathrm{p}} = 2\mu_{\mathrm{s}}^{\mathrm{p}}\mathbf{D}_{\mathrm{s}}, \tag{3.11}$$

where the strain rate tensor is

$$\mathbf{D}_{\mathrm{s}} = \frac{1}{2}\left[\nabla\mathbf{U}_{\mathrm{s}} + (\nabla\mathbf{U}_{\mathrm{s}})^{\mathrm{T}}\right]. \tag{3.12}$$

The solid phase viscosity in the plastic regime is defined as

$$\mu_{\mathrm{s}}^{\mathrm{p}} = \frac{p^* \sin\phi}{2\sqrt{I_{2D}}}, \tag{3.13}$$

where ϕ is the angle of internal friction, and I_{2D} is the second invariant of the deviator of the strain rate tensor, written as

$$I_{2D} = \frac{1}{6}\left[(\mathbf{D}_{\mathrm{s}11} - \mathbf{D}_{\mathrm{s}22})^2 + (\mathbf{D}_{\mathrm{s}22} - \mathbf{D}_{\mathrm{s}33})^2 + (\mathbf{D}_{\mathrm{s}33} - \mathbf{D}_{\mathrm{s}11})^2\right] + \mathbf{D}_{\mathrm{s}12}^2 + \mathbf{D}_{\mathrm{s}23}^2 + \mathbf{D}_{\mathrm{s}31}^2. \tag{3.14}$$

In the viscous regime, granular temperature Θ_{s} is introduced to describe solids pressure and granular stress. The solids pressure is given in [40] as

$$p_{\mathrm{s}}^{\mathrm{v}} = \rho_{\mathrm{s}}\alpha_{\mathrm{s}}\Theta_{\mathrm{s}} + K_1\alpha_{\mathrm{s}}^2\Theta_{\mathrm{s}}, \tag{3.15}$$

where Θ_{s} is the granular temperature, and K_1 is written as

$$K_1 = 2(1 + e_{\mathrm{pp}})\rho_{\mathrm{s}} g_0, \tag{3.16}$$

with e_{pp} being particle-particle restitution coefficient, and g_0 being radial distribution function defined as

$$g_0 = \left[1 - \left(\frac{\alpha_{\mathrm{s}}}{\alpha_{\mathrm{s,max}}}\right)^{\frac{1}{3}}\right]^{-1}, \tag{3.17}$$

where $\alpha_{\mathrm{s,max}}$ is the packing limit.

The granular stress tensor of solid phase in the viscous regime $\boldsymbol{\tau_{\mathrm{s}}}^{\mathrm{v}}$ is defined as

$$\boldsymbol{\tau_{\mathrm{s}}}^{\mathrm{v}} = 2\mu_{\mathrm{s}}^{\mathrm{v}}\mathbf{D}_{\mathrm{s}} + \lambda_{\mathrm{s}}^{\mathrm{v}}\,\mathrm{tr}(\mathbf{D}_{\mathrm{s}})\mathbf{I}, \tag{3.18}$$

where the solids bulk viscosity $\lambda_{\mathrm{s}}^{\mathrm{v}}$ and shear viscosity $\mu_{\mathrm{s}}^{\mathrm{v}}$ are given in the following equations, and the strain rate tensor $\mathbf{D}_{\mathrm{s}}$ has the same definition as in the plastic regime shown in Eq. 3.12.

The equation for solids bulk viscosity is written as

$$\lambda_{\mathrm{s}}^{\mathrm{v}} = K_2\alpha_{\mathrm{s}}\sqrt{\Theta_{\mathrm{s}}}, \tag{3.19}$$

where K_2 is a constant given as

$$K_2 = \frac{4d_{\mathrm{s}}\alpha_{\mathrm{s}}\rho_{\mathrm{s}}(1 + e_{\mathrm{pp}})g_0}{3\sqrt{\pi}} - \frac{2}{3}K_3, \tag{3.20}$$

with K_3 being a constant written as

$$K_3 = \frac{d_s \rho_s}{2}\left\{\frac{\sqrt{\pi}}{3(3-e_{pp})}\left[0.5(3e_{pp}+1)+0.4(1+e_{pp})(3e_{pp}-1)\alpha_s g_0\right] + \frac{8\alpha_s g_0(1+e_{pp})}{5\sqrt{\pi}}\right\}. \quad (3.21)$$

The shear viscosity of the solid phase μ_s^v is defined as

$$\mu_s^v = K_3 \alpha_s \sqrt{\Theta_s}. \quad (3.22)$$

An algebraic granular energy equation derived from the energy equation of Lun et al. [64] is implemented in MFIX [99], and is used in the present work. The granular temperature Θ_s is solved as

$$\Theta_s = \left\{\frac{-K_1\alpha_s \operatorname{tr}(\mathbf{I}_s) + \sqrt{K_1^2\alpha_s^2 \operatorname{tr}^2(\mathbf{D}_s) + 4K_4\alpha_s\left[K_2 \operatorname{tr}^2(\mathbf{D}_s) + 2K_3 \operatorname{tr}(\mathbf{D}_s^2)\right]}}{2K_4\alpha_s}\right\}^2, \quad (3.23)$$

where constant K_4 is given as

$$K_4 = \frac{12(1-e_{pp}^2)\rho_s g_0}{d_s\sqrt{\pi}}. \quad (3.24)$$

With above equations, the system is closed, and the bubbling fluidized bed can be solved.

3.3 Theory of Quadrature-Based Uncertainty Quantification Approach with Reconstruction of the PDF of the System Response

As described in Section 3.2, all models present a strongly non-linear relationship between input parameters and simulation outputs. The input parameters can be affected by uncertainties caused by such as difficulties in the measurements, and assumptions made to derive models or closures. These uncertainties in input parameters can influence the simulation results with consequences to predict the quantities of interest for real applications. Therefore, the propagation of uncertainties from model input parameters to computational outputs need to be studied. In this chapter, a non-intrusive QBUQ approach with the reconstruction of the PDF of the system response proposed in Chapter 2 is adopted.

3.3.1 Quadrature-based UQ approach

In the non-intrusive UQ approaches, the computational cost depends on the number of samples, which sometimes can be large [58]. It is thus clear that the sampling strategy is crucial for non-intrusive UQ approaches to reduce the number of samples without losing the accuracy of the UQ procedure. The foundation of the quadrature-based UQ approach is to directly evaluate the moments of the system response [4, 119] by Gaussian quadrature formulae [42]. The sampling procedure is illustrated in Appendix A [29, 42].

For each sample, the simulation is performed once, whose results are used to estimate the moments of quantities of interest. Once the moments of the system response are obtained, the statistics of the response can be calculated using Eqs. 2.3 to 2.6. The set of moments of the response can also be used to reconstruct the PDF of the response using extended quadrature method of moments (EQMOM) [121]. The foundation of EQMOM is to represent the approximated PDF of the response $f(\kappa)$ as a weighted sum of N non-negative kernel functions [14,121]:

$$f_N(\kappa) = \sum_{i=1}^{N} \rho_i \delta_\sigma(\kappa, \kappa_i), \tag{3.25}$$

where ρ_i and κ_i are the i-th quadrature weight and node used in the reconstruction of the PDF, and $\delta_\sigma(\kappa, \kappa_i)$ is a kernel density function. The choice of $\delta_\sigma(\kappa, \kappa_i)$ depends on the properties of the distribution that needs to be reconstructed, specifically on the support of the distribution. A beta distribution is chosen for distributions on bounded interval $[a, b]$; for distributions on semi-finite interval $[a, +\infty)$, a gamma distribution can be used; for distributions on the whole real set, Gaussian distribution is chosen. Details about the EQMOM method for these three kernel density functions can be found in Appendix C and in the literature [14, 121]. The key advantage of the proposed quadrature-based UQ approach is that not only the statistics of the system response are provided, but the PDF of the response is provided as well, which can be used to evaluate the probability of critical events.

3.3.2 Implementation of the quadrature-based UQ approach into MFIX

Two separate modules based on the Python programming language and shell scripts are developed to implement the quadrature-based UQ approach into MFIX, including a pre-processing

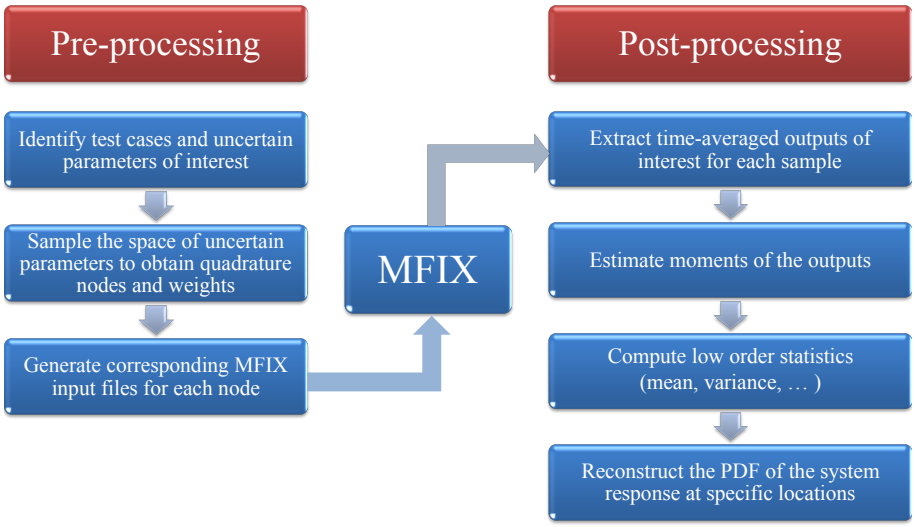

Figure 3.1 Framework of implementation of quadrature-based UQ approach into MFIX.

module and a post-processing module. The framework of the implementation is shown in Fig. 3.1.

In the pre-processing module, the script first identifies the properties of uncertain input parameters, such as PDF of the parameters, and lower and upper bounds of the parameters. Quadrature weights and nodes are generated next, with which the script creates corresponding MFIX input files for each sample, stored in separate directories.

Once the simulations for each sample are completed, the script in the post-processing module can extract time-averaged quantities of interest for each sample. The set of moments can be directly evaluated with these time-averaged results for each sample and quadrature weights generated by the pre-processing module using Gaussian quadrature formulae [42]. With the set of moments, statistics of the response, such as mean, variance, skewness, and kurtosis can be calculated, and the PDF of the response can be reconstructed using EQMOM [14, 121].

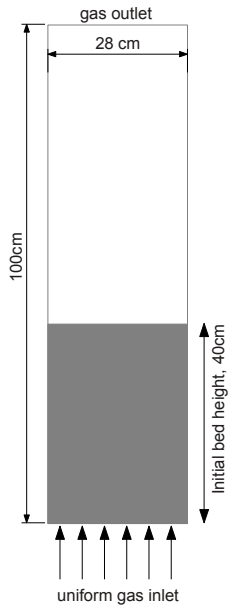

Figure 3.2 Scheme of the bubbling fluidized bed.

3.4 Descriptions of the Computational Problem and the Uncertain Parameters

The QBUQ procedure was demonstrated by considering a bubbling fluidized bed studied in Taghipour et al. [100] experimentally and computationally as an example application. Details about the simulation setup are in the following section.

3.4.1 Descriptions of the computational problem

A two-dimensional bubbling fluidized bed is simulated in the present work, with scheme shown in Fig. 3.2. The column is 28 cm in width, and 100 cm in height. Spherical glass beads with density 2500 kg/m^3 and mean diameter 275 μm are fluidized by injecting the air uniformly from the bottom of the column at 0.38 m/s at ambient conditions. The computational domain is discretized by 44800 (112×400) cells, with the grid interval spacing being 0.25 cm. The adaptive time stepping of MFIX is applied with starting time step being 1.0×10^{-4} s. The maximum number of iterations per time step is set to 500, and the convergence criteria for residual components are 1.0×10^{-3}. The initial bed height is 0.4 m, and initial void fraction is 0.4. The inlet and outlet boundary conditions are constant gas inflow, and zero relative gas

pressure, respectively. No-slip wall boundary condition is applied to both gas and solid phases. The particle-particle restitution coefficient is set to 0.9 for all simulations in this work. The governing equations needed to solve this system are described in Section 3.2.1. The parameters and conditions used in the simulations are summarized in Table. 3.1.

Table 3.1 Simulation parameters and conditions.

Properties	Values
Gas density	1.225 kg/m^3
Particle density	2500 kg/m^3
Mean particle diameter	275 μm
Restitution coefficient	0.9
Initial bed height	0.4 m
Initial void fraction	0.4
Superficial gas velocity	0.38 m/s
Inlet boundary condition	constant gas inflow
Exit boundary condition	zero relative gas pressure
Grid interval spacing	0.25 cm
Simulation time	90 s
Starting time steps	1.0×10^{-4} s
Maximum number of iterations	500
Convergence criteria	1.0×10^{-3}

3.4.2 Descriptions of the uncertain parameter

The influence of uncertain particle size on the simulation results is studied. In practice, a distribution of particle size exists constantly. In this work, a uniform distribution is assumed for the distribution of particle diameter. The mean particle diameter d_s is 275 μm, and the standard deviation is $0.3d_\mathrm{s}$, which indicates the particle diameter is distributed uniformly on the interval $[192.5, 357.5]$. Using the pre-processing module illustrated in Section 3.3.2, 20 samples are generated. Results are discussed in the next section.

3.5 Results and Discussion

Three time-averaged quantities of interest are studied to evaluate the effects of uncertain particle size on the simulation outputs, including solid volume fraction α_s, gas pressure p_s, and vertical solid velocity v_s. Moments of the quantities are computed directly using the

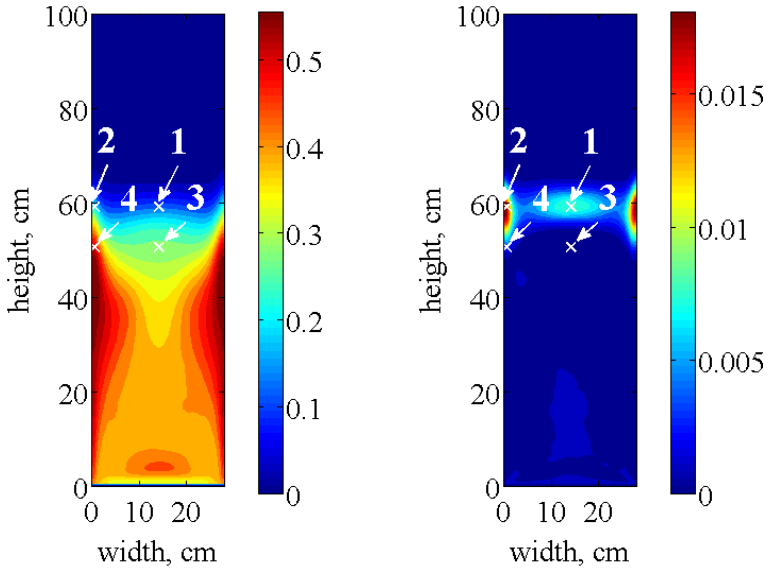

(a) mean $\mu(\alpha_s)$ (b) variance $\sigma^2(\alpha_s)$

Figure 3.3 Contour plots of (a) mean and (b) variance of the solid volume fraction.

Gaussian quadrature formulae, mentioned in Section 3.3. Contour plots are plotted for moments up to fourth order, and for statistics like mean and variance of the system response. The approximated PDFs of the response are reconstructed at specific locations using EQMOM [121].

3.5.1 Solid volume fraction α_s

Fig. 3.3 shows the contour plots of the mean and variance of the solid volume fraction α_s, with symmetrical profiles shown. The effect of uncertain particle size on the solid volume fraction α_s focuses on the interface of the bed, in particular on locations near the wall. Contour plots of moments up to fourth order of solid volume fraction are also reported in Fig. 3.4.

Four sets of data at varied locations are used to reconstruct the PDF of the system response, two on the centerline (locations 1 and 3), and two near the wall (locations 2 and 4). Locations 1 and 2 are at height near the interface of the bed, while locations 3 and 4 are in the fluidized bed. If not noted otherwise, the designated locations in all figures in this chapter are the same. Table 3.2 lists the coordinates of these four locations.

The reconstructed PDFs of solid volume fraction α_s at these four locations are shown in

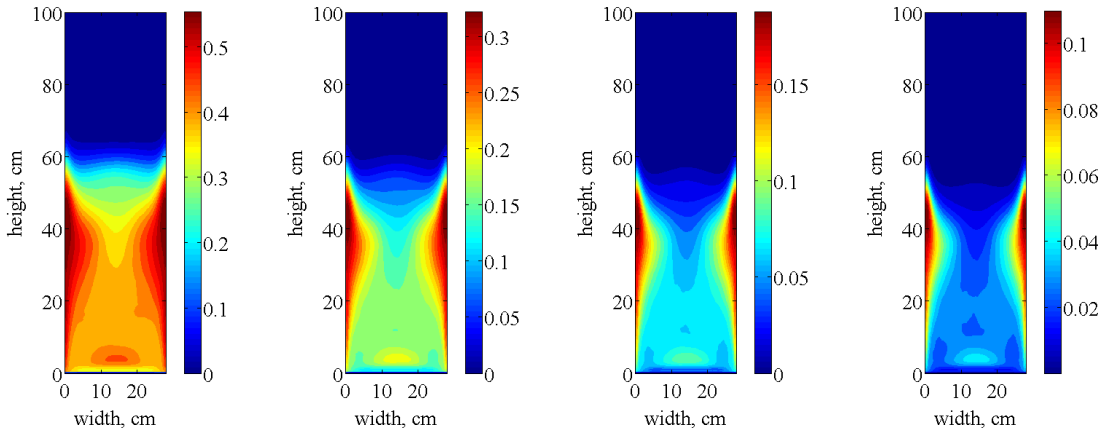

(a) m_1 (b) m_2 (c) m_3 (d) m_4

Figure 3.4 Contour plots of moments of solid volume fraction from first order to fourth order: (a) m_1, (b) m_2, (c) m_3, (d) m_4.

Table 3.2 Coordinates of the designated locations.

Location	Coordinates	
	x	y
1	14.125	59.125
2	0.625	59.125
3	14.125	50.625
4	0.625	50.625

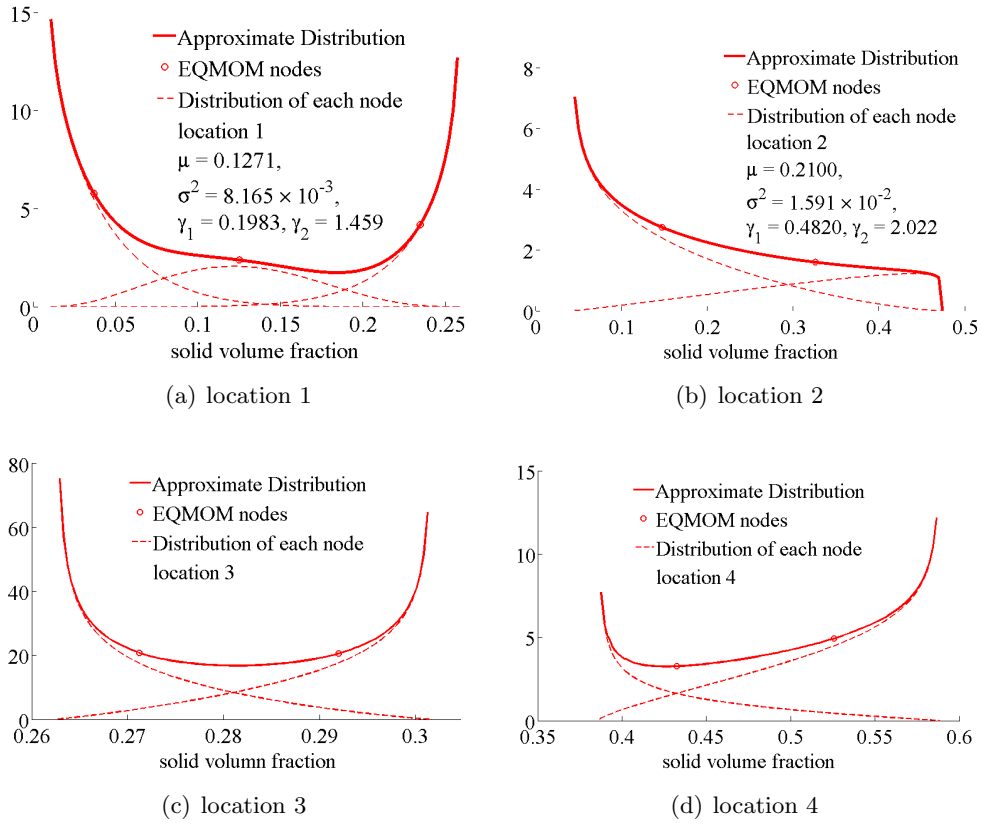

(a) location 1 (b) location 2

(c) location 3 (d) location 4

Figure 3.5 Reconstructed PDFs of the solid volume fraction. Statistics of α_s at locations 1 and 2 are given: μ, σ^2, γ_1, and γ_2 are mean, variance, skewness, and kurtosis, respectively.

Fig. 3.5. At locations 1 and 3, either low or high solid volume fraction is preferable. At location 2, lower solid volume fraction has larger probability because when near the wall at this height, particles can barely reach this height, and are moving downward, which is shown in Section 3.5.3 later. At location 4, higher solid volume fraction has larger probability, which indicates particles tend to accumulate at this location.

3.5.2 Gas pressure p_g

Contour plots of the mean and variance of gas pressure are shown in Fig. 3.6, and moments of gas pressure up to fourth order are shown in Fig. 3.7. The symmetrical profiles are observed as well. The effect of uncertain particle size on gas pressure concentrates on the interface of the bed, especially at locations near the wall, which is consistent with conclusions in Section 3.5.1.

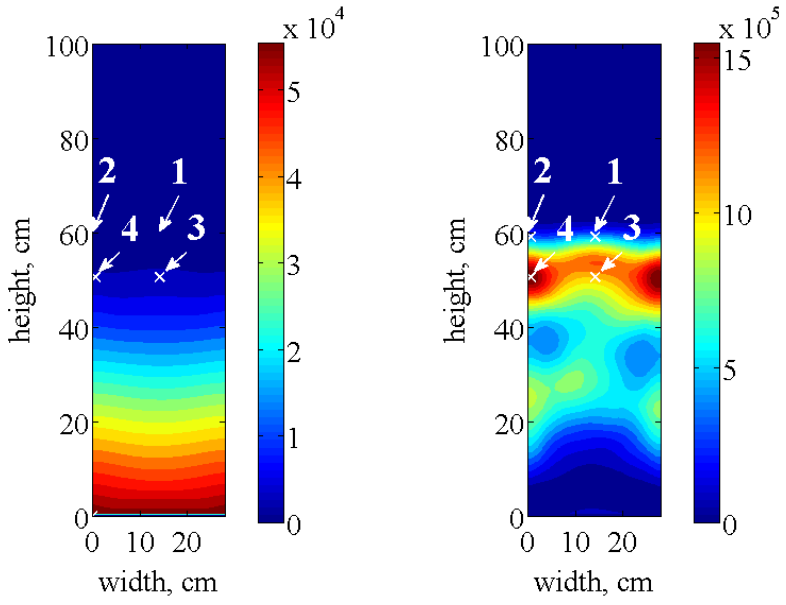

(a) mean $\mu(p_g)$ (b) variance $\sigma^2(p_g)$

Figure 3.6 Contour plots of (a) mean and (b) variance of the gas pressure.

Approximated PDFs of gas pressure are also reconstructed at the same locations, shown in Fig. 3.8. For locations 1 and 2, low gas pressure is preferred because at this height particle concentration is very low. At lower positions, such as locations 3 and 4, though low gas pressure still has large probability, the shape of the PDFs is broader.

3.5.3 Vertical solid velocity v_s

Fig. 3.9 and Fig. 3.10 show the contour plots of mean and variance of vertical solid velocity, and moments from first order to fourth order of v_s, with symmetrical profiles observed. At locations near the centerline of the reactor, particles are moving upward, while near the wall negative vertical velocities are observed, which indicates circulation of particles is formed inside the reactor. Again, at the interface of the bed, specifically near the wall, uncertain particle size influences the results the most.

The approximated PDFs of vertical solid velocity are reconstructed at the same locations, shown in Fig. 3.11. At location 1, particles tend to move downward. At location 2, particles are

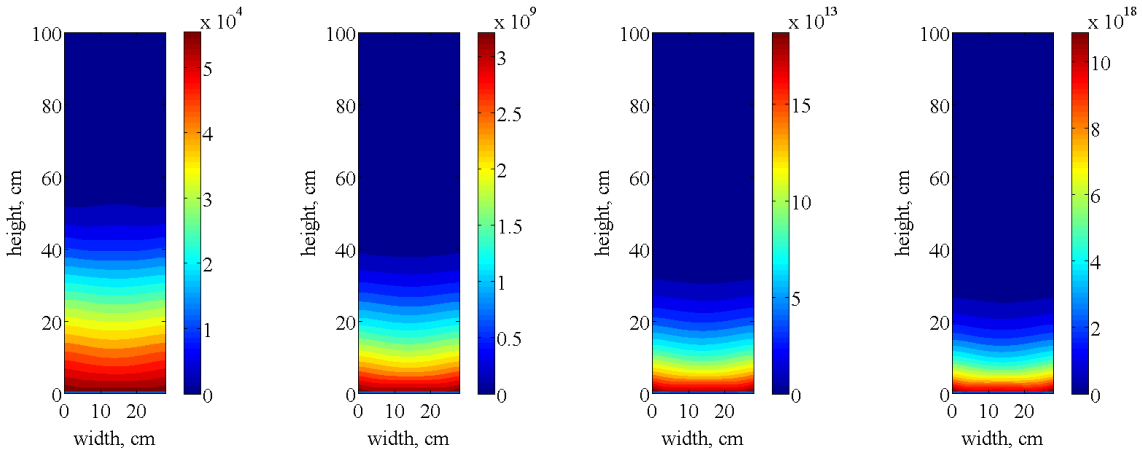

(a) m_1 (b) m_2 (c) m_3 (d) m_4

Figure 3.7 Contour plots of moments of gas pressure from first order to fourth order: (a) m_1, (b) m_2, (c) m_3, (d) m_4.

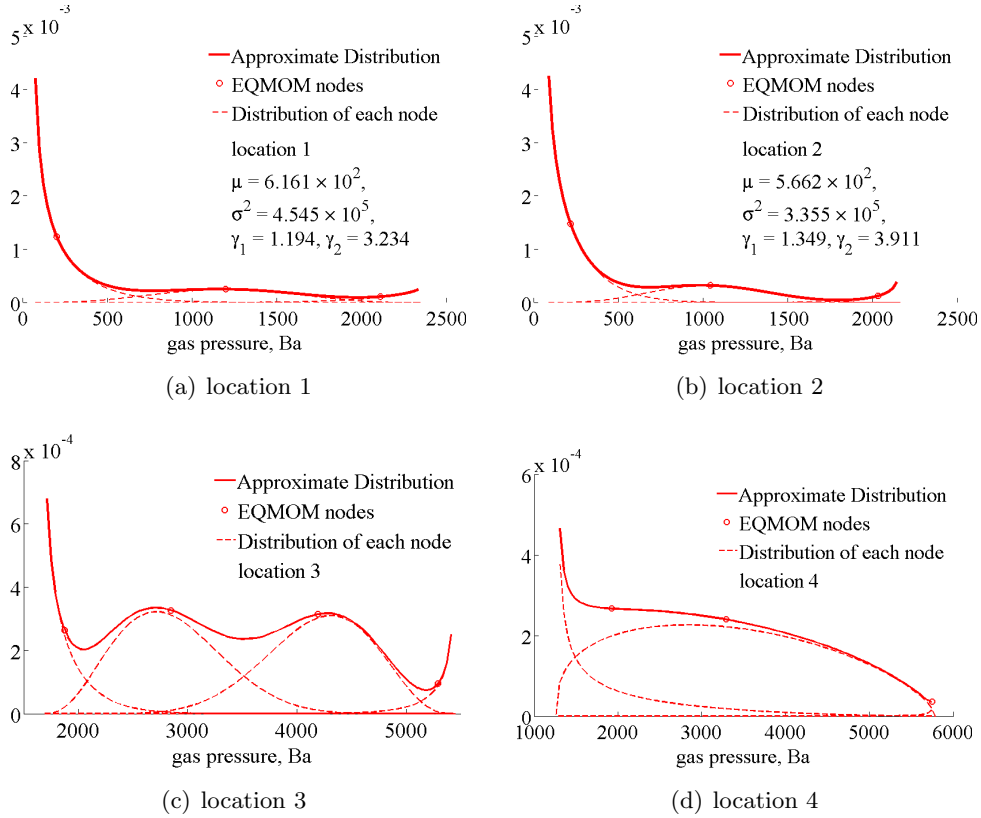

(a) location 1 (b) location 2

(c) location 3 (d) location 4

Figure 3.8 Reconstructed PDFs of the gas pressure. Statistics of p_g at locations 1 and 2 are given: μ, σ^2, γ_1, and γ_2 are mean, variance, skewness, and kurtosis, respectively.

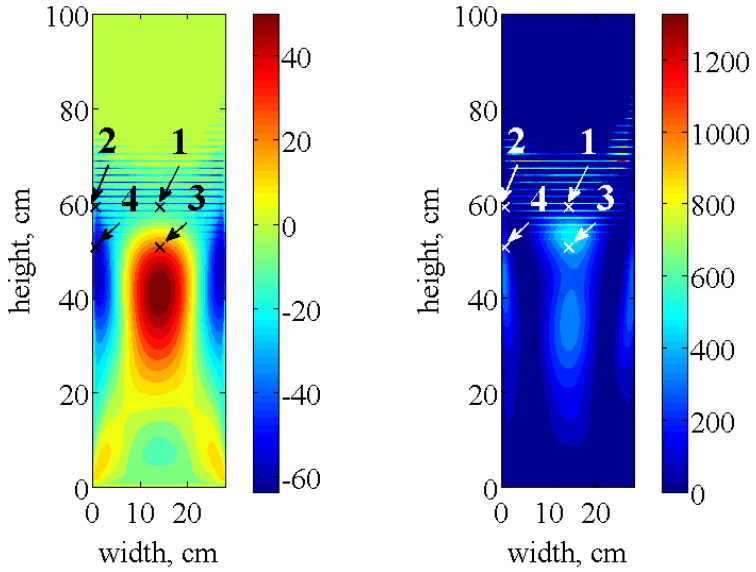

(a) mean $\mu(v_s)$ (b) variance $\sigma^2(v_s)$

Figure 3.9 Contour plots of (a) mean and (b) variance of the vertical solid velocity.

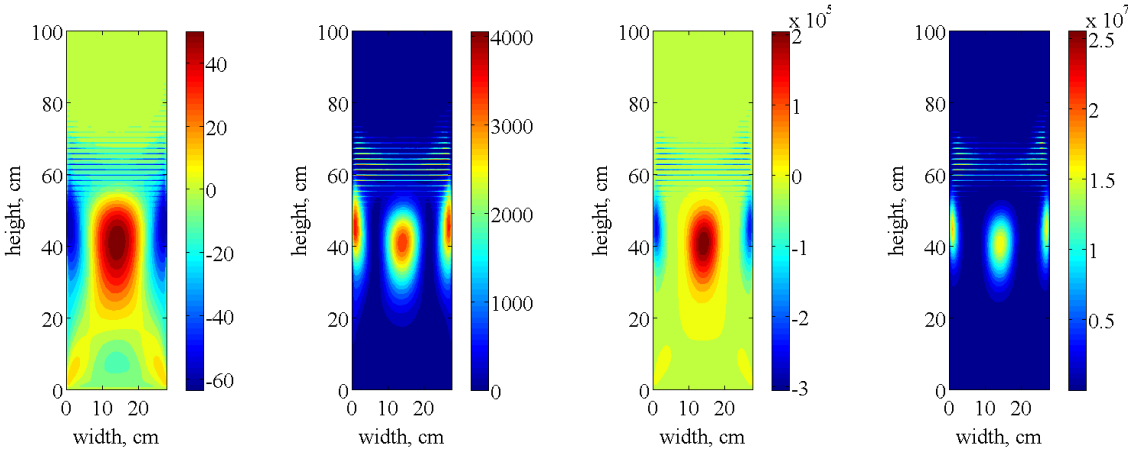

(a) m_1 (b) m_2 (c) m_3 (d) m_4

Figure 3.10 Contour plots of moments of vertical solid velocity from first order to fourth order: (a) m_1, (b) m_2, (c) m_3, (d) m_4.

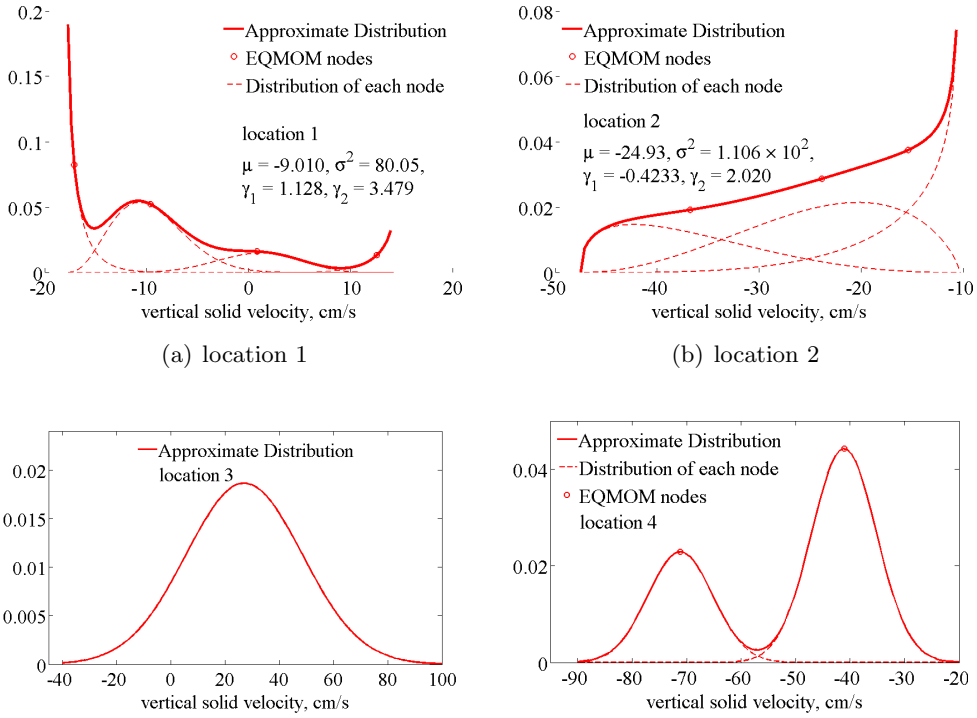

(a) location 1

(b) location 2

(c) location 3

(d) location 4

Figure 3.11 Reconstructed PDFs of the vertical solid velocity. Statistics of v_s at locations 1 and 2 are given: μ, σ^2, γ_1, and γ_2 are mean, variance, skewness, and kurtosis, respectively.

going downward, and low vertical velocity is preferable because no-slip wall boundary condition was applied. At location 3, PDF with a broad peak is reconstructed, and positive vertical solid velocity is preferred. At location 4, particles have negative vertical velocity. Because of no-slip wall boundary condition for the solid phase, lower vertical velocity has larger probability.

3.6 Conclusions

A non-intrusive quadrature-based uncertainty quantification approach with reconstruction of the distribution of the system response is presented in this work, and is applied to a bubbling fluidized bed with uncertain particle diameter. Contour plots of mean, variance and moments up to fourth order of solid volume fraction, gas pressure, and vertical solid velocity are shown, with symmetrical profiles observed. Results indicate that the influences of the uncertain particle size on the simulation outputs focus on the interface of the bed, in particular on locations

near the wall. Approximated probability distribution functions of the system response are reconstructed successfully at specific locations. The approach illustrated in this work can be extended to multi-variate problems.

CHAPTER 4. APPLICATION OF QUADRATURE-BASED UNCERTAINTY QUANTIFICATION TO THE NETL SMALL-SCALE CHALLENGE PROBLEM SSCP-I

Modified from a paper submitted to Powder Technology, 2014.

Xiaofei Hu, Alberto Passalacqua, and Rodney O. Fox

Non-intrusive quadrature-based uncertainty quantification with reconstruction of the distribution of the system response is introduced and applied to the simulation of dense fluidized beds. This approach relies on the conditional quadrature method of moments (CQMOM) to generate a set of samples of the distribution of multiple uncertain parameters of the model. The moments of the system response are directly estimated using Gaussian quadrature formulae, and are used to reconstruct an approximate distribution of the response using extended quadrature method of moments (EQMOM). The approach is demonstrated by considering a bubbling fluidized bed with two uncertain parameters. Contour plots of the mean and standard deviation of volume fraction, phase velocity and pressure are provided. The probability distribution functions of the response are reconstructed using EQMOM with appropriate kernel density functions. The simulation results are compared to experimental data provided by the 2013 NETL small-scale challenge problem.

4.1 Introduction

Gas-fluidized beds are widely used in industrial processes, such as combustion and gasification, catalytic cracking, and coating [8, 51, 118]. Computational fluid dynamics (CFD) provides a useful tool to study gas-solid fluidized beds, from understanding the fundamental

knowledge inside the reactor to helping design and scale-up the process [105, 107]. Due to the large separation of modeling scales, three approaches with different modeling levels can be found in the literature. The approach at the most detailed level is the direct numerical simulation (DNS) [45,106], which studies the particle-particle and gas-particle interactions directly. This approach can provide closure models for more coarse-grained models. Discrete particle modeling (DPM) and discrete element modeling (DEM) are approaches that operated at an intermediate level, which studies the particle-particle and particle-wall interactions in a realistic way but using closure models for gas-particle interactions [18, 45, 106]. At a coarser level, two fluid models (TFM) are widely used, which treat both solid and gas phases as continua, with closure models for particle-particle and gas-particle interactions [45, 106, 107].

Independently from the approach chosen to model gas-particle flows, each model is affected by uncertainty. Code and solution verification aim at ensuring that the correct numerical algorithm is used to accurately solve the equations of the mathematical model [16, 94]. Validation ensures that models represent the true physical system they aim at describing [16,94]. However, in most of CFD work, the predicted results are provided as deterministic values without confidence intervals [31] to account for the uncertainty in the inputs to the simulation. Studying the effects of uncertain inputs on the simulation results is a necessity, in order to ensure that the effect of input uncertainty are properly represented by the model. The objective of uncertainty quantification (UQ) is to evaluate the overall uncertainties associated to the prediction of the quantities of interest. In particular it studies the propagation of input uncertainties to the outputs of the models [16]. Either an intrusive or a non-intrusive approach can be used to perform UQ analysis. The intrusive UQ approach directly introduces the uncertainty into the system by reformulating the model equations. Although this method is computationally efficient because only one set of mathematical equations needs to be solved, it is also challenging to implement into complex systems due to the requirement of large amounts of modifications to the computational models. Therefore, non-intrusive UQ approaches that leave the computational model unchanged are usually considered for practical applications. The computational cost of non-intrusive approaches depends on the number of samples since for each sample the simulation is performed once. Therefore, an effective sampling strategy is crucial. Samples can

be generated using random or deterministic sampling strategies. The former are based on the Monte Carlo method [58], which is convenient for a large number of random input parameters because the convergence of the method is independent of the dimensionality of the space of random variables. However, the method is known for its slow convergence of high-order moments with respect to the number of samples [58]. Improvements to the Monte Carlo method are reported in the literature to reduce the required number of samples, such as importance sampling Monte Carlo method and Latin hypercube Monte Carlo method [24]. However, these methods become limited for computationally expensive problems. On the contrary, deterministic quadrature-based sampling strategies can significantly reduce the required number of samples, therefore reducing the computational cost [73]. However, these approaches become inefficient for problems with a large number of uncertain parameters because the required number of samples increases exponentially with the number of random variables. Therefore, these methods are limited to problems with a moderate number of uncertain parameters.

Many applications of UQ approaches such as polynomial chaos (PC), moment methods, and Monte Carlo methods to single-phase CFD simulations have been reported [24, 50, 58, 73], including compressible flows [15, 46, 61, 62, 68, 69, 86, 109], incompressible flows [54–56, 74, 85, 116], non-isothermal flows [3, 53, 56, 57, 60, 110], and reacting flows [17, 59, 87, 90–92]. However, applications of UQ approaches to multiphase CFD simulations are very limited. Although applications of UQ to flows in porous media are reported in the literature [36, 37, 63], for more complex systems such as gas-solid flows, few works can be found. Gel et al. [31] built a surrogate model based on data-fitted response surface for a bubbling fluidized bed. Then forward propagation of input uncertainty was studied by using the Monte Carlo method. In another work done by Gel et al. [32], the uncertainty in the outputs of a circulating fluidized bed caused by spatial discretization, time averaging, uncertain input parameters, and surrogate model was studied. In Donato and Pitchumani [20], a non-intrusive methodology called QUICKER was proposed, and was applied to a circulating fluidized bed and a turbulent fluidized bed.

In this chapter, non-intrusive quadrature-based uncertainty quantification (QBUQ), first proposed by Yoon et al. [4, 119], is adopted to estimate the moments of the system response

directly. This approach relies on Gaussian quadrature formulae [42] and on the conditional quadrature method of moments (CQMOM) [120] to generate a set of samples for the distribution of the uncertain parameters of the model. A numerical simulation is performed for each sample, and the moments of the system response are directly evaluated from the simulation results by means of quadrature formulae [4, 119]. These moments are then used to reconstruct the probability distribution function (PDF) of the system response using the extended quadrature method of moments (EQMOM) [121]. The proposed QBUQ approach with the reconstruction of the PDF of the outputs is then applied to a bubbling fluidized bed. For each system response, confidence intervals are provided, and the PDF is reconstructed at specific locations in the computational domain. The simulation results are also compared to the experimental data of the small-scale challenge problem (SSCP-I) proposed by the National Energy Technology Laboratory (NETL) [75].

4.2 Quadrature-Based Uncertainty Quantification Approach

The founding idea of QBUQ approach is to directly estimate the moments of the system response using Gaussian quadrature formulae [4, 119]. To illustrate the method, a random process $\kappa(\boldsymbol{\xi})$ with N random variables $\boldsymbol{\xi}$ is considered. A probability space $\mathcal{P}(\Omega, \mathfrak{F}, P)$ is defined by a sample space Ω, a sigma-algebra $\mathfrak{F}$, which is a non-empty collection of subsets of Ω, and a probability measure P on $(\Omega, \mathfrak{F})$. The objective of the approach is to estimate the moments of the system response, defined as

$$m_n = \langle \kappa(\boldsymbol{\xi})^n \rangle = \int_\Omega \kappa(\boldsymbol{\xi})^n p(\boldsymbol{\xi}) \mathrm{d}\boldsymbol{\xi}, \tag{4.1}$$

where $p(\boldsymbol{\xi})$ relies on the probability measure P. This is achieved by means of Gaussian quadrature formulae [4, 119], whose weights and nodes are found with different methods based on the number of the random variables. For the univariate problem, Ω is sampled using a one-dimensional Gaussian quadrature formula [42]; for multiple random variables, quadrature weights and nodes are obtained by sampling Ω using CQMOM [120]. These methods are discussed in this section.

4.2.1 QBUQ for one random variable

We consider $p(\xi)$ as the weight function for the univariate ($N = 1$) problem. The integral shown in Eq. 4.1 is approximated by an M-node Gaussian quadrature formula:

$$m_n = \int_\Omega \kappa(\xi)^n p(\xi) \mathrm{d}\xi \approx \sum_{i=1}^{\mathrm{M}} w_i \kappa(\xi_i)^n, \tag{4.2}$$

where w_i and ξ_i are the quadrature weights and nodes respectively. If the PDF of the random variable can be treated as a classical weight function, quadrature weights and nodes can be easily obtained using existing quadrature rules, which means ξ_i are the roots of the orthogonal polynomials associated to the weight function, and w_i can be calculated accordingly [29]. For example, the Gauss-Hermite quadrature rule can be used for a random variable with Gaussian distribution, while, if ξ is uniformly distributed, the Gauss-Legendre quadrature rule can be applied. If $p(\xi)$ cannot be considered as one of the classical weight functions, or only the moments with respect to ξ from zeroth order to order $2\mathrm{M} - 1$ are known, the quadrature weights and nodes can be determined by solving an eigenvalue problem [29, 42]. The monic orthogonal polynomials associated with the weight function are defined by a recurrence relation:

$$\begin{aligned} &Q_{-1}(\xi) = 0, \\ &Q_0(\xi) = 1, \\ &Q_{r+1}(\xi) = (\xi - \alpha_r) Q_r(\xi) - \beta_r Q_{r-1}(\xi),\ \beta_r > 0, \end{aligned} \tag{4.3}$$

where the coefficients α_r and β_r can be computed from the moments using Wheeler's algorithm [29, 88]. A symmetric tridiagonal matrix, named the Jacobi matrix, can then be constructed (Eq. 4.4) using the coefficients of the recurrence relation,

$$\mathbf{J}_{\mathrm{M}} = \begin{pmatrix} \alpha_0 & \sqrt{\beta_1} & & & 0 \\ \sqrt{\beta_1} & \alpha_1 & \sqrt{\beta_2} & & \\ & \ddots & \ddots & \ddots & \\ & & \sqrt{\beta_{\mathrm{M}-2}} & \alpha_{\mathrm{M}-2} & \sqrt{\beta_{\mathrm{M}-1}} \\ 0 & & & \sqrt{\beta_{\mathrm{M}-1}} & \alpha_{\mathrm{M}-1} \end{pmatrix}, \tag{4.4}$$

whose eigenvalues are the quadrature nodes of the M-node Gaussian quadrature formulae [29, 42], and the corresponding quadrature weights can be computed as

$$w_i = \beta_0 v_{i,1}^2,\ i = 1, \ldots, \mathrm{M}, \tag{4.5}$$

where $v_{i,1}$ is the first component of the eigenvector $\mathbf{v}_i$ of $\mathbf{J}_\mathrm{M}$, and

$$\beta_0 = \int_I w(\xi)\mathrm{d}\xi,$$

with I being the integration interval.

4.2.2 QBUQ for multiple random variables

For multiple random variables ($N \geq 2$), the space Ω is sampled using a moment-inversion procedure called conditional quadrature method of moments (CQMOM), proposed by Yuan and Fox [120]. The foundation of the method is to compute the conditional moments from the pure moments by solving a linear system, and to use Wheeler's algorithm to find the conditional weights and nodes from the conditional moments. In this way, a multi-dimensional problem is decomposed into several one-dimensional moment-inversion problems, which can be easily solved. In the remainder of this section, a bivariate problem ($N = 2, \boldsymbol{\xi} = (\xi_1, \xi_2)$) is used as an example to illustrate the method, while interested readers can find the details of the approach for a higher number of variables in the literature [120].

The joint PDF of the uncertain parameters ξ_1 and ξ_2 can be written as in Eq. 4.6 using the chain rule of conditional probability:

$$p(\xi_1, \xi_2) = p(\xi_2|\xi_1)p(\xi_1), \tag{4.6}$$

where $p(\xi_2|\xi_1)$ is the conditional PDF of ξ_2 given a fixed value of ξ_1, and $p(\xi_1)$ is the marginal PDF of ξ_1. The j-th order conditional moments obtained from the conditional PDF are defined as

$$\langle \xi_2^j \rangle(\xi_1) = \int \xi_2^j p(\xi_2|\xi_1)\mathrm{d}\xi_2. \tag{4.7}$$

Then the pure moments of order $(i + j)$ of the joint PDF of the uncertain parameters can be expressed as:

$$m_{i,j}^{i+j} = \int_\Omega \xi_1^i \xi_2^j p(\xi_1, \xi_2)\mathrm{d}\xi_1\mathrm{d}\xi_2 = \int \xi_1^i \langle \xi_2^j \rangle(\xi_1) p(\xi_1)\mathrm{d}\xi_1. \tag{4.8}$$

These pure moments are assumed to be known to sample the space of the uncertain parameters so that quadrature weights and nodes can be obtained.

The space of the first parameter ξ_1 can be sampled with an M_1-node one-dimensional Gaussian quadrature formula, as discussed in Section 4.2.1 [29, 42]. The quadrature weights w_{l_1} and nodes ξ_{1,l_1} are obtained from the pure moments $m_{i,0}^i$ with $i = 0, 1, \ldots, 2\mathrm{M}_1 - 1$ using the adaptive Wheeler algorithm proposed in [120]. Then, an M_1-point distribution representation of the marginal PDF $p(\xi_1)$ can be written as

$$p(\xi_1) = \sum_{l_1=1}^{\mathrm{M}_1} w_{l_1} \delta(\xi_1 - \xi_{1,l_1}). \tag{4.9}$$

The next step is to compute the conditional moments $\langle \xi_2^j \rangle (\xi_{1,l_1})$ with $j = 1, 2, \ldots, 2\mathrm{M}_2 - 1$ for each ξ_{1,l_1} to determine conditional quadrature weights w_{l_1,l_2} and nodes ξ_{2,l_1,l_2}. From here on, for sake of simplicity, let $\langle \xi_2^j \rangle_{l_1} \equiv \langle \xi_2^j \rangle (\xi_{1,l_1})$ denote the conditional moments. By substituting Eq. 4.9 into Eq. 4.8, the pure moments can be expressed as

$$m_{i,j}^{i+j} = \sum_{l_1=1}^{\mathrm{M}_1} w_{l_1} \xi_{1,l_1}^i \langle \xi_2^j \rangle_{l_1}. \tag{4.10}$$

A Vandermonde linear system [88] is generated by Eq. 4.10, which relates the conditional moments to the pure moments:

$$\boldsymbol{\Xi}_1 \mathbf{W}_1 \begin{pmatrix} \langle \xi_2 \rangle_1 & \langle \xi_2^2 \rangle_1 & \cdots & \langle \xi_2^{2\mathrm{M}_2-1} \rangle_1 \\ \langle \xi_2 \rangle_2 & \langle \xi_2^2 \rangle_2 & \cdots & \langle \xi_2^{2\mathrm{M}_2-1} \rangle_2 \\ \vdots & \vdots & \vdots & \vdots \\ \langle \xi_2 \rangle_{\mathrm{M}_1} & \langle \xi_2^2 \rangle_{\mathrm{M}_1} & \cdots & \langle \xi_2^{2\mathrm{M}_2-1} \rangle_{\mathrm{M}_1} \end{pmatrix} = \begin{pmatrix} m_{0,1}^1 & m_{0,2}^2 & \cdots & m_{0,2\mathrm{M}_2-1}^{2\mathrm{M}_2-1} \\ m_{1,1}^1 & m_{1,2}^3 & \cdots & m_{1,2\mathrm{M}_2-1}^{2\mathrm{M}_2} \\ \vdots & \vdots & & \vdots \\ m_{\mathrm{M}_1-1,1}^{\mathrm{M}_1} & m_{\mathrm{M}_1-1,2}^{\mathrm{M}_1+1} & \cdots & m_{\mathrm{M}_1-1,2\mathrm{M}_2-1}^{\mathrm{M}_2+2\mathrm{M}_2-1} \end{pmatrix}, \tag{4.11}$$

where the coefficient matrices are

$$\mathbf{\Xi_1} = \begin{pmatrix} 1 & \cdots & 1 \\ \xi_{1,1} & \cdots & \xi_{1,\mathrm{M}_1} \\ \vdots & & \vdots \\ (\xi_{1,1})^{\mathrm{M}_1-1} & \cdots & (\xi_{1,\mathrm{M}_1})^{\mathrm{M}_1-1} \end{pmatrix}, \text{ and } \mathbf{W}_1 = \begin{pmatrix} 1 & & \\ & \ddots & \\ & & w_{\mathrm{M}_1} \end{pmatrix}. \tag{4.12}$$

This linear system can be solved using the procedure proposed by Rybicki [88] to obtain the conditional moments, which can be inverted to compute the conditional quadrature weights w_{l_1,l_2} and nodes ξ_{2,l_1,l_2} for each value of l_1 by means of the adaptive Wheeler algorithm [120]. With the conditional quadrature weights and nodes, a quadrature representation of the joint PDF $p(\xi_1, \xi_2)$ can be constructed:

$$p(\xi_1, \xi_2) = \sum_{l_1=1}^{\mathrm{M}_1} \sum_{l_2=1}^{\mathrm{M}_2} w_{l_1} w_{l_1,l_2} \delta(\xi_1 - \xi_{1,l_1}) \delta(\xi_2 - \xi_{2,l_1,l_2}). \tag{4.13}$$

The n-th order moment of the system response in Eq. 4.1 can then be computed as:

$$m_n = \int_\Omega \kappa(\boldsymbol{\xi})^n p(\boldsymbol{\xi}) \mathrm{d}\boldsymbol{\xi} \approx \sum_{l_1=1}^{\mathrm{M}_1} \sum_{l_2=1}^{\mathrm{M}_2} w_{l_1} w_{l_1,l_2} (\kappa(\xi_{1,l_1}, \xi_{2,l_1,l_2}))^n. \tag{4.14}$$

Once the moments of the system response are obtained, conventional statistics of the response such as mean, variance, skewness, and kurtosis, can be evaluated.

It is worth noting that the adaptive Wheeler algorithm [120] is applied to automatically determine the actual number of quadrature points M_1 and M_2 used in each direction of the parameter space. The algorithm uses two parameters (*eabs* and *rmin*) to control the distance between any two nodes and the ratio of the smallest to the largest weights respectively. The *eabs* ensures any two nodes are further than a user-defined limit so that the Vandermonde matrix shown in Eq. 4.11 is well defined. The *rmin* controls the minimum values of the weight ratios in order to avoid highly skewed nodes. In CQMOM, the user has to provide only the maximum value of quadrature nodes to be used in each direction, as an upper bound for the quadrature algorithm, which will determine the optimal number of nodes automatically, in order to properly represent the PDF.

4.3 Reconstruction of the Probability Distribution Function of the System Response

The moments of the system response obtained with the method described in Section 4.2 can be used to reconstruct the approximated PDF of the response using the extended quadrature method of moments (EQMOM) [121]. The founding idea of the method is to represent the PDF $p(\kappa)$ as a weighted sum of N non-negative kernel density functions [14, 121]:

$$f_N(\kappa) = \sum_{i=1}^{N} \rho_i \delta_\sigma(\kappa, \kappa_i), \tag{4.15}$$

where ρ_i denotes the quadrature weights used in EQMOM, in order to be distinguished from the quadrature weights w_i used in the sampling procedure, κ_i are the quadrature nodes used in EQMOM, and $\delta_\sigma(\kappa, \kappa_i)$ is a kernel density function related to the parameter σ.

The kernel density function $\delta_\sigma(\kappa, \kappa_i)$ is selected based on the properties of the distribution that needs to be reconstructed, especially based on the support of the distribution to be reconstructed. For κ in the bounded interval $[a, b]$, a beta distribution can be chosen for δ_σ; for κ on the semi-infinite interval $[a, +\infty[$, δ_σ is set to a gamma distribution; for $\kappa \in \mathbb{R}$, a normal distribution is used to define δ_σ. Then $2N + 1$ moments of the system response are used to solve for $2N + 1$ unknowns, including the spread parameter σ, N quadrature weights ρ_i, and N quadrature nodes κ_i with $i = 1, \ldots, N$. It is worth recalling that the parameter σ is shared by all the kernel density functions, in order to simplify the solution procedure that allows its value to be determined. The remainder of this section gives a general idea of solving for these unknowns, while procedures using different kernel densities can be found in Appendix C and in the literature [14, 121].

The first step of the EQMOM procedure consists of calculating the n-th order integer moments of the kernel density $\delta_\sigma(\kappa, \kappa_i)$, and the integer moments of p. Then the integer moments of p can be rewritten in the matrix form, which is a lower triangular system of linear equations to find σ, shown in Eq. 4.16,

$$\mathbf{m} = \mathbf{A}(\sigma)\mathbf{m}^* \tag{4.16}$$

where $m_n^* = \sum_{i=1}^{N} \rho_i \kappa_i^n$, and $\mathbf{A}(\sigma)$ is a lower triangular matrix. The parameter σ is then determined by solving the system in Eq. 4.16 iteratively with the following algorithm [121]:

1. Guess the value of σ
2. Compute the moments m_n^* from the lower triangular system

$$\mathbf{m} = \mathbf{A}(\sigma)\mathbf{m}^*$$

3. Use the adaptive Wheeler algorithm to find weights ρ_i and abscissae κ_i from $\mathbf{m}^*$
4. Compute m_{2N}^* using weights and abscissae found in the last step
5. Compute the scalar function $J_N(\sigma)$, which is the difference between the original moments and the approximated moments computed from m_{2N}^*
6. If $J_N(\sigma) \neq 0$, guess a new σ and iterate from step 1.

The final approximate PDFs using different kernel density functions are shown in Eq. 4.17,

$$f_N(\kappa) = \begin{cases} \dfrac{1}{b-a} \displaystyle\sum_{i=1}^{N} \rho_i \dfrac{\left(\frac{\kappa-a}{b-a}\right)^{\lambda_i - 1} \left(\frac{b-\kappa}{b-a}\right)^{\phi_i - 1}}{B\left(\lambda_i, \phi_i\right)} & \kappa \in [a, b] \\ \displaystyle\sum_{i=1}^{N} \rho_i \dfrac{(\kappa - a)^{\lambda_i - 1} \, \mathrm{e}^{-(\kappa - a)/\sigma}}{\Gamma(\lambda_i) \sigma^{\lambda_i}} & \kappa \in [a, +\infty[\\ \displaystyle\sum_{i=1}^{N} \dfrac{\rho_i}{\sigma\sqrt{2\pi}} \exp\left[-\dfrac{(\kappa - \kappa_i)^2}{2\sigma^2}\right] & \kappa \in \mathbb{R} \end{cases} \tag{4.17}$$

where the parameters λ_i and ϕ_i are related to κ_i and σ, whose definitions are given in Appendix C.

4.4 Applications

The proposed approach was applied to the simulation of a bubbling fluidized bed, which was chosen as an example application. The study is based on case 1 of the 2013 NETL small scale challenge problem (SSCP-I) [75]. The effects of two independent uncertain parameters, namely the particle-wall and the particle-particle restitution coefficients, on the system response are studied. Low-order statistics of the system response are reported, and the PDF of the response

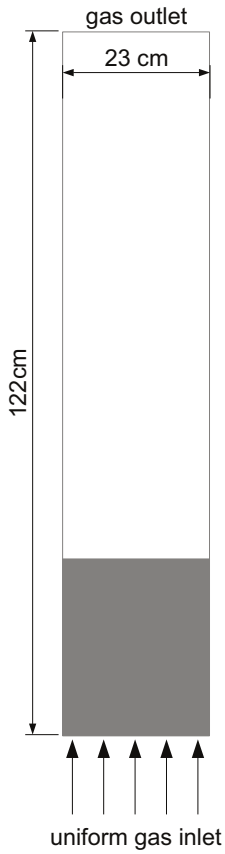

Figure 4.1 Schematic representation of the bubbling fluidized bed.

is reconstructed at specific locations in the computational domain. The simulation results are also compared to experimental data provided by SSCP-I.

4.4.1 Description of the simulation conditions

The experimental data of SSCP-I were obtained in a 3 in $\times$ 9 in $\times$ 48 in bubbling fluidized bed with rectangular cross-section. Geldart D particles with constant diameter and high sphericity were used in the experiments. In this work we perform two-dimensional simulations of the experimental system, which we model as a rectangle having width of 23 cm and height of 122 cm, as illustrated in Figure 4.1. The gas is injected uniformly at the bottom of the reactor with superficial velocity 219 cm/s. The top of the reactor is at atmospheric conditions. The particles have a Sauter mean diameter of 0.3256 cm and a density of 1.131 g/cm^3. The initial bed height is 16.3 cm, with packed bed void fraction equal to 0.4. A uniform grid with

46×244 cells is used for all simulations in this work. The open source code MFIX (Multiphase Flow with Interface eXchanges) [99] developed by NETL, is used to simulate the system. The remaining simulation conditions are listed in Table 4.1.

Table 4.1 MFIX simulation conditions.

Conditions	Value
Particle-wall restitution coefficient (e_{pw})	$[0.75, 0.95]$
Particle-particle restitution coefficient (e_{pp})	$[0.73, 0.92]$
Specularity coefficient	0.045
Inlet boundary condition	Constant gas velocity
Outlet boundary condition	Zero relative gas pressure
Wall boundary condition for gas phase	No-slip
Wall boundary condition for solid phase	Johnson-Jackson [49]
Simulation time	90 s
Initial time step	1.0×10^{-4} s
Convergence criteria	1.0×10^{-4}

4.4.2 Governing equations

A two-fluid model [21] with kinetic theory closures for solid phase [40] was applied to describe the fluidized bed considered in the example application. The governing equations implemented into MFIX are briefly summarized below [99].

Continuity equations of gas phase (g) and solid phase (s)

$$\frac{\partial}{\partial t}\left(\alpha_{\mathrm{g}}\rho_{\mathrm{g}}\right) + \nabla \cdot \left(\alpha_{\mathrm{g}}\rho_{\mathrm{g}}\mathbf{U}_{\mathrm{g}}\right) = 0 \tag{4.18}$$

$$\frac{\partial}{\partial t}\left(\alpha_{\mathrm{s}}\rho_{\mathrm{s}}\right) + \nabla \cdot \left(\alpha_{\mathrm{s}}\rho_{\mathrm{s}}\mathbf{U}_{\mathrm{s}}\right) = 0 \tag{4.19}$$

where α_{i} is the phase volume fraction, ρ_{i} is the density, and $\mathbf{U}_{\mathrm{i}}$ is the phase velocity field.

Momentum equations of gas and solid phases

$$\frac{\partial}{\partial t}\left(\alpha_{\mathrm{g}}\rho_{\mathrm{g}}\mathbf{U}_{\mathrm{g}}\right)+\nabla\cdot\left(\alpha_{\mathrm{g}}\rho_{\mathrm{g}}\mathbf{U}_{\mathrm{g}}\mathbf{U}_{\mathrm{g}}\right)=-\alpha_{\mathrm{g}}\nabla p_{\mathrm{g}}+\nabla\cdot\boldsymbol{\tau}_{\mathrm{g}} + \alpha_{\mathrm{g}}\rho_{\mathrm{g}}\mathbf{g}+K_{\mathrm{gs}}\left(\mathbf{U}_{\mathrm{s}}-\mathbf{U}_{\mathrm{g}}\right) \quad (4.20)$$

$$\frac{\partial}{\partial t}\left(\alpha_{\mathrm{s}}\rho_{\mathrm{s}}\mathbf{U}_{\mathrm{s}}\right)+\nabla\cdot\left(\alpha_{\mathrm{s}}\rho_{\mathrm{s}}\mathbf{U}_{\mathrm{s}}\mathbf{U}_{\mathrm{s}}\right)=-\alpha_{\mathrm{s}}\nabla p_{\mathrm{g}}-\nabla p_{\mathrm{s}}+\nabla\cdot\boldsymbol{\tau}_{\mathrm{s}} + \alpha_{\mathrm{s}}\rho_{\mathrm{s}}\mathbf{g}-K_{\mathrm{gs}}\left(\mathbf{U}_{\mathrm{s}}-\mathbf{U}_{\mathrm{g}}\right) \quad (4.21)$$

where p_{i} is the phase pressure, $\boldsymbol{\tau}_{\mathrm{i}}$ is the phase stress tensor, $\mathbf{g}$ is the acceleration of gravity, and K_{gs} is the gas-solid drag coefficient.

Syamlal and O'Brien gas-solid drag coefficient

$$K_{gs}=\frac{3}{4}C_D\frac{\rho_{\mathrm{g}}\alpha_{\mathrm{g}}\alpha_{\mathrm{s}}}{U_{\mathrm{rs}}^2 d_{\mathrm{s}}}\left(\frac{\mathrm{Re}}{U_{\mathrm{rs}}}\right)\left|\mathbf{U}_{\mathrm{s}}-\mathbf{U}_{\mathrm{g}}\right|$$

$$C_D=\begin{cases}\dfrac{24}{\mathrm{Re}}\left(1+0.15\,\mathrm{Re}\right)^{0.687} & \mathrm{Re}<1000\\ 0.44 & \mathrm{Re}\geq 1000\end{cases}$$

$$U_{\mathrm{rs}}=0.5\left(A-0.06\,\mathrm{Re}+\sqrt{(0.06\,\mathrm{Re})^2+0.12\,\mathrm{Re}(2B-A)+A^2}\right)$$

$$A=\alpha_{\mathrm{g}}^{4.14}$$

$$B=\begin{cases}0.8\alpha_{\mathrm{g}}^{1.28} & \alpha_{\mathrm{g}}\leq 0.85\\ \alpha_{\mathrm{g}}^{2.65} & \alpha_{\mathrm{g}}>0.85\end{cases}$$

$$\mathrm{Re}=\frac{\rho_{\mathrm{g}}\alpha_{\mathrm{g}}\left|\mathbf{U}_{\mathrm{s}}-\mathbf{U}_{\mathrm{g}}\right|d_{\mathrm{s}}}{\mu_{\mathrm{g}}}$$

where d_{s} is the particle diameter, and μ_{g} is the shear viscosity of gas.

Constitutive equations

The constitutive equations required to close the momentum equations are listed Table 4.2.

Table 4.2 Constitutive equations. The symbols represent $\mathbf{I}$: unit tensor, e_{pp}: particle-particle restitution coefficient, Θ_{s}: granular temperature, ϕ: angle of internal friction, I_{2D}: the second invariant of the deviator of the strain-rate tensor, and $\alpha_{\mathrm{s,max}}$: packing limit.

Gas-phase stress tensor
$\boldsymbol{\tau}_{\mathrm{g}} = \alpha_{\mathrm{g}}\mu_{\mathrm{g}}\left[\nabla\mathbf{U}_{\mathrm{g}} + (\nabla\mathbf{U}_{\mathrm{g}})^{\mathrm{T}}\right] - \frac{2}{3}\alpha_{\mathrm{g}}\mu_{\mathrm{g}}\left(\nabla\cdot\mathbf{U}_{\mathrm{g}}\right)\mathbf{I}$
Solid-phase stress tensor
$\boldsymbol{\tau}_{\mathrm{s}} = \alpha_{\mathrm{s}}\mu_{\mathrm{s}}\left[\nabla\mathbf{U}_{\mathrm{s}} + (\nabla\mathbf{U}_{\mathrm{s}})^{\mathrm{T}}\right] + \alpha_{\mathrm{s}}\left(\lambda_{\mathrm{s}} - \frac{2}{3}\mu_{\mathrm{s}}\right)\left(\nabla\cdot\mathbf{U}_{\mathrm{s}}\right)\mathbf{I}$
Granular temperature equation
$\frac{3}{2}\left[\frac{\partial}{\partial t}\left(\alpha_{\mathrm{s}}\rho_{\mathrm{s}}\Theta_{\mathrm{s}}\right) + \nabla\cdot\left(\alpha_{\mathrm{s}}\rho_{\mathrm{s}}\mathbf{U}_{\mathrm{s}}\Theta_{\mathrm{s}}\right)\right] = \left(-p_{\mathrm{s}}\mathbf{I} + \boldsymbol{\tau}_{\mathrm{s}}\right) : \nabla\mathbf{U}_{\mathrm{s}} + \nabla\cdot\left(k_{\mathrm{s}}\nabla\Theta_{\mathrm{s}}\right) - \gamma_{\mathrm{s}} - 3K_{\mathrm{gs}}\Theta_{\mathrm{s}}$
Solids pressure
$p_{\mathrm{s}} = \alpha_{\mathrm{s}}\rho_{\mathrm{s}}\Theta_{\mathrm{s}} + 2(1+e_{\mathrm{pp}})\alpha_{\mathrm{s}}^2\rho_{\mathrm{s}}g_0\Theta_{\mathrm{s}}$
Solids bulk viscosity
$\lambda_{\mathrm{s}} = \frac{4}{3}\alpha_{\mathrm{s}}\rho_{\mathrm{s}}d_{\mathrm{s}}g_0(1+e_{\mathrm{pp}})\sqrt{\frac{\Theta_{\mathrm{s}}}{\pi}}$
Solids shear viscosity
$\mu_{\mathrm{s}} = \mu_{\mathrm{s,kin}} + \mu_{\mathrm{s,fr}}$
Solids kinetic viscosity
$\mu_{\mathrm{s,kin}} = \frac{10\rho_{\mathrm{s}}d_{\mathrm{s}}\sqrt{\pi\Theta_{\mathrm{s}}}}{96\alpha_{\mathrm{s}}g_0(1+e_{\mathrm{pp}})}\left[1 + \frac{4}{5}\alpha_{\mathrm{s}}g_0(1+e_{\mathrm{pp}})\right]^2$
Solids frictional viscosity
$\mu_{\mathrm{s,fr}} = \frac{p_{\mathrm{s}}\sin\phi}{2\sqrt{I_{2D}}}$
Radial distribution function
$g_0 = \left[1 - \left(\frac{\alpha_{\mathrm{s}}}{\alpha_{\mathrm{s,max}}}\right)^{\frac{1}{3}}\right]^{-1}$
Solids conductivity
$k_{\mathrm{s}} = \frac{150\rho_{\mathrm{s}}d_{\mathrm{s}}\sqrt{\pi\Theta_{\mathrm{s}}}}{384g_0(1+e_{\mathrm{pp}})}\left[1 + \frac{6}{5}\alpha_{\mathrm{s}}g_0(1+e)\right]^2 + 2\alpha_{\mathrm{s}}^2\rho_s d_s g_0(1+e)\sqrt{\frac{\Theta_{\mathrm{s}}}{\pi}}$
Collisional dissipation
$\gamma_{\mathrm{s}} = \frac{12\alpha_{\mathrm{s}}^2\rho_{\mathrm{s}}g_0(1-e_{\mathrm{pp}}^2)}{d_{\mathrm{s}}\sqrt{\pi}}\Theta_{\mathrm{s}}^{3/2}$

Johnson-Jackson boundary condition

At the walls, no slip boundary condition is applied for the gas phase. For solid phase, Johnson-Jackson boundary condition is used [49], shown in Eq. 4.22,

$$\begin{aligned}\mathbf{n}\cdot(\mu_{\mathrm{s}}\nabla\mathbf{U}_{\mathrm{sl}}) &= -\frac{\pi\phi_{\mathrm{s}}\alpha_{\mathrm{s}}\rho_{\mathrm{s}}g_0\sqrt{3\Theta_{\mathrm{s}}}}{6\alpha_{\mathrm{s,max}}}\mathbf{U}_{\mathrm{sl}} \\ \mathbf{n}\cdot(k_{\mathrm{s}}\nabla\Theta_{\mathrm{s}}) &= \frac{\pi\alpha_{\mathrm{s}}\rho_{\mathrm{s}}g_0|\mathbf{U}_{\mathrm{sl}}|^2\sqrt{3\Theta_{\mathrm{s}}}}{6\alpha_{\mathrm{s,max}}} - \frac{\sqrt{3}\pi\alpha_{\mathrm{s}}\rho_{\mathrm{s}}g_0(1-e_{\mathrm{pw}})^2}{4\alpha_{\mathrm{s,max}}}\Theta_{\mathrm{s}}^{3/2},\end{aligned} \tag{4.22}$$

where $\mathbf{n}$ is the unit vector normal to the wall, $\mathbf{U}_{\mathrm{sl}}$ is the slip velocity between the particles and the wall, ϕ_{s} is the specularity coefficient, and e_{pw} is the particle-wall restitution coefficient.

4.4.3 Sampling procedure

As mentioned above, two independent parameters were considered as uncertain variables: particle-wall restitution coefficient e_{pw} and particle-particle restitution coefficient e_{pp}. The space of the uncertain parameters was sampled using the CQMOM approach described in Section 4.2.2. The pure moments that CQMOM requires as input are estimated based on the experimental data provided by SSCP-I for these two parameters. A series of experiments were conducted to measure e_{pw} and e_{pp} for the particle and wall materials used in the actual bubbling fluidized bed. The range of e_{pw} is 0.75 to 0.95, and e_{pp} is between 0.73 to 0.92. The space of e_{pw} was sampled first with five quadrature nodes, then the conditional moments with respect to e_{pp} were determined, with which the conditional weights and nodes were computed. In total, fifteen samples are generated by CQMOM. Figure 4.2(a) gives the locations of each sample, and Figure 4.2(b) shows the weights of each sample. The nodes with large weights concentrate in the region near the mean values of the parameters.

4.4.4 Results and discussion

Once the space of the uncertain parameters was sampled, MFIX simulations were performed for each sample. Four time-averaged quantities are considered as system response: solid volume fraction (α_{s}), gas pressure (p_{g}), solid-phase horizontal velocity (u_{s}), and solid-phase vertical velocity (v_{s}). Low-order statistics, such as mean and variance of the system response, are computed and compared to experimental data. The approximated PDF of the response at

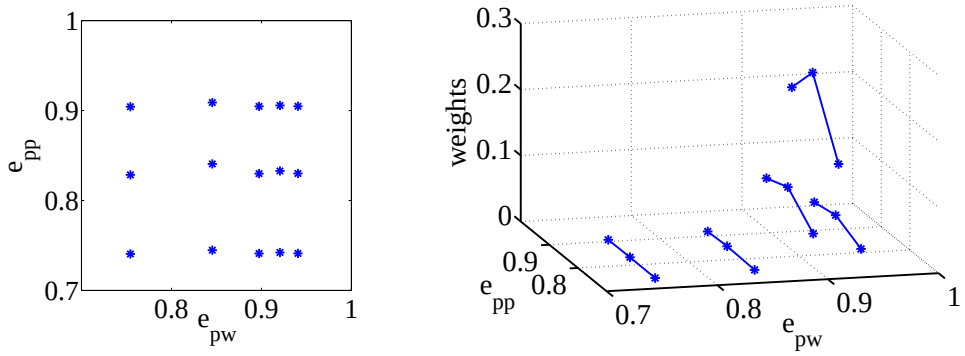

(a) (b)

Figure 4.2 Samples generated by CQMOM: (a) locations and (b) weights of each sample.

specific locations in the computational domain is reconstructed. Results are discussed in the remainder of this section.

4.4.4.1 Low-order statistics

Figure 4.3 shows the contour plots of mean and standard deviation of the solid volume fraction, indicating a symmetric profile with respect to the vertical axis. The concentration of particles decreases with increasing distance from the bottom of the reactor, in the center of the bed, and particles concentrate near the walls. The effect of uncertain particle-particle and particle-wall restitution coefficients on the solid volume fraction mainly focuses on the interface of the bed, especially on the locations near the wall, and also at the center of the fluidized bed. The minimum and maximum values of the standard deviation of α_s are 4.393×10^{-6} and 3.614×10^{-2}, respectively.

The designated location 1 to 4 in Figure 4.3 are where the PDF of the system response is reconstructed. Locations 1 and 2 are in the fluidized bed, where the experimental data are obtained. Locations 3 and 4 are near the interface of the bed. If not stated otherwise, the designated locations in all figures of this section are the same. The coordinates of these four points are listed in Table 4.3.

Figure 4.4 reports the contour plots of mean and standard deviation of the gas pressure. The gas pressure reduces to zero with increasing the distance from the bottom of the reactor. The

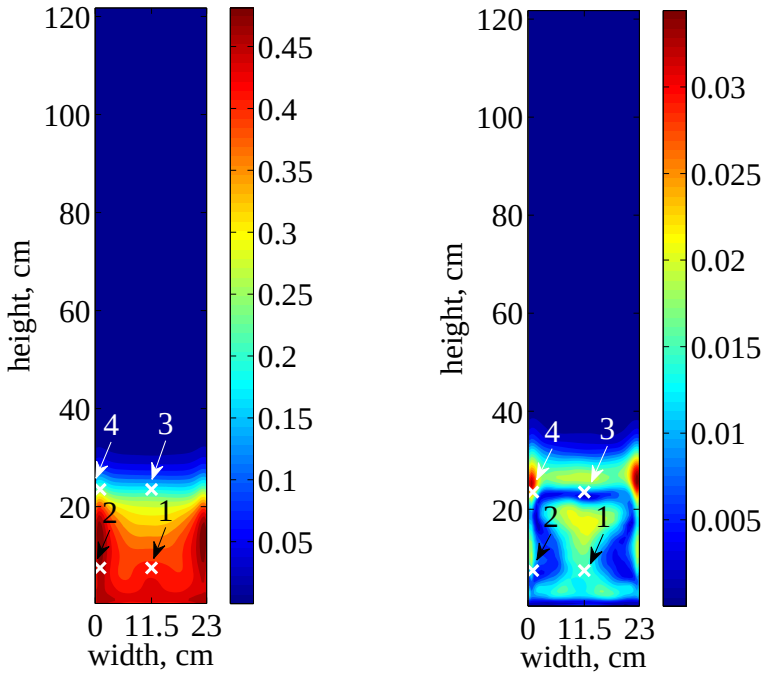

(a) mean (b) standard deviation

Figure 4.3 Contour plots of (a) mean and (b) standard deviation of solid volume fraction.

Table 4.3 Coordinates of the designated locations.

Location	Coordinates	
	x	y
1	11.50	7.50
2	1.00	7.50
3	11.50	23.50
4	1.00	23.50

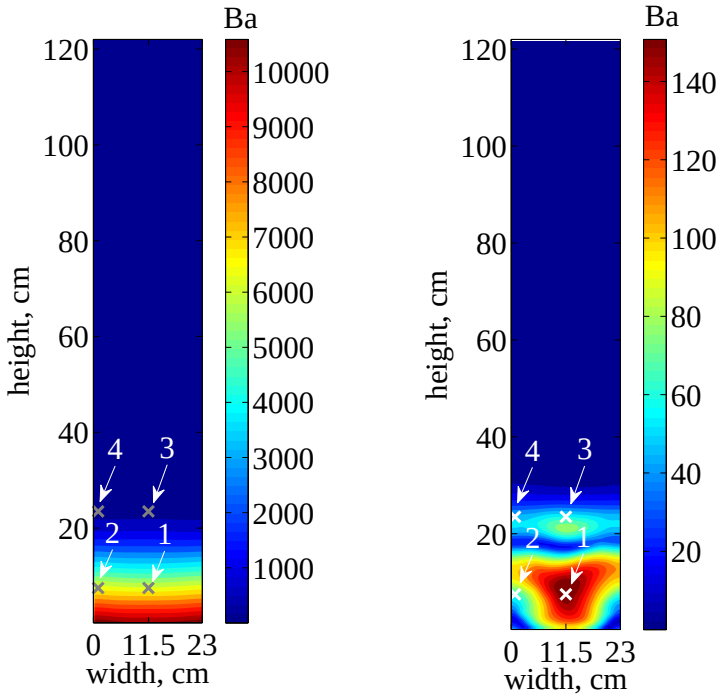

(a) mean (b) standard deviation

Figure 4.4 Contour plots of (a) mean and (b) standard deviation of gas pressure.

uncertain parameters influence the gas pressure the most in the center of the bed. The minimum and maximum values of the standard deviation of p_g are 5.514×10^{-3} Ba and 1.583×10^{2} Ba, respectively.

Figure 4.5 and Figure 4.6 show the contour plots of the mean and standard deviation of the solid horizontal and vertical velocity. Figure 4.5(a) and Figure 4.6(a) indicate circulations of particles are formed. The effect of uncertain parameters focuses on the locations near the interface of the bed and at the bottom of the bed for solid horizontal velocity, and on locations near the wall for solid vertical velocity. The minimum and maximum value of the standard deviation of u_s are 0.0 cm/s and 4.947 cm/s, respectively, while those values of v_s are 0.0 cm/s and 7.365 cm/s, respectively.

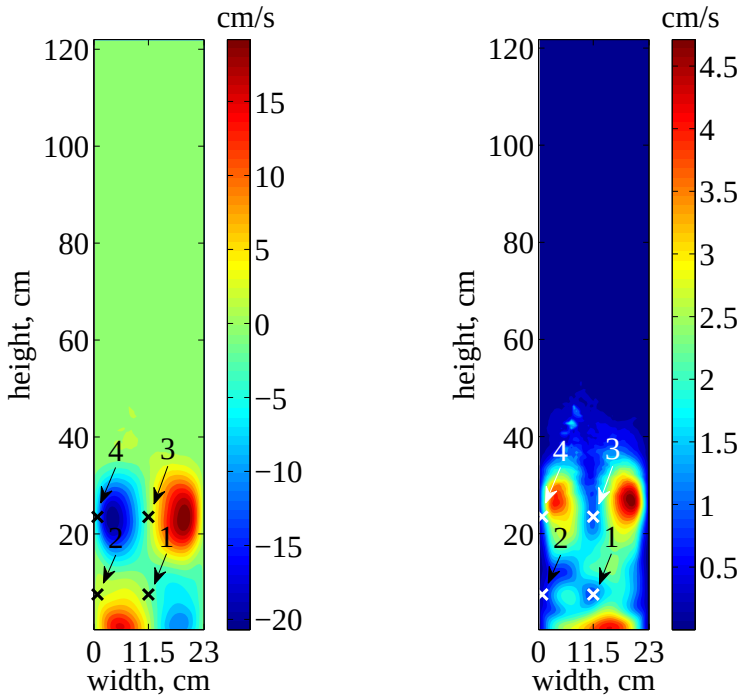

(a) mean

(b) standard deviation

Figure 4.5 Contour plots of (a) mean and (b) standard deviation of solid horizontal velocity.

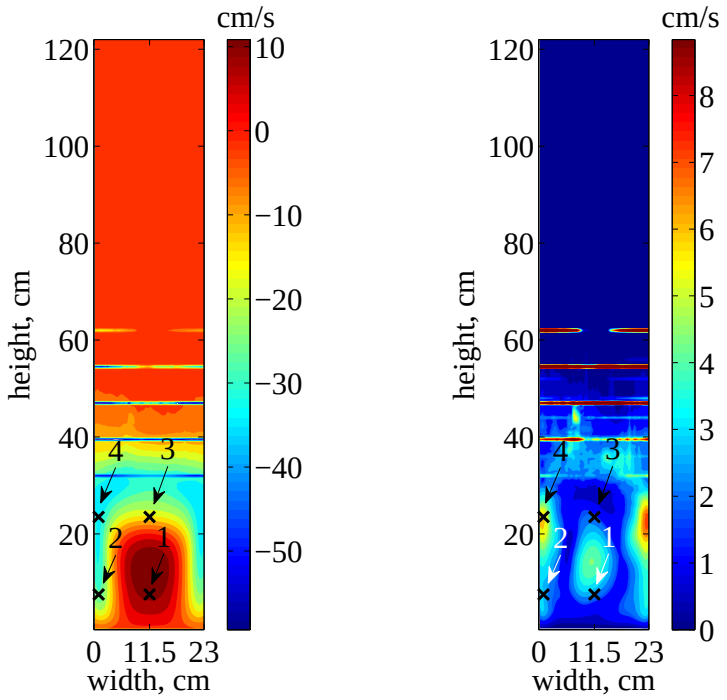

(a) mean

(b) standard deviation

Figure 4.6 Contour plots of (a) mean and (b) standard deviation of solid vertical velocity.

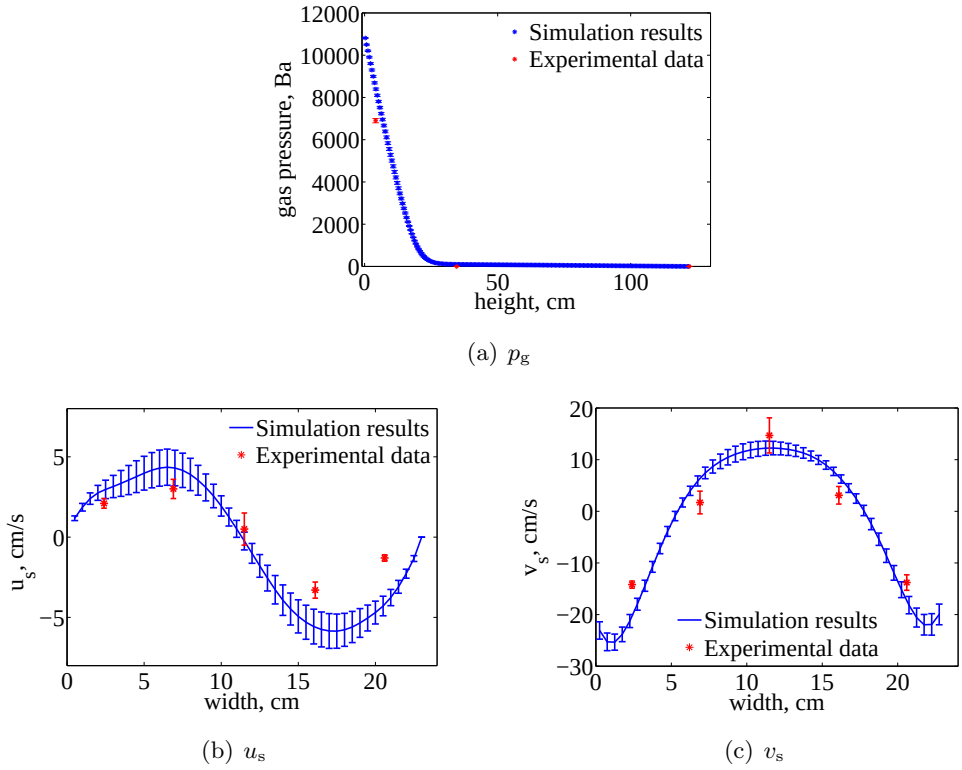

(a) p_g

(b) u_s

(c) v_s

Figure 4.7 Simulated (a) gas pressure, (b) solid horizontal velocity, (c) and solid vertical velocity compared to experimental data.

4.4.4.2 Comparison with experimental data

Based on the results for the mean and standard deviation of the system response, the 95% confidence interval of the simulation outputs can be calculated as

$$\bar{\kappa} \pm t_{0.025}(N-1)\frac{S}{\sqrt{N}}, \tag{4.23}$$

where $\bar{\kappa}$ and S are the mean and the standard deviation of the system response, N is the number of samples, and $t_{0.025}(N-1)$ is the value at which the probability of t-distribution with $N-1$ degrees of freedom is 0.025. In this work, N is 15, and $t_{0.025}(14)$ is 2.145. Therefore, the simulation results can be compared to experimental data provided by SSCP-I [75], shown in Figure 4.7.

Results show that the mean values of the simulation results are in fair agreement with experimental data. Some of the experimental data give larger 95% confidence intervals, especially near the center of the bed, which may indicate that, besides particle-particle and particle-

wall restitution coefficients, other uncertain parameters, such as particle size, may influence the simulation results. It is also possible that the uncertainty in the experiments due to the measurement method causes large confidence intervals for experimental data.

4.4.4.3 Reconstruction of the PDF of the system response

Four locations are chosen to reconstruct the PDF of solid volume fraction, gas pressure, and solid horizontal and vertical velocities using EQMOM described in Section 4.3 [121]. Results are discussed below.

The PDF of the solid volume fraction is reconstructed using two-node beta EQMOM because the support of the distribution of the solid volume fraction is $[0, 1]$. Reconstruction results for locations 1 to 4 are shown in Figure 4.8. All the reconstructed distributions show two peaks. However, those at locations 1, 2, and 3 are very narrow, while the one at location 4 is wider, indicating an actual bimodal distribution. At locations 1 and 2 inside the fluidized bed, the solid volume fraction is high, while near the bed free surface (locations 3 and 4), the peaks corresponds to low solid volume fraction. For locations near the wall (locations 2 and 4), a higher solid volume fraction is preferred.

Figure 4.9 shows the reconstruction results for locations 1 to 4 for the gas pressure, obtained with gamma EQMOM. All distributions present profiles with a bimodal distribution. At locations 1 and 2 inside the bed, low gas pressure has high probability. The PDF at location 2 is narrower than the PDF of location 1, which is consistent with the conclusion obtained from the contour plot of the standard deviation of the gas pressure shown in Figure 4.4(b) that at locations in the center of the bed, the standard deviation of gas pressure is large.

The PDF of the solid horizontal velocity is reconstructed using two-node Gaussian EQMOM since the distribution of velocity is defined on the whole real line. Figure 4.10 shows the reconstruction results for locations 1 to 4. For locations 1 and 3 at the center of the bed, the peak of the distribution forms near zero velocity with a positive tail for location 1 (inside the bed) and a negative tail for location 3 (near interface of the bed). For locations 2 and 4 near the wall, a bimodal distribution is observed.

The PDF of the solid vertical velocity is reconstructed using Gaussian EQMOM. As shown

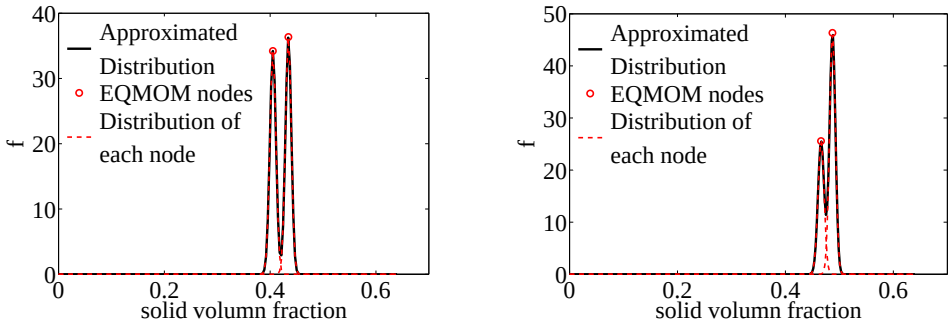

(a) location 1

(b) location 2

(c) location 3

(d) location 4

Figure 4.8 Reconstructed distribution of the solid volume fraction at different locations.

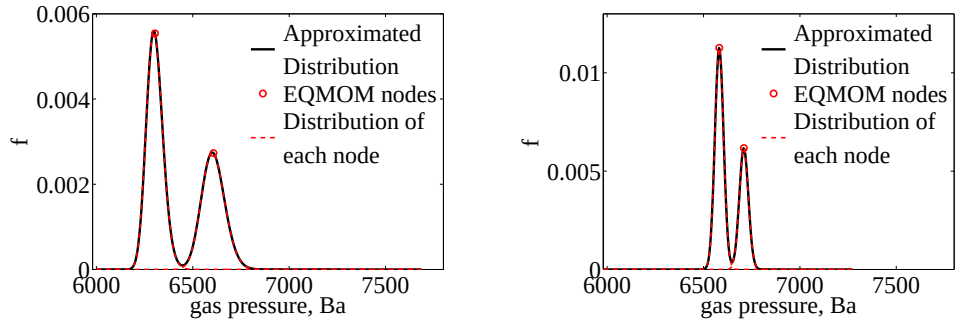

(a) location 1

(b) location 2

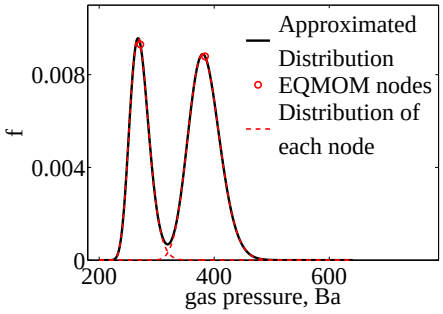

(c) location 3

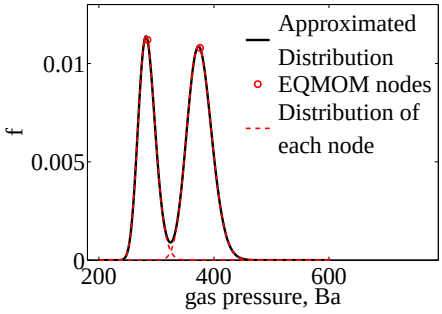

(d) location 4

Figure 4.9 Reconstructed distribution of the gas pressure at different locations.

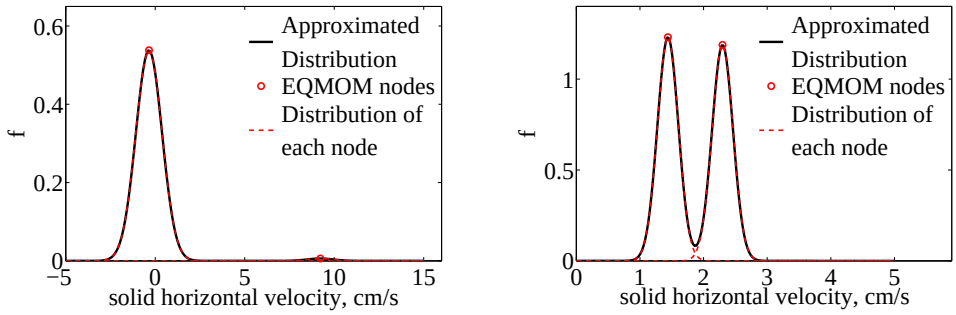

(a) location 1

(b) location 2

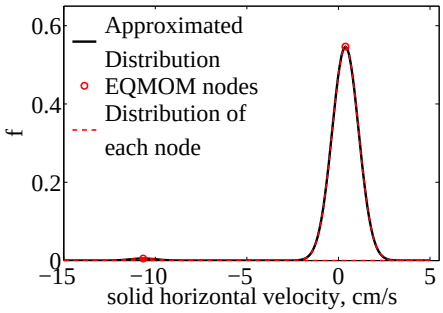

(c) location 3

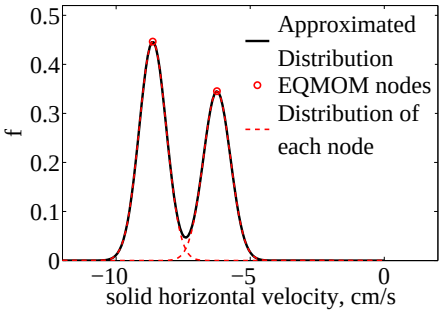

(d) location 4

Figure 4.10 Reconstructed distribution of the solid horizontal velocity at different locations.

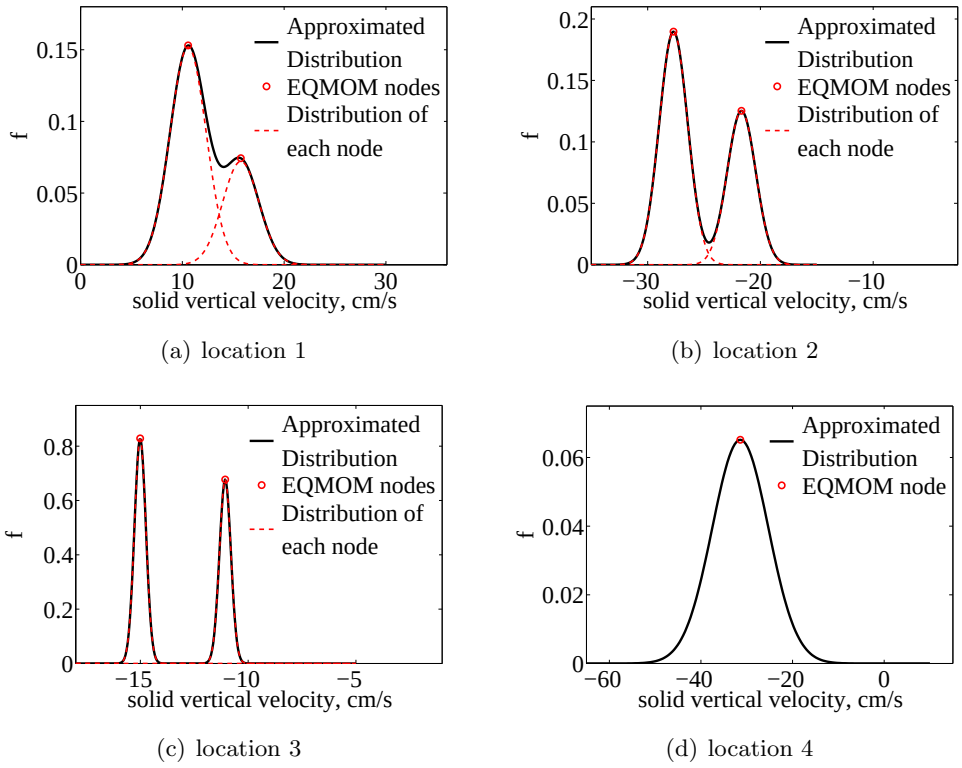

(a) location 1

(b) location 2

(c) location 3

(d) location 4

Figure 4.11 Reconstructed distribution of the solid vertical velocity at different locations.

in Figure 4.11, for locations 1 to 3, two-node Gaussian EQMOM is used while for location 4, only a node reconstruction was performed because the PDF is Gaussian, and one node is sufficient to reconstruct it accurately. At location 1, a broad peak with a shoulder is formed. Particles are going upward, and low velocity has high probability at this location. At location 2 when particles are moving downward, a bimodal distribution is observed with high probability for high velocity. At locations 3 and 4 near the bed free surface, particles are moving downward.

4.5 Source Code

The python source code implementing the quadrature-based UQ procedure described in this manuscript is released under the GNU General Public License Version 3 and can be downloaded from the git repository https://bitbucket.org/albertop/qbuq .

4.6 Conclusions

Non-intrusive quadrature-based uncertainty quantification and a reconstruction procedure for the PDF of the system response are presented in this work. The methods are applied to the case of a bubbling fluidized bed as an example. Contour plots of the mean and standard deviation of solid volume fraction, gas pressure, and solid horizontal and vertical velocities are shown. The mean value and 95% confidence interval of the system response at specific locations are compared to the values obtained from experimental data. The mean values of the simulation results are in fair agreement with experiment. The confidence intervals obtained from the simulation results sometimes cannot cover the confidence intervals provided by the experiment, which may be caused by uncertainty introduced by other parameters besides the two parameters studied in this work. The measurement method may also result in large confidence intervals for experimental data. This observation needs to be studied in future work. The PDF of the system response is reconstructed at four different locations in the computational domain. The reconstruction procedure will be extended to multi-variate problems in future work.

CHAPTER 5. A QUADRATURE-BASED UNCERTAINTY QUANTIFICATION APPROACH IN A MULTIPHASE GAS-PARTICLE FLOW SIMULATION IN A RISER

A non-intrusive quadrature based uncertainty quantification (QBUQ) approach is applied to a riser of a circulating fluidized bed with particle size assumed to be the uncertain parameter. The method uses Gaussian quadrature formulae to sample the space of the distribution of the uncertain particle size. Numerical simulations are performed for each sample, whose results are used to directly estimate the moments of the quantities of interest with quadrature rules. The solid volume fraction, solid phase velocities, and granular temperature are considered as quantities of interest. The set of moments is then used to calculate low order statistics such as mean and standard deviation, and to reconstruct the probability distribution function (PDF) of the system response with extended quadrature method of moments (EQMOM) for univariate PDF reconstruction and extended conditional quadrature method of moments (ECQMOM) for bivariate PDF reconstruction. Contour plots of the mean and standard deviation of quantities of interest and reconstructed PDFs of the system response at specific locations of the computational domain are provided. The simulation results are compared to the experimental data provided in the literature as well.

5.1 Introduction

Circulating fluidized beds (CFB) are widely used in industrial operations such as fluid catalytic cracking (FCC), combustion, calcination, and Fischer-Tropsch synthesis [5,7,8,12,22, 43,83,93]. In a typical CFB, the riser is the unit where gas and particles interact and chemical reactions occur, and hence where many studies are concentrating. By using computational

fluid dynamics (CFD), the hydrodynamics of fluidization inside a riser can be studied, and simulation results are adopted for design, scale-up, and optimization of CFB reactors. To simulate gas-particle flows in risers, two types of approaches are in general considered: Eulerian-Lagrangian approach and Eulerian-Eulerian approach [41, 81, 82, 96, 117]. In the Eulerian-Lagrangian approach, Newton's second law is applied to solid phase to solve the motion of each particle in the flow, and therefore, the particle-particle and particle-wall interactions are described in a realistic way. The fluid phase is considered as a continuous phase, and Navier-Stokes equations are solved with closures for gas-particle interactions. The computational cost for Eulerian-Lagrangian approach is usually high, and hence the approach is limited to very dilute systems [1,18,96,117]. In the Eulerian-Eulerian approach, the fluid and solid phases are both considered as continua, and Navier-Stokes equations are solved for both phases. Closure models are applied to account for gas-particle and particle-particle interactions. The Eulerian-Eulerian approach is computationally efficient, and can be applied to relatively large and dense systems [1,28,40,41,96,117].

In most of CFD simulations using either Eulerian-Lagrangian approach or Eulerian-Eulerian approach, the simulation results are single values or deterministic values without statistics provided to quantify the uncertainties introduced by factors such as uncertain input parameters [31]. The objective of uncertainty quantification (UQ) is to study the propagation of uncertainty in model inputs to simulation outputs so that computational predictions with confidence intervals can be provided [16]. Two methods can be used to implement UQ approaches into CFD codes. Intrusive approach introduces the uncertainty into the computational model by reformulating the governing equations, which are only solved once, and therefore the approach is computationally efficient. However, for complex systems such as multiphase flows, it requires a great deal of modifications to the original computational codes, which makes it difficult to implement the approach into multiphase CFD simulations. On the contrary, by using the original models directly, non-intrusive approaches are usually considered for complicated practical systems. For non-intrusive approaches, sampling strategy is the key element because the CFD simulation is performed once for each sample, and the computational cost of the approaches scales with the number of samples. For problems with a large amount of

uncertain input parameters, Monte Carlo based random sampling strategies are usually considered because the convergence of the methods is independent of the number of random input parameters. However, the slow convergence of high order moments with respect to the number of samples limits the applications of the methods to computationally intense problems [58]. For problems with a moderate number of uncertain input parameters, by using deterministic sampling strategies such as quadrature-based sampling strategy, the number of samples required and hence the computational cost can be reduced significantly [73].

In this chapter, the non-intrusive quadrature-based uncertainty quantification (QBUQ) approach first proposed by Yoon et al. [4,119] is applied to a riser flow simulation with the particle diameter considered as the uncertain input parameter. The space of the distribution of uncertain particle diameter is sampled using Gaussian quadrature formulae [42]. A CFD simulation is performed for each sample, and the moments of the system response are directly estimated from the simulation results using quadrature formulae [4,119]. The simulation results with confidence intervals are compared to the experimental data. The set of moments are also used to reconstruct the PDF of the system response at specific locations of the computational domain using EQMOM [14, 121] for univariate PDF reconstruction and ECQMOM for bivariate PDF reconstruction.

5.2 Quadrature-Based UQ Approach

The basic idea of QBUQ is to directly evaluate the moments of the system response [4, 119] using Gaussian quadrature formulae [42]. The method used to sample the space of the distribution of uncertain parameters and to find corresponding weights and nodes depends on the number of uncertain input parameters. For univariate problems, a one dimensional Gaussian quadrature formula is used [29, 42], described in Section 4.2.1 and Appendix A. For problems with multiple input parameters with uncertainty, samples can be generated using a moment inversion algorithm, conditional quadrature method of moments (CQMOM), proposed by Yuan and Fox [120], and illustrated in Section 4.2.2. For each sample, the CFD simulation is performed once. Then the simulation results of quantities of interest of each sample is used as quadrature abscissas to directly approximate the moments of the system response.

The set of moments of the system response can be used to calculate the statistics including mean, variance, skewness, and kurtosis using Eq. 2.3 to Eq. 2.6 in Section 2.2. The moments can also be used to reconstruct the PDF of the system response using EQMOM [14, 121] and ECQMOM. The procedure of univariate PDF reconstruction using EQMOM with different kernel density functions is described in detail in Sections 2.4 and 4.3, Appendix C, and literature [14,121]. Here the procedure for multivariate PDF reconstruction using ECQMOM is explained.

5.2.1 Multivariate PDF reconstruction

The idea of using ECQMOM for multivariate PDF reconstruction is to combine EQMOM with CQMOM [120] described in Section 4.2.2 so that a multivariate reconstruction problem can be transformed into a series of univariate reconstruction problems. For the sake of simplicity and clarity, a 4-node (2×2) Gaussian ECQMOM, which is a bivariate extension of 2-node Gaussian EQMOM combined with CQMOM, is illustrated as a demonstration of the method. The same methodology can be extended to more nodes for each variable, more variables, and other kernel density functions.

The bivariate moments of the system response $\boldsymbol{\kappa} = (\kappa_1, \kappa_2)$ are defined as

$$m_{i,j} = \int_{\mathbb{R}^2} \kappa_1^i \kappa_2^j \, \mathrm{d}\boldsymbol{\kappa}, \;\; i, j = 0, 1, 2, \ldots, \tag{5.1}$$

which can be directly approximated using the QBUQ procedure. A 4-node bivariate Gaussian distribution is then defined as

$$f_{12}(\kappa_1, \kappa_2) = \sum_{\alpha=1}^{2} \rho_\alpha g(\kappa_1; \kappa_{1\alpha}, \sigma_1) \left(\sum_{\beta=1}^{2} \rho_{\alpha\beta} g(\kappa_2 - K(\kappa_1); \kappa_{2\alpha\beta}, \sigma_{2\alpha}) \right), \tag{5.2}$$

where the Gaussian kernel density function g is

$$g(x; \mu, \sigma) = \frac{1}{\sigma\sqrt{2\pi}} \exp\left(-\frac{(x-\mu)^2}{2\sigma^2} \right). \tag{5.3}$$

In Eq. 5.2, the subscript of f_{12} indicates the conditioning order, and here it is κ_2 conditioned on κ_1.

The function $K(\kappa_1)$ in Eq. 5.2 is defined to have the properties shown in Eq. 5.4,

$$\sum_{\alpha=1}^{2} \rho_\alpha \int_{\mathbb{R}} \kappa_1^i K(\kappa_1) g(\kappa_1; \kappa_{1\alpha}, \sigma_1) \mathrm{d}\kappa_1 = m_{i,1}, \;\; i = 0, 1. \tag{5.4}$$

A choice for $K(\kappa_1)$ is a linear function $K(\kappa_1) = c_0 + c_1\kappa_1$, where c_0 and c_1 and be calculated as

$$c_0 = \frac{m_{2,0}m_{0,1} - m_{1,0}m_{1,1}}{m_{0,0}m_{2,0} - m_{1,0}^2} = \mu_{\kappa_2} - \mu_{\kappa_1}c_1, \tag{5.5}$$

and

$$c_1 = \frac{m_{0,0}m_{1,1} - m_{1,0}m_{0,1}}{m_{0,0}m_{2,0} - m_{1,0}^2} = \frac{\rho\sigma_{\kappa_2}}{\sigma_{\kappa_1}}, \tag{5.6}$$

with

$$\mu_{\kappa_1} = \frac{m_{1,0}}{m_{0,0}},\ \sigma_{\kappa_1}^2 = \frac{m_{2,0}}{m_{0,0}} - \mu_{\kappa_1}^2,\ \mu_{\kappa_2} = \frac{m_{0,1}}{m_{0,0}},\ \sigma_{\kappa_2}^2 = \frac{m_{0,2}}{m_{0,0}} - \mu_{\kappa_2}^2, \text{ and } \rho = \frac{m_{1,1}/m_{0,0} - \mu_{\kappa_1}\mu_{\kappa_2}}{\sigma_{\kappa_1}\sigma_{\kappa_2}}.$$

It is worth noting that $K(\kappa_1)$ is well defined if the standard deviation in the κ_1 direction σ_{κ_1} is nonzero, and in fact, $K(\kappa_1)$ is the conditional expected value of κ_2 given κ_1.

The reconstruction in the κ_1 direction is a univariate reconstruction problem, in which known integer moments set $\{m_{0,0}, m_{1,0}, m_{2,0}, m_{3,0}, m_{4,0}\}$ is used to compute nodes and corresponding weights using Gaussian EQMOM described in Appendix C and in literature [14,108]. The next step is to reconstruct the PDF in the κ_2 direction. To simplify the notation, the following definition is introduced,

$$\langle \kappa_1^i K^j \rangle_\alpha \equiv \int_{\mathbb{R}} \kappa_1^i K(\kappa_1)^j g(\kappa_1; \kappa_{1\alpha}, \sigma_1) \mathrm{d}\kappa_1, \tag{5.7}$$

where Gaussian integer moments up to order of $i + j$ are involved, which are known functions of $\kappa_{1\alpha}$ and σ_1.

Define $y = \kappa_2 - K(\kappa_1)$, then the integer moments of f_{12} in Eq. 5.2 can be expressed as

$$\begin{aligned} m_{i,j}^{\mathrm{G}} &= \sum_{\alpha=1}^{2} \rho_\alpha \int_{\mathbb{R}} \kappa_1^i g(\kappa_1; \kappa_{1\alpha}, \sigma_1) \left(\sum_{\beta=1}^{2} \rho_{\alpha\beta} \int_{\mathbb{R}} \kappa_2^j g(\kappa_2 - K(\kappa_1); \kappa_{2\alpha\beta}, \sigma_{2\alpha}) \mathrm{d}\kappa_2 \right) \mathrm{d}\kappa_1 \\ &= \sum_{\alpha=1}^{2} \rho_\alpha \int_{\mathbb{R}} \kappa_1^i g(\kappa_1; \kappa_{1\alpha}, \sigma_1) \left(\sum_{\beta=1}^{2} \rho_{\alpha\beta} \int_{\mathbb{R}} [y + K(\kappa_1)]^j g(y; \kappa_{2\alpha\beta}, \sigma_{2\alpha}) \mathrm{d}y \right) \mathrm{d}\kappa_1. \end{aligned} \tag{5.8}$$

With the conditional moments of y given $\kappa_1 = \kappa_{1\alpha}$ defined as

$$\mu_\alpha^j = \sum_{\beta=1}^{2} \rho_{\alpha\beta} \int_{\mathbb{R}} y^j g(y; \kappa_{2\alpha\beta}, \sigma_{2\alpha}) \mathrm{d}y, \tag{5.9}$$

a binomial expansion for integer j can be written as

$$m_{i,j}^{\mathrm{G}} = \sum_{\alpha=1}^{2} \rho_\alpha \sum_{j_1=0}^{j} \binom{j}{j_1} \langle \kappa_1^i K^{j-j_1} \rangle_\alpha \mu_\alpha^{j_1}. \tag{5.10}$$

The unique solution to Eq. 5.10 when $i = 0, 1$ and $j = 0$ is $\mu_\alpha^0 = 1$, and likewise the solution for the equation with $i = 0, 1$ and $j = 1$ is $\mu_\alpha^1 = 0$ using properties of $K(\kappa_1)$ in Eq. 5.4. In order to determine $\kappa_{2\alpha\beta}$, $\rho_{\alpha\beta}$, and $\sigma_{2\alpha}$, Eq. 5.10 needs to be solved to obtain $\mu_\alpha^{j_1}$ for $j_1 = 2, 3, 4$, which is straightforward by solving the following linear systems sequentially (Eq. 5.11 to Eq. 5.13):

$$\begin{aligned} \sum_{\alpha=1}^{2} \rho_\alpha \mu_\alpha^2 &= m_{0,2} - \sum_{\alpha=1}^{2} \rho_\alpha \langle K^2 \rangle_\alpha, \\ \sum_{\alpha=1}^{2} \rho_\alpha \kappa_{1\alpha} \mu_\alpha^2 &= m_{1,2} - \sum_{\alpha=1}^{2} \rho_\alpha \langle \kappa_1 K^2 \rangle_\alpha; \end{aligned} \tag{5.11}$$

$$\begin{aligned} \sum_{\alpha=1}^{2} \rho_\alpha \mu_\alpha^3 &= m_{0,3} - 3\sum_{\alpha=1}^{2} \rho_\alpha \langle K \rangle_\alpha \mu_\alpha^2 - \sum_{\alpha=1}^{2} \rho_\alpha \langle K^3 \rangle_\alpha, \\ \sum_{\alpha=1}^{2} \rho_\alpha \kappa_{1\alpha} \mu_\alpha^3 &= m_{1,3} - 3\sum_{\alpha=1}^{2} \rho_\alpha \langle \kappa_1 K \rangle_\alpha \mu_\alpha^2 - \sum_{\alpha=1}^{2} \rho_\alpha \langle \kappa_1 K^3 \rangle_\alpha; \end{aligned} \tag{5.12}$$

$$\begin{aligned} \sum_{\alpha=1}^{2} \rho_\alpha \mu_\alpha^4 &= m_{0,4} - 4\sum_{\alpha=1}^{2} \rho_\alpha \langle K \rangle_\alpha \mu_\alpha^3 - 6\sum_{\alpha=1}^{2} \rho_\alpha \langle K^2 \rangle_\alpha \mu_\alpha^2 - \sum_{\alpha=1}^{2} \rho_\alpha \langle K^4 \rangle_\alpha, \\ \sum_{\alpha=1}^{2} \rho_\alpha \kappa_{1\alpha} \mu_\alpha^4 &= m_{1,4} - 4\sum_{\alpha=1}^{2} \rho_\alpha \langle \kappa_1 K \rangle_\alpha \mu_\alpha^3 - 6\sum_{\alpha=1}^{2} \rho_\alpha \langle \kappa_1 K^2 \rangle_\alpha \mu_\alpha^2 - \sum_{\alpha=1}^{2} \rho_\alpha \langle \kappa_1 K^4 \rangle_\alpha. \end{aligned} \tag{5.13}$$

Once the set of conditional moments $\{1, 0, \mu_\alpha^2, \mu_\alpha^3, \mu_\alpha^4\}$ for $\alpha \in \{1, 2\}$ is obtained, univariate Gaussian EQMOM can be applied again to determine $\kappa_{2\alpha\beta}$, $\rho_{\alpha\beta}$, and $\sigma_{2\alpha}$.

When the univariate moments $m_{i,0}$ with 1-D Gaussian EQMOM are used to find ρ_1, ρ_2, κ_{11}, κ_{12}, and σ_1, two cases can be possible: a nondegenerate case with $\kappa_{11} \neq \kappa_{12}$ and a degenerate case with $\kappa_{11} = \kappa_{12}$. The above procedure is suitable for the nondegenerate case. For the degenerate case, the univariate moments $m_{i,0}$ are Gaussian, and the (2×2)-node Gaussian ECQMOM degenerates to a 2-node Gaussian ECQMOM because only one node is used to represent the PDF of the first direction.

For the degenerate case, a 2-node bivariate Gaussian distribution is defined as

$$f_{12}(\kappa_1, \kappa_2) = m_{0,0} g(\kappa_1; \mu_{\kappa_1}, \sigma_{\kappa_1}) \left(\sum_{\alpha=1}^{2} \rho_\alpha g(\kappa_2 - K(\kappa_1); \kappa_{2\alpha}, \sigma_2) \right). \tag{5.14}$$

The integer moments of f_{12} can be expressed as

$$m_{i,j}^{\mathrm{G}} = m_{0,0} \sum_{j_1=0}^{j} \binom{j}{j_1} \langle \kappa_1 K^{j-j_1} \rangle \mu^{j_1}, \tag{5.15}$$

where

$$\langle \kappa_1^i K^j \rangle = \int_{\mathbb{R}} \kappa_1^i K(\kappa_1)^j g(\kappa_1; \mu_{\kappa_1}, \sigma_{\kappa_1}) \mathrm{d}\kappa_1, \tag{5.16}$$
$$\langle K \rangle = \frac{m_{0,1}}{m_{0,0}} = \mu_{\kappa_2}, \ \langle \kappa_1 K \rangle = \frac{m_{1,1}}{m_{0,0}},$$

and the conditional moments are defined as

$$\mu^j = \sum_{\alpha=1}^{2} \rho_\alpha \int_{\mathbb{R}} (\kappa_2 - K(\kappa_1))^j g(\kappa_2 - K(\kappa_1); \kappa_{2\alpha}, \sigma_2) \mathrm{d}\kappa_2 = \sum_{\alpha=1}^{2} \rho_\alpha \int_{\mathbb{R}} y^j g(y; \kappa_{2\alpha}, \sigma_2) \mathrm{d}y, \tag{5.17}$$

with $y = \kappa_2 - K(\kappa_1)$, $\mu^0 = 1$, and $\mu^1 = 0$ by definition. The conditional moments μ^2, μ^3, and μ^4 can be found from Eq. 5.15 for $i = 0$ and $j = 2, 3, 4$:

$$\begin{aligned} \mu^2 &= \frac{m_{0,2}}{m_{0,0}} - \langle K^2 \rangle, \\ \mu^3 &= \frac{m_{0,3}}{m_{0,0}} - \langle K^3 \rangle - 3\langle K \rangle \mu^2, \\ \mu^4 &= \frac{m_{0,4}}{m_{0,0}} - \langle K^4 \rangle - 6\langle K^2 \rangle \mu^2 - 4\langle K \rangle \mu^3, \end{aligned} \tag{5.18}$$

where the moments $\langle K^j \rangle$ can be calculated from Eq. 5.16 with $i = 0$. With the moment set $\{1, 0, \mu^2, \mu^3, \mu^4\}$, 1-D Gaussian EQMOM can be used to determine ρ_α, $\kappa_{2\alpha}$, and σ_2 for $\alpha = 1, 2$. With the above procedure, the 2-D Gaussian ECQMOM is complete for both nondegenerate and degenerate cases.

5.3 Application of QBUQ to a Riser Flow

The QBUQ approach with PDF reconstruction is applied to a riser flow studied experimentally and computationally by Tartan and Gidaspow [102]. The propagation of uncertainty in particle diameter to simulation outputs including solid volume fraction, solid phase velocities, and granular temperature is studied. Contour plots of mean and standard deviation of the system response are provided. Time-averaged simulation results with confidence intervals are compared to the experimental data. The PDF of the response is reconstructed at specific locations in the computational domain.

5.3.1 Descriptions of the computational problem

A two-dimensional riser flow simulation was set up based on the experiments conducted in the IIT CFB reactor described in Tartan and Gidaspow [102]. The riser of IIT CFB possessed a diameter of 7.62 cm and a height of 699 cm. Geldart B particles were used in the experiments. In this work, the simulations are performed in a 2-D channel with width of 7.62 cm and height of 699 cm, discretized by 40×466 cells. The riser is initially empty. The mixture of glass beads and air is injected uniformly from the bottom of the channel, and exits from the top. MFIX (Multiphase Flow with Interface eXchanges), an open source code developed by the National Energy Technology Laboratory (NETL) of Department of Energy (DOE) (http://mfix.netl.doe.gov), is used to simulate the riser flow. The simulation conditions and parameters are listed in Table 5.1.

Table 5.1 Simulation parameters and conditions.

Parameters and conditions	Values
Gas density	1.184 kg/m^3
Particle density	2460 kg/m^3
Mean particle diameter	530 μm
Particle-particle restitution coefficient	0.95
Particle-wall Restitution coefficient	0.6
Specularity coefficient	0.007
Inlet superficial gas velocity	4.90 m/s
Inlet solid mass flux	14.2 kg/m$^2 \cdot$ s
Inlet solid volume fraction	0.98
Exit boundary condition	zero relative gas pressure
Wall boundary condition for gas phase	No-slip
Wall boundary condition for solid phase	Johnson-Jackson [49]
Simulation time	90 s
Starting time steps	1.0×10^{-4} s
Convergence criteria	1.0×10^{-3}

5.3.2 Governing equations

A two-fluid model (Eulerian-Eulerian approach) [21, 23] with kinetic theory closures for particulate phase [40] is used to solve the multiphase flow in the riser. The governing and constitutive equations are summarized in Table 5.2 and Table 5.3. At the walls, no-slip bound-

ary condition and Johnson-Jackson boundary condition [49] are applied to gas phase and solid phase, respectively, shown in Table 5.4.

Table 5.2 Governing equations. Representation of symbols: subscript g – gas phase, subscript s – solid phase, α_{i} – phase volume fraction, ρ_{i} – density, $\mathbf{U}_{\mathrm{i}}$ – phase velocity field, p_{g} – gas pressure, $\mathbf{g}$ – acceleration of gravity, Θ_{s} – granular temperature, $\mathbf{I}$ – unit tensor, d_{s} – particle diameter, and μ_{g} – shear viscosity of gas.

Gas phase continuity
$$\frac{\partial}{\partial t}\left(\alpha_{\mathrm{g}}\rho_{\mathrm{g}}\right)+\nabla\cdot\left(\alpha_{\mathrm{g}}\rho_{\mathrm{g}}\mathbf{U}_{\mathrm{g}}\right)=0$$

Solid phase continuity
$$\frac{\partial}{\partial t}\left(\alpha_{\mathrm{s}}\rho_{\mathrm{s}}\right)+\nabla\cdot\left(\alpha_{\mathrm{s}}\rho_{\mathrm{s}}\mathbf{U}_{\mathrm{s}}\right)=0$$

Gas phase momentum
$$\frac{\partial}{\partial t}\left(\alpha_{\mathrm{g}}\rho_{\mathrm{g}}\mathbf{U}_{\mathrm{g}}\right)+\nabla\cdot\left(\alpha_{\mathrm{g}}\rho_{\mathrm{g}}\mathbf{U}_{\mathrm{g}}\mathbf{U}_{\mathrm{g}}\right)=-\alpha_{\mathrm{g}}\nabla p_{\mathrm{g}}+\nabla\cdot\boldsymbol{\tau}_{\mathrm{g}}+\alpha_{\mathrm{g}}\rho_{\mathrm{g}}\mathbf{g}+K_{\mathrm{gs}}\left(\mathbf{U}_{\mathrm{s}}-\mathbf{U}_{\mathrm{g}}\right)$$

Solid phase momentum
$$\frac{\partial}{\partial t}\left(\alpha_{\mathrm{s}}\rho_{\mathrm{s}}\mathbf{U}_{\mathrm{s}}\right)+\nabla\cdot\left(\alpha_{\mathrm{s}}\rho_{\mathrm{s}}\mathbf{U}_{\mathrm{s}}\mathbf{U}_{\mathrm{s}}\right)=-\alpha_{\mathrm{s}}\nabla p_{\mathrm{g}}-\nabla p_{\mathrm{s}}+\nabla\cdot\boldsymbol{\tau}_{\mathrm{s}}+\alpha_{\mathrm{s}}\rho_{\mathrm{s}}\mathbf{g}-K_{\mathrm{gs}}\left(\mathbf{U}_{\mathrm{s}}-\mathbf{U}_{\mathrm{g}}\right)$$

Granular temperature
$$\frac{3}{2}\left[\frac{\partial}{\partial t}\left(\alpha_{\mathrm{s}}\rho_{\mathrm{s}}\Theta_{\mathrm{s}}\right)+\nabla\cdot\left(\alpha_{\mathrm{s}}\rho_{\mathrm{s}}\mathbf{U}_{\mathrm{s}}\Theta_{\mathrm{s}}\right)\right]=\left(-p_{\mathrm{s}}\mathbf{I}+\boldsymbol{\tau}_{\mathrm{s}}\right):\nabla\mathbf{U}_{\mathrm{s}}+\nabla\cdot\left(k_{\mathrm{s}}\nabla\Theta_{\mathrm{s}}\right)-\gamma_{\mathrm{s}}-3K_{\mathrm{gs}}\Theta_{\mathrm{s}}$$

Gidaspow gas-solid drag correlation
$$K_{gs}=\begin{cases}\dfrac{3}{4}C_D\dfrac{\rho_{\mathrm{g}}\alpha_{\mathrm{g}}\alpha_{\mathrm{s}}\left|\mathbf{U}_{\mathrm{s}}-\mathbf{U}_{\mathrm{g}}\right|}{d_{\mathrm{s}}}\alpha_{\mathrm{g}}^{-2.65} & \alpha_{\mathrm{g}}\geq 0.8\\ \dfrac{150\alpha_{\mathrm{s}}^2\mu_{\mathrm{g}}}{\alpha_{\mathrm{g}}d_{\mathrm{s}}^2}+\dfrac{1.75\rho_{\mathrm{g}}\alpha_{\mathrm{s}}\left|\mathbf{U}_{\mathrm{s}}-\mathbf{U}_{\mathrm{g}}\right|}{d_{\mathrm{s}}} & \alpha_{\mathrm{g}}<0.8\end{cases}$$
$$C_D=\begin{cases}\dfrac{24}{\mathrm{Re}}\left(1+0.15\,\mathrm{Re}\right)^{0.687} & \mathrm{Re}<1000\\ 0.44 & \mathrm{Re}\geq 1000\end{cases}$$
$$\mathrm{Re}=\frac{\rho_{\mathrm{g}}\alpha_{\mathrm{g}}\left|\mathbf{U}_{\mathrm{s}}-\mathbf{U}_{\mathrm{g}}\right|d_{\mathrm{s}}}{\mu_{\mathrm{g}}}$$

5.3.3 Descriptions of the uncertain parameter

In reality, particle size is not a single value, and a distribution of particle size always exists. In this work, the effect of uncertain particle size on the simulation outputs is studied. The PDF of particle diameter is assumed to be a uniform distribution with mean value $\bar{d}_{\mathrm{s}}$ and standard

Table 5.3 Constitutive equations. Representation of symbols: e_{pp} – particle-particle restitution coefficient, ϕ – angle of internal friction, I_{2D} – the second invariant of the deviator of the strain-rate tensor, and $\alpha_{\mathrm{s,max}}$ – packing limit.

Gas-phase stress tensor	$\boldsymbol{\tau}_{\mathrm{g}} = \alpha_{\mathrm{g}}\mu_{\mathrm{g}}\left[\nabla\mathbf{U}_{\mathrm{g}} + (\nabla\mathbf{U}_{\mathrm{g}})^{\mathrm{T}}\right] - \frac{2}{3}\alpha_{\mathrm{g}}\mu_{\mathrm{g}}\left(\nabla\cdot\mathbf{U}_{\mathrm{g}}\right)\mathbf{I}$
Solid-phase stress tensor	$\boldsymbol{\tau}_{\mathrm{s}} = \alpha_{\mathrm{s}}\mu_{\mathrm{s}}\left[\nabla\mathbf{U}_{\mathrm{s}} + (\nabla\mathbf{U}_{\mathrm{s}})^{\mathrm{T}}\right] + \alpha_{\mathrm{s}}\left(\lambda_{\mathrm{s}} - \frac{2}{3}\mu_{\mathrm{s}}\right)\left(\nabla\cdot\mathbf{U}_{\mathrm{s}}\right)\mathbf{I}$
Solids pressure	$p_{\mathrm{s}} = \alpha_{\mathrm{s}}\rho_{\mathrm{s}}\Theta_{\mathrm{s}} + 2(1+e_{\mathrm{pp}})\alpha_{\mathrm{s}}^2\rho_{\mathrm{s}}g_0\Theta_{\mathrm{s}}$
Solids bulk viscosity	$\lambda_{\mathrm{s}} = \frac{4}{3}\alpha_{\mathrm{s}}\rho_{\mathrm{s}}d_{\mathrm{s}}g_0(1+e_{\mathrm{pp}})\sqrt{\frac{\Theta_{\mathrm{s}}}{\pi}}$
Solids shear viscosity	$\mu_{\mathrm{s}} = \mu_{\mathrm{s,kin}} + \mu_{\mathrm{s,fr}}$
Solids kinetic viscosity	$\mu_{\mathrm{s,kin}} = \frac{10\rho_{\mathrm{s}}d_{\mathrm{s}}\sqrt{\pi\Theta_{\mathrm{s}}}}{96\alpha_{\mathrm{s}}g_0(1+e_{\mathrm{pp}})}\left[1+\frac{4}{5}\alpha_{\mathrm{s}}g_0(1+e_{\mathrm{pp}})\right]^2$
Solids frictional viscosity	$\mu_{\mathrm{s,fr}} = \frac{p_{\mathrm{s}}\sin\phi}{2\sqrt{I_{2D}}}$
Radial distribution function	$g_0 = \left[1-\left(\frac{\alpha_{\mathrm{s}}}{\alpha_{\mathrm{s,max}}}\right)^{\frac{1}{3}}\right]^{-1}$
Solids conductivity	
$k_{\mathrm{s}} = \frac{150\rho_{\mathrm{s}}d_{\mathrm{s}}\sqrt{\pi\Theta_{\mathrm{s}}}}{384g_0(1+e_{\mathrm{pp}})}\left[1+\frac{6}{5}\alpha_{\mathrm{s}}g_0(1+e)\right]^2 + 2\alpha_{\mathrm{s}}^2\rho_s d_s g_0(1+e)\sqrt{\frac{\Theta_{\mathrm{s}}}{\pi}}$	
Collisional dissipation	$\gamma_{\mathrm{s}} = \frac{12\alpha_{\mathrm{s}}^2\rho_{\mathrm{s}}g_0(1-e_{\mathrm{pp}}^2)}{d_{\mathrm{s}}\sqrt{\pi}}\Theta_{\mathrm{s}}^{3/2}$

Table 5.4 Wall boundary conditions. Representation of symbols: $\mathbf{U}_{\mathrm{il}}$ – slip velocity between gas or solid and the wall, $\mathbf{n}$ – unit vector normal to the wall, ϕ_{s} – specularity coefficient, and e_{pw} – particle-wall restitution coefficient.

Gas phase	$\mathbf{U}_{\mathrm{gl}} = \mathbf{0}$
Solid phase	
$\mathbf{n}\cdot(\mu_{\mathrm{s}}\nabla\mathbf{U}_{\mathrm{sl}}) = -\frac{\pi\phi_{\mathrm{s}}\alpha_{\mathrm{s}}\rho_{\mathrm{s}}g_0\sqrt{3\Theta_{\mathrm{s}}}}{6\alpha_{\mathrm{s,max}}}\mathbf{U}_{\mathrm{sl}}$	
$\mathbf{n}\cdot(k_{\mathrm{s}}\nabla\Theta_{\mathrm{s}}) = \frac{\pi\alpha_{\mathrm{s}}\rho_{\mathrm{s}}g_0\lvert\mathbf{U}_{\mathrm{sl}}\rvert^2\sqrt{3\Theta_{\mathrm{s}}}}{6\alpha_{\mathrm{s,max}}} - \frac{\sqrt{3}\pi\alpha_{\mathrm{s}}\rho_{\mathrm{s}}g_0(1-e_{\mathrm{pw}})^2}{4\alpha_{\mathrm{s,max}}}\Theta_{\mathrm{s}}^{3/2},$	

deviation being 530 μm and $0.1\bar{d}_{\mathrm{s}}$, respectively. Hence the particle diameter d_{s} is uniformly distributed on the interval $[477, 583]$. In total 20 samples are generated using the sampling method for one uncertain parameter described in previous chapters.

5.3.4 Results and discussion

For each sample, MFIX simulation is performed once. The moments of the system response are directly estimated using Gaussian quadrature formulae [4, 42, 119]. The influences of uncertain particle size on four time-averaged quantities of interest are evaluated, including solid volume fraction α_{s}, solid radial velocity u_{s}, solid axial velocity v_{s}, and granular temperature Θ_{s}. These four quantities are time-averaged from 50 s to 90 s. Results are discussed below.

5.3.4.1 Low order statistics

Figure 5.1 shows the contour plots of mean and standard deviation of the solid volume fraction. Because of the large ratio of the height to the diameter of the riser, the riser is cut into four parts at height of 175 cm, 350 cm, and 525 cm so that details of the contour plots can be displayed. The contour plots are all shown in this way if not stated otherwise. Core-annular structure is observed as expected, though the annulus is very thin. The annulus is relatively dense, while the core is dilute. The concentration of the particles decreases with increasing the distance from the bottom of the channel. The effect of uncertain particle size on the solid volume fraction focuses on the bottom of the riser, the annulus, and some spots near the wall at very high positions of the riser.

The designated points in Figure 5.1 are the locations where the reconstruction of the PDF of the system response is performed, and at the same height, the experimental results are obtained. Location 1 is at the centerline, while location 2 is near the wall. If not stated otherwise, all designated points in all figures of this section have the same coordinates, listed in Table 5.5.

Figure 5.2 gives the contour plots of mean and standard deviation of solid radial velocity. After the initial mixing near the bottom of the riser, particles are moving towards the wall, which can explain the dilute core and dense annulus structure. With increasing the distance

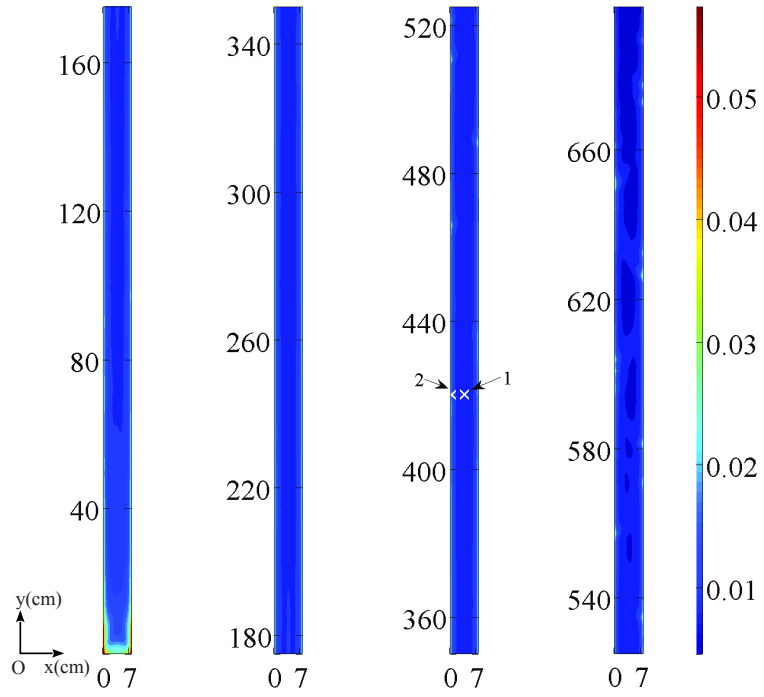

(a) mean

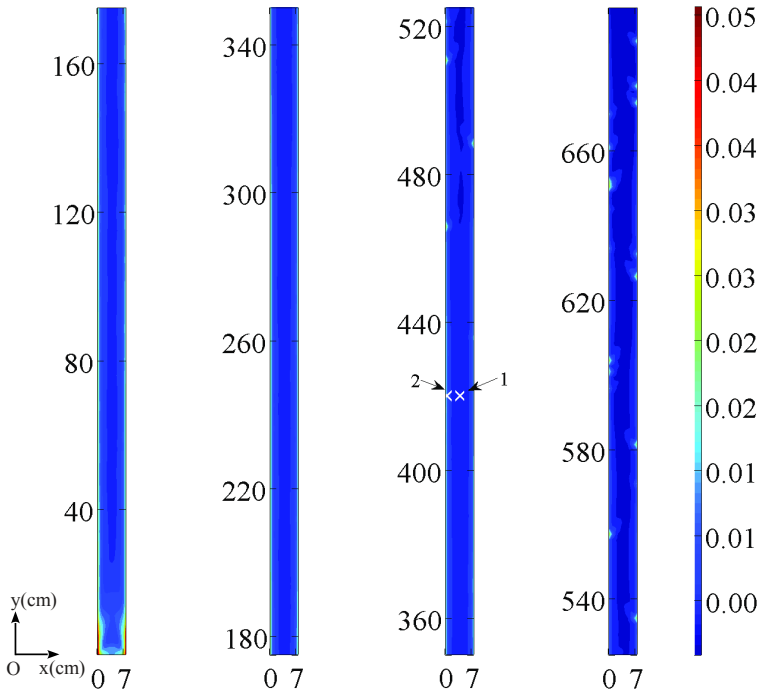

(b) standard deviation

Figure 5.1 Contour plots of (a) mean and (b) standard deviation of solid volume fraction.

Table 5.5 Coordinates of the designated locations.

Location	Coordinates	
	x	y
1	3.810	420.00
2	0.381	420.00

from the bottom of the riser, the absolute value of the solid radial velocity increases, and particles are pushed from one side of the riser to the other side. The influence of uncertain particle size on solid radial velocity concentrates mainly on the upper part of the channel and slightly on the locations near the inlet of the riser.

Figure 5.3 reports the contour plots of mean and standard deviation of solid axial velocity. Particles are moving faster in the core than in the annulus. The thickness of low velocity region increases, and the high velocity region starts to shift, with increasing the distance from the bottom of the riser. The standard deviation is larger in the annulus than in the core, which indicates uncertain particle size has more effect on solid axial velocity in the annulus than in the core.

Contour plots of mean and standard deviation of granular temperature are shown in Figure 5.4. The granular temperature is low in the annulus, while it is high in the core. In the core, the solids fluctuation is enhanced with increasing the distance from the bottom of the riser. The standard deviation of granular temperature also presents core-annular structure, with low value in the annulus. An interesting observation is that while the fluctuation is enhanced in the core, the standard deviation decreases with increasing the distance from the bottom of the riser. The influence of uncertain particle size on the granular temperature mainly focuses on the core region, especially on the lower part of the core.

5.3.4.2 Comparison to the experimental data

The simulation results are compared to the experimental data provided in the literature [102]. The upper and lower values of the confidence intervals are mean values plus and minus standard deviation, respectively. Results are presented in Figure 5.5, which indicates that the mean value of solid volume fraction has a good agreement with the experiment results, while

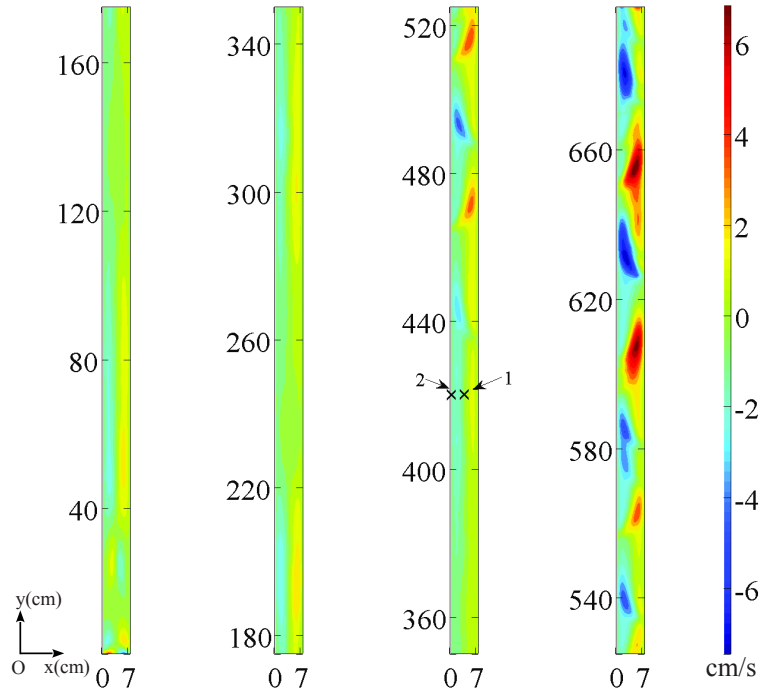

(a) mean

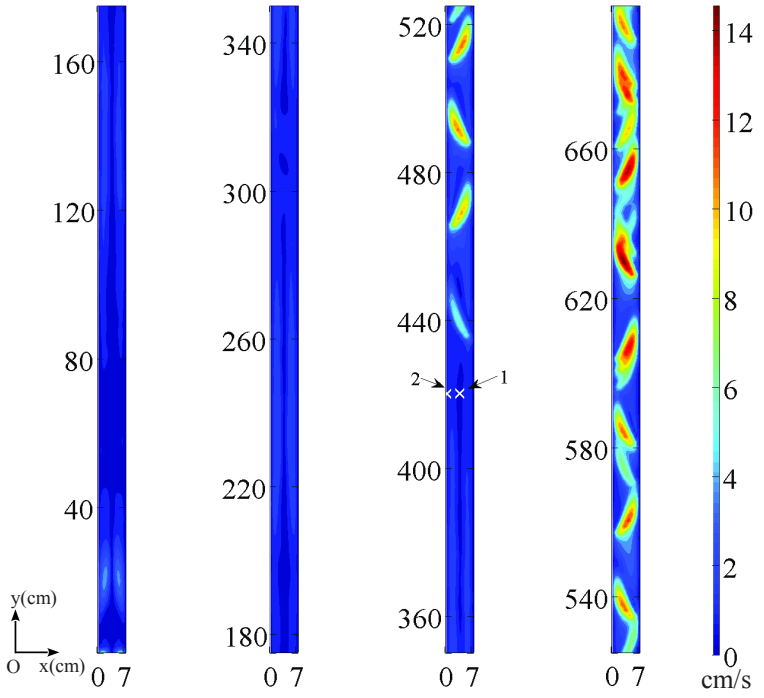

(b) standard deviation

Figure 5.2 Contour plots of (a) mean and (b) standard deviation of solid radial velocity.

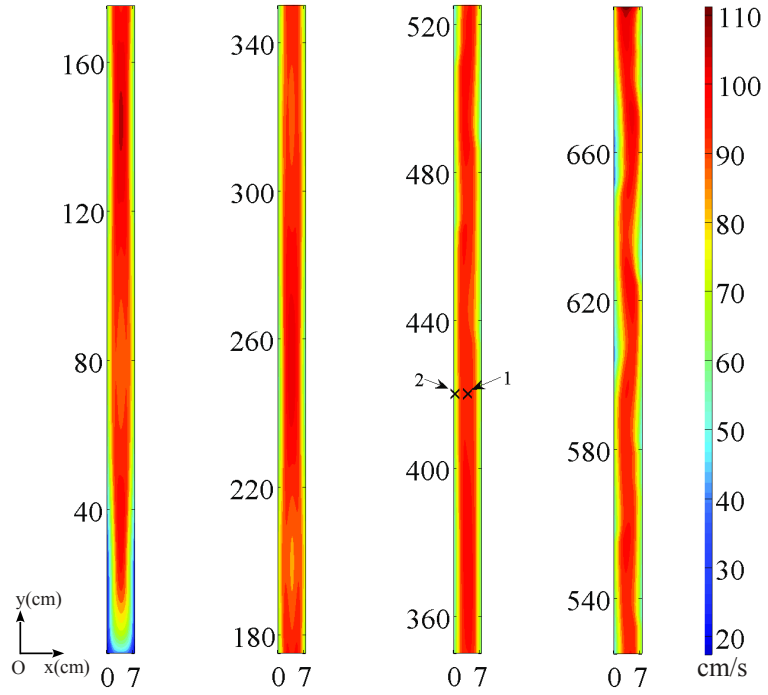

(a) mean

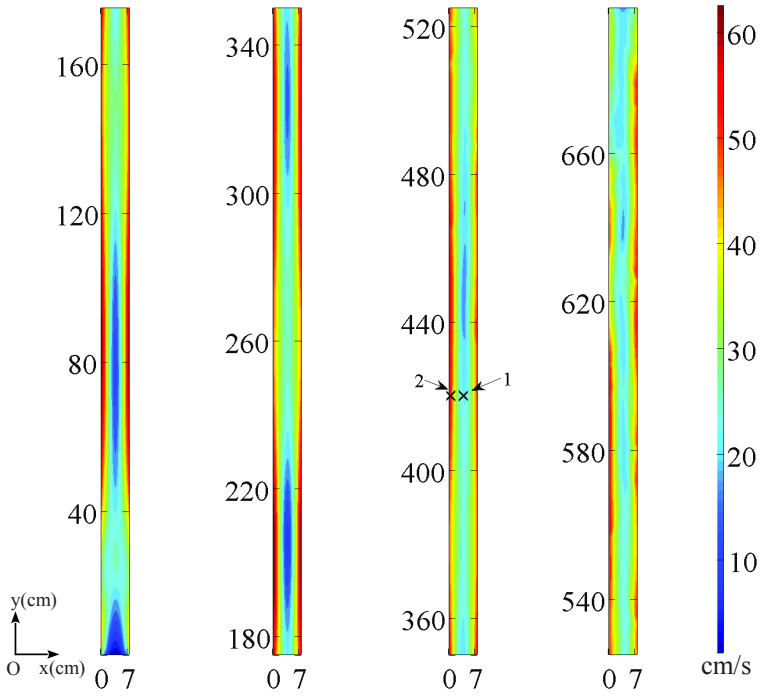

(b) standard deviation

Figure 5.3 Contour plots of (a) mean and (b) standard deviation of solid axial velocity.

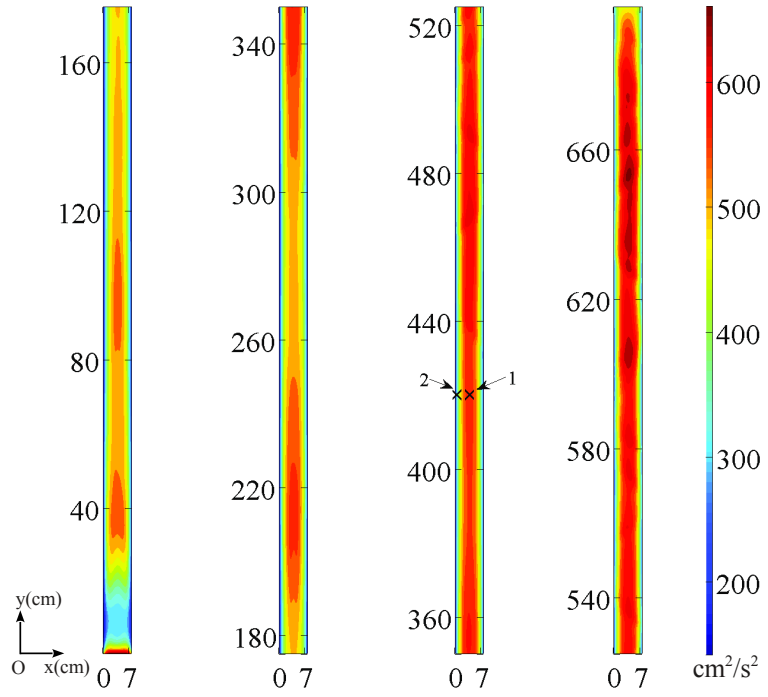

(a) mean

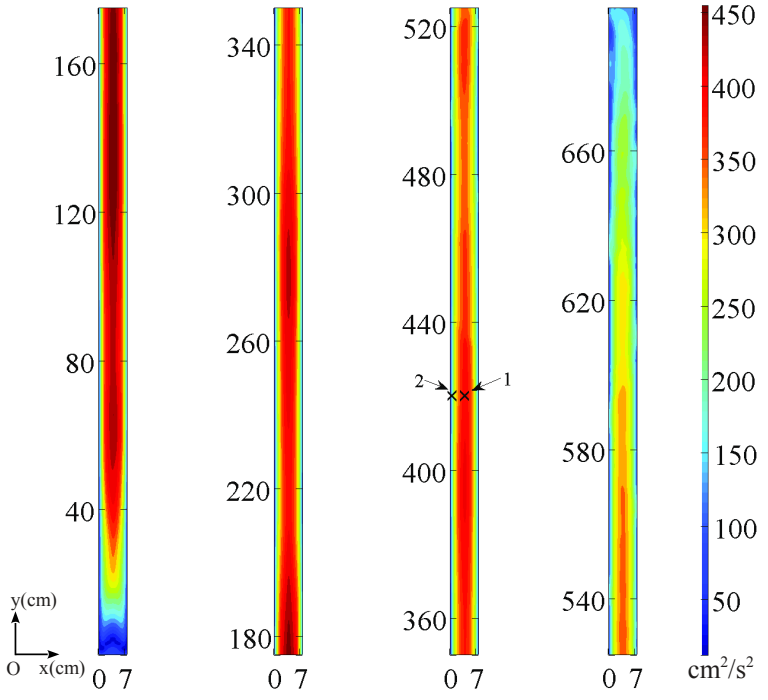

(b) standard deviation

Figure 5.4 Contour plots of (a) mean and (b) standard deviation of granular temperature.

fair agreements are obtained comparing the mean values of solid axial velocity and granular temperature to the experimental data. The shaded area in the figure represents the values between the upper and lower limits of the confidence interval of each response. With the confidence intervals, the predicted simulation results can cover most of the experimental data except that in Figure 5.5(b) some experiment data near the walls are outside the shaded area but close to the lower limit of the confidence interval of the predicted solid axial velocity, and in Figure 5.5(c) upper values of the error bars of two points exceed the upper boundary of the shaded area of granular temperature. This observation demonstrates that with UQ analysis performed by method like QBUQ to account for the uncertainty introduced by parameters like particle size, the reliability of the simulation results is improved, and these predicted values can be used with confidence for purpose of design and optimization.

5.3.4.3 PDF reconstruction of the system response

Two locations in the computational domain, designated in contour plots in Section 5.3.4.1 are used to reconstruct the PDF of system response. Univariate PDF reconstruction is performed for each system response using EQMOM [14, 121] described in previous chapters and Appendix C, and the joint PDF of solid axial and radial velocities is reconstructed using 4-node Gaussian ECQMOM illustrated in Section 5.2.1.

The PDF of the solid volume fraction is reconstructed using 2-node EQMOM with beta distribution as the kernel density function, results shown in Figure 5.6. For location 1, which is at the centerline, low solid volume fraction is preferred. For location 2, which is near the wall, the distribution is broad, and lower value has higher probability.

Figure 5.7 shows the reconstructed PDF of solid radial velocity using 2-node Gaussian EQMOM. For location 1, the peak of the distribution shows up at near zero velocity, with negative low velocity slightly preferred. At location 2, bimodal distribution is presented, with negative velocity having high probability.

Two-node Gaussian EQMOM is also used to reconstruct the PDF of solid axial velocity, results presented in Figure 5.8. Bimodal distribution is observed at both locations, yet when near the wall (location 2), the two peaks are completely separated. At the centerline (loca-

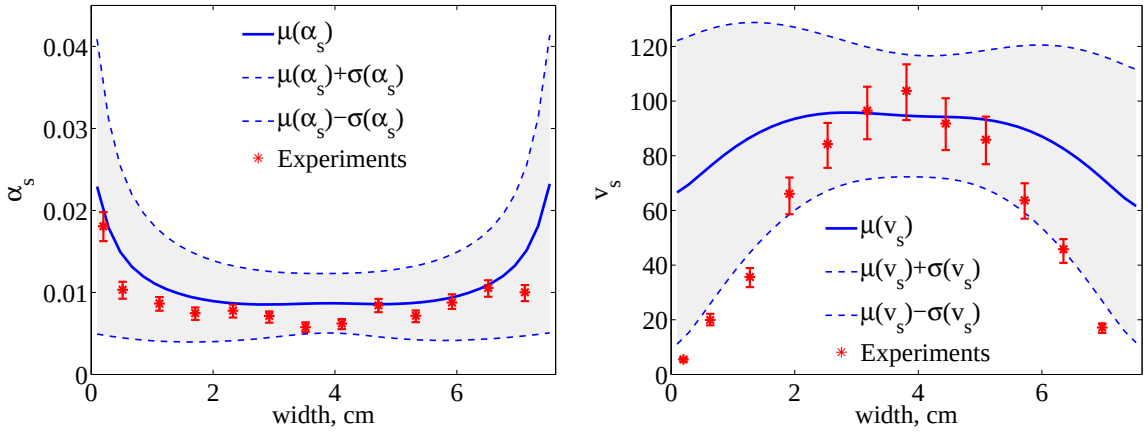

(a) α_s (b) v_s

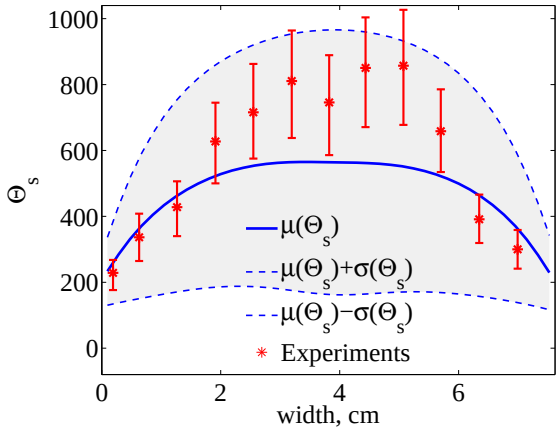

(c) Θ_s

Figure 5.5 Simulated time-averaged (a) solid volume fraction, (b) solid axial velocity, and (c) granular temperature compared to experimental data.

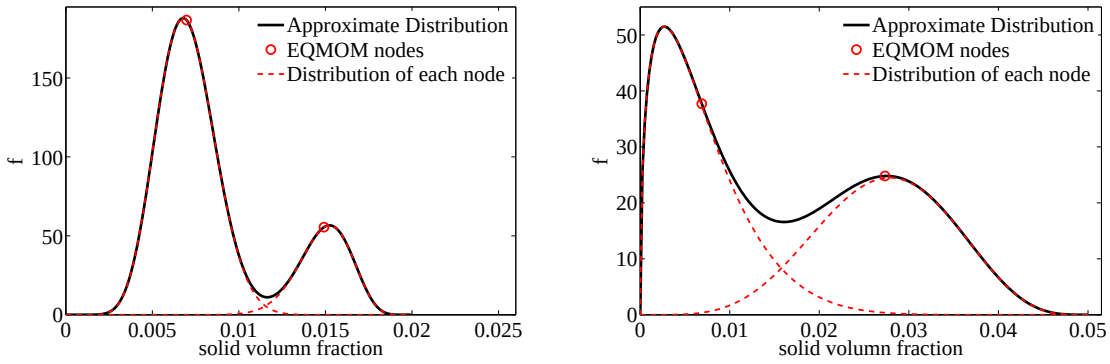

(a) location 1 (b) location 2

Figure 5.6 Reconstructed distribution of the solid volume fraction at different locations.

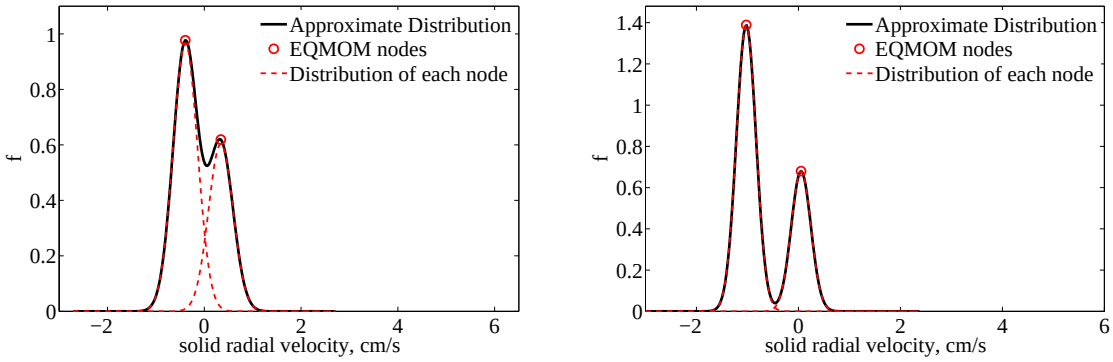

(a) location 1 (b) location 2

Figure 5.7 Reconstructed distribution of the solid radial velocity at different locations.

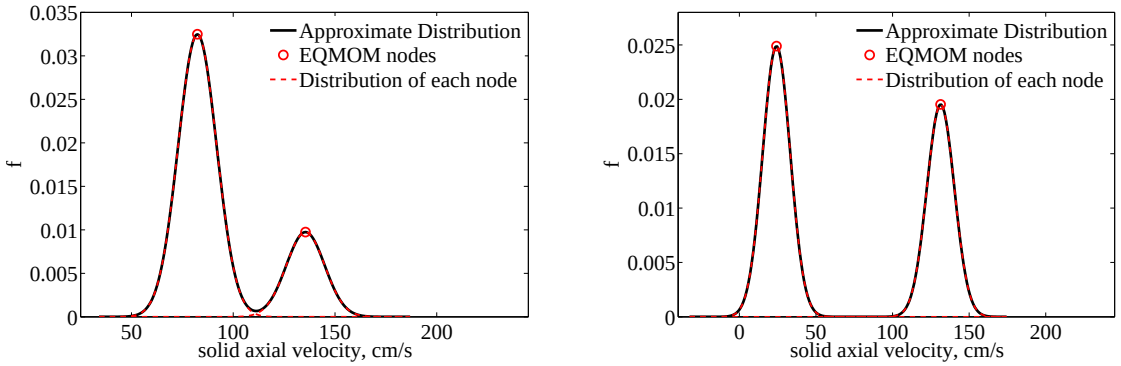

(a) location 1 (b) location 2

Figure 5.8 Reconstructed distribution of the solid axial velocity at different locations.

tioin 1), low solid axial velocity is clearly preferred, while near the wall low velocity just has a bit larger probability than high velocity.

The distribution of granular temperature is reconstructed using 2-node EQMOM with gamma distribution as the kernel. According to the results shown in Figure 5.9, at both locations, two peaks are formed. One sharp peak with high probability shows up at low granular temperature, while the other broad peak with relatively low probability is formed at high granular temperature.

The joint PDF of solid axial and radial velocities is reconstructed using 4-node Gaussian ECQMOM described in Section 5.2.1, results shown in Figure 5.10. At the centerline (location 1), the peak with highest probability is formed at relatively low solid axial velocity and negative

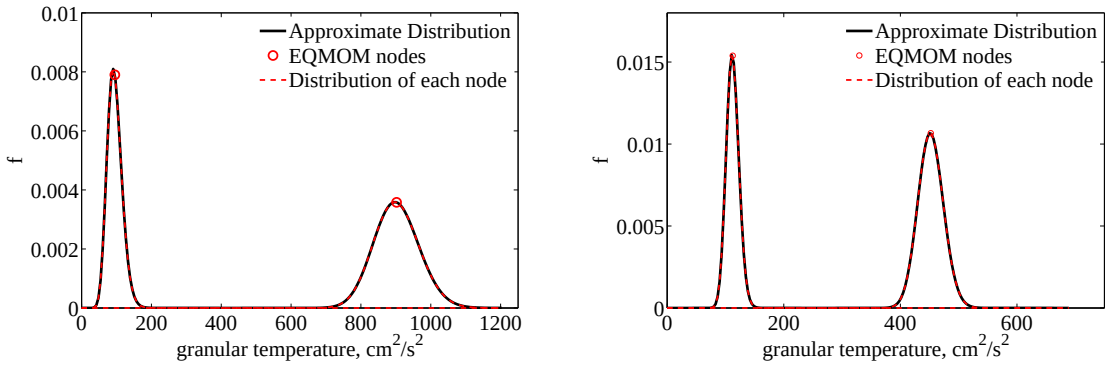

(a) location 1 (b) location 2

Figure 5.9 Reconstructed distribution of the granular temperature at different locations.

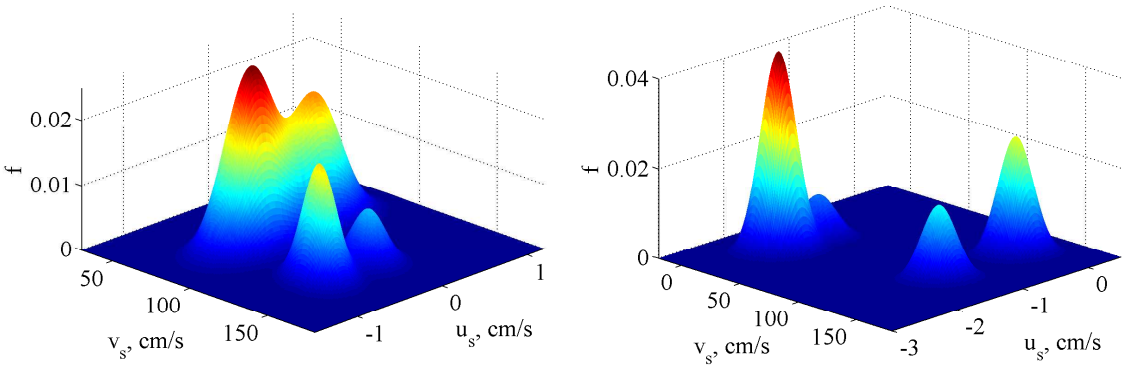

(a) location 1 (b) location 2

Figure 5.10 Reconstructed joint distribution of the solid axial and radial velocities at different locations.

solid radial velocity, which indicates particles tend to move upwards and towards the wall. At location 2, which is near the wall, low solid axial velocity and negative solid radial velocity have the high probability, which means most of the particles are slowly moving upwards towards the wall. However, a relatively strong peak is formed at high axial and positive radial velocity, which indicates some of the particles are moving fast upwards towards the center of the riser.

5.4 Conclusions

A non-intrusive quadrature-based uncertainty quantification approach is applied to a riser flow simulation with particle size as the uncertain input parameter. Contour plots of the mean and standard deviation of the system response including time-averaged solid volume fraction, solid phase velocities, and granular temperature are provided. The effects of uncertain particle diameter on these quantities of interest are studied. The mean values and confidence intervals of the outputs at specific height of the riser are compared to the experimental data provided in the literature. Satisfactory agreement is obtained between the mean values of the simulation results and the experiments. The confidence intervals calculated by the QBUQ approach can cover most of the confidence intervals provided by the experiments. The univariate PDF reconstructions are performed for each system response at specific locations in the computational domain using EQMOM with different kernel density functions. The joint PDF of the solid axial and radial velocities at the same locations are reconstructed as well using Gaussian ECQMOM, which is a combination of EQMOM and CQMOM. The bivariate PDF reconstruction method, Gaussian ECQMOM introduced in this chapter, can be naturally extended to more variables, more nodes for each variable, and other kernel density functions in the future.

CHAPTER 6. SUMMARY AND FUTURE WORK

In this chapter, sub-projects done in previous chapters are summarized, and works can be performed are proposed in future work.

6.1 Summary

The objectives of the project are to develop a non-intrusive quadrature-based uncertainty quantification (QBUQ) approach, and to apply it to multiphase gas-solid flow simulations. The approach relies on Gaussian quadrature formulae and conditional quadrature method of moments (CQMOM) to generate a set of samples for the distribution of the uncertain parameters. Simulations are performed for each sample, and the moments of the system response can be evaluated directly using quadrature rules. With these moments, low order statistics such as mean, variance, skewness, and kurtosis of the system response can be calculated so that confidence intervals for the simulation results can be provided. Meanwhile, with the set of moments of the system response, the probability distribution functions (PDFs) of the system response can be reconstructed using extended quadrature method of moments (EQMOM) and extended conditional quadrature method of moments (ECQMOM). Thus the probability especially of the rare events can be evaluated.

In Chapter 2, the QBUQ approach is described in detail for a univariate case in terms of the random input parameter. The approach significantly reduces the number of samples required to predict the moments of a given order. Beta EQMOM is described in the chapter to illustrate the PDF reconstruction method. The QBUQ approach with the reconstruction of the PDF of the system response is demonstrated by considering a developing channel flow with uncertain viscosity and an oblique shock problem with uncertain inlet Mach number. In the developing

channel flow, we observe that twenty samples are sufficient to calculate moments of order 1 to 4 with an accuracy higher than 10^{-8}, moments of order 5 to 9 are predicted with an absolute error of magnitude 10^{-8}. Using a significantly higher number (like 1000) of samples does not lead to a significant reduction of the error affecting the highest order moments. The approximate distributions of the axial velocity at two different locations show great agreement with the histograms, and four EQMOM nodes are sufficient to reconstruct the axial velocity distribution. In the oblique shock problem, a shock discontinuity is observed with a range of angle with respect to horizontal because of the uncertain input Mach number. The estimation of the shock angle range with QBUQ matches the analytical value with an error on the order of 0.1 degrees. The approximate distributions of the horizontal velocity below the shock show good agreement with histograms. Satisfactory distributions of the horizontal velocity in the shock region are obtained, although some oscillations are formed because of the steep discontinuities presented in the distributions that are being reconstructed. The reconstruction of the distribution in the shock region improves when the number of EQMOM nodes increases, but not significantly. Four nodes are adequate to reconstruct the horizontal velocity distributions in this case.

In Chapter 3, the QBUQ approach with reconstruction of the PDF of the system response is applied to a bubbling fluidized bed. The approach is implemented into MFIX by two separate modules developed based on the Python programming language and shell scripts. The script in the pre-processing module identifies the properties of the input parameters, and generates corresponding MFIX input files for each sample. Once simulations for all samples are completed, the post-processing module extracts time-averaged quantities of interest for each sample, computes the set of the moments, calculates low order statistics such as mean and variance, and reconstruct the PDF of the system response. The distribution of the uncertain input parameter (particle size) of the bubbling fluidized bed is assumed to be uniform distribution, and twenty samples are generated. The effects of uncertain particle size on the solid volume fraction, gas pressure, and vertical solid velocity are studied. Contour plots of mean, variance, and moments up to fourth order of the response indicate that the influences of uncertain particle size concentrate on the interface of the bed, in particular on locations near the wall. Approximated distributions of the response are reconstructed at two different locations.

In Chapter 4, the QBUQ approach is extended to problems with multiple uncertain input parameters. CQMOM is used to sample the space of the uncertain parameters, and is explained by using a bivariate problem as an example. The moments of the system response are directly estimated using Gaussian quadrature formulae, and are used to reconstruct an approximate distribution of the response using EQMOM. The approach is demonstrated by considering a bubbling fluidized bed with two uncertain parameters (particle-wall restitution coefficient and particle-particle restitution coefficient). Contour plots of the mean and standard deviation of solid volume fraction, gas pressure, and solid horizontal and vertical velocities are shown. Circulations of particles are formed in the bed. The effect of uncertain parameters on the solid volume fraction mainly focuses on the interface of the bed, especially on the locations near the wall, and also at the center of the fluidized bed. For gas pressure, the influence of uncertain parameters focuses on the center of the bed. The uncertain parameters influence the solid horizontal velocity the most near the interface of the bed and at the bottom of the bed, and affect the solid vertical velocity the most near the wall. The mean value and 95% confidence interval of the system response at specific locations are compared to the values obtained from small-scale challenge problem. The mean values of the simulation results are in fair agreement with experiment. The confidence intervals obtained from the simulation results sometimes cannot cover the confidence intervals provided by the experiment, which may be caused by uncertainty introduced by other parameters besides the two parameters studied in this work. The measurement method may also result in large confidence intervals for experimental data. The PDF of the system response is reconstructed at four different locations in the computational domain using EQMOM with appropriate kernel density functions.

In Chapter 5, the QBUQ approach is applied to a riser flow simulation with particle diameter considered as the uncertain input parameter. In total 20 samples are generated, and the results of each sample are used to directly estimate the moments of the system response. Contour plots of the mean and standard deviation of time-averaged solid volume fraction, solid phase velocities, and granular temperature are provided. Core-annular structure is observed as expected. For solid volume fraction, the effect of uncertain particle size focuses on the bottom of the riser, the annulus, and some spots near the wall at very high positions of the

riser. The influence of uncertain particle size on solid radial velocity concentrates mainly on the upper part of the riser and slightly on the locations near the inlet of the riser. For solid axial velocity, the uncertain parameter has more effect in the annulus than in the core. And for granular temperature, the influence of uncertain particle size mainly focuses on the core region, especially on the lower part of the core. The mean values and confidence intervals of the outputs at specific height of the riser are compared to the experimental data provided in the literature. Satisfactory agreement is obtained between the mean values of the simulation results and the experiments. The confidence intervals calculated by the QBUQ approach can cover most of the confidence intervals provided by the experiments. The univariate PDF reconstructions are performed for each system response at specific locations in the computational domain using EQMOM with different kernel density functions. The joint PDF of the solid axial and radial velocities at the same locations are reconstructed as well using Gaussian ECQMOM, which is a combination of EQMOM and CQMOM.

6.2 Future Work

Study on uncertainty quantification in multiphase CFD simulations is at its initial level. The QBUQ approach proposed here is applied just to bubbling fluidized beds and riser flows. The approach needs to be tested on other types of multiphase flows. Eventually, the goal is to provide confidence for simulation results of multiphase CFD, which is a very challenging task. For complex models like those for multiphase flows, intrusive UQ approach is hardly to implement. Therefore, non-intrusive UQ approach is nearly the only choice. This leaves the problem to the sampling approaches. Deterministic sampling approaches suffer from the curse of dimensionality while random sampling approaches require too many samples. Reducing the number of samples required for a given accuracy will be a long-term task. A compromising way is to study the most influential parameters first to reduce the number of uncertain input parameters, which needs proper methods to decide which parameters are indeed the most influential. For the post-processing of the UQ data, especially for the reconstruction of the PDF of the system response, the proposed method EQMOM for univariate problem in this thesis has been extended to a bivariate problem using Gaussian ECQMOM. This method can

be extended to more variables and other kernel density functions. Comparisons of EQMOM and ECQMOM to other PDF reconstruction approaches can also be studied in the future.

APPENDIX A. DETERMINATION OF QUADRATURE WEIGHTS AND NODES

The determination of Gaussian quadrature weights and nodes is based on the consideration that monic orthogonal polynomials are defined by a recurrence relation in the form [29, 42]

$$\begin{aligned} &Q_{-1}(\xi) = 0, \\ &Q_0(\xi) = 1, \\ &Q_{r+1}(\xi) = (\xi - \alpha_r)Q_r(\xi) - \beta_r Q_{r-1}(\xi),\ \beta_r > 0. \end{aligned} \tag{A.1}$$

The eigenvalues of the symmetric tridiagonal matrix

$$\mathbf{J}_{\mathrm{M}} = \begin{pmatrix} \alpha_0 & \sqrt{\beta_1} & & & 0 \\ \sqrt{\beta_1} & \alpha_1 & \sqrt{\beta_2} & & \\ & \ddots & \ddots & \ddots & \\ & & \sqrt{\beta_{\mathrm{M}-2}} & \alpha_{\mathrm{M}-2} & \sqrt{\beta_{\mathrm{M}-1}} \\ 0 & & & \sqrt{\beta_{\mathrm{M}-1}} & \alpha_{\mathrm{M}-1} \end{pmatrix}, \tag{A.2}$$

called a Jacobi matrix, are the quadrature nodes of the M-points Gauss quadrature formula, whose weight function is orthogonal to the polynomials defined by the recurrence relation Eq. A.1. The corresponding quadrature weights are given by

$$w_i = \beta_0 v_{i,1}^2,\ i = 1, \ldots, \mathrm{M}, \tag{A.3}$$

where $v_{i,1}$ is the first component of the eigenvector $\mathbf{v}_i$ of $\mathbf{J}_{\mathrm{M}}$, and

$$\beta_0 = \int_I w(\xi)\mathrm{d}\xi,$$

being I the integration interval under consideration.

APPENDIX B. INTRODUCTION OF DIRECT QUADRATURE BASED UNCERTAINTY QUANTIFICATION APPROACH

The main results reported in Yoon et al. are summarized here to introduce the method and to explain how to estimate the required number of samples [4, 119].

B.1 Direct Quadrature Approach to Compute Moments of System Response

The direct quadrature approach is proposed based on using Gaussian quadrature formulae to compute integrals. A one-dimensional integral with form

$$\int_a^b f(x)w(x)\mathrm{d}x$$

can be approximated by a Gaussian quadrature formula with M nodes as

$$\int_a^b f(x)w(x)\mathrm{d}x \approx \sum_{i=1}^{M} f(x_i)w_i, \tag{B.1}$$

where x_i is the i^{th} root of the orthogonal polynomials with corresponding weight function $w(x)$, which is 1 for Gauss-Legendre quadrature, e^{-x^2} for Gauss-Hermite quadrature, and $1/\sqrt{1-x^2}$ for Gauss-Chebyshev quadrature. If $f(x)$ is continuous on the interval $[a, b]$, when $M \to \infty$, the approximation in Eq. B.1 converges to the integral.

The error of Eq. B.1 for $f(x) \in C^{2M}([a, b])$ is given as

$$E = \frac{f^{2M}(\zeta)}{(2M)!}\langle \Phi_M, \Phi_M \rangle, \tag{B.2}$$

where $f^{2M}(\zeta)$ is the $2M$-th derivative of f, $\zeta \in [a, b]$, and $\langle \Phi_M, \Phi_M \rangle$ is the inner product of the M-th order polynomial orthogonal to the weight function $w(x)$. Eq. B.2 shows that for a polynomial of order up to $2M - 1$, M-node Gauss quadrature is exact.

Using Gaussian quadrature formulae, the n-th order moment of a random process u with a single random variable ξ can be approximated as

$$\langle u^n(\xi)\rangle = \int_a^b u(\xi)^n p(\xi)\mathrm{d}\xi \approx \sum_{i=1}^{M} u(\xi_i)^n w_i, \tag{B.3}$$

where ξ_i are the quadrature nodes, w_i are the quadrature weights, and $p(\xi)$ is the weight function. The type of quadrature depends on the distribution of the random varible ξ, for example, Gauss-Hermite quadrature for Gaussian distribution and Gauss-Legendre quadrature for uniform distribution. Finally, for a given distribution $p(\xi)$ without existing quadrature rules, the moments can be approximated as

$$\begin{aligned}\langle u^n(\xi)\rangle &= \int_a^b u(\xi)^n p(\xi)\mathrm{d}\xi \\ &= \int_c^d u(\xi)^n \frac{p(\xi)}{f(\xi)} f(\xi)\mathrm{d}\xi \\ &\approx \sum_{i=1}^{M} \frac{u(\xi_i)^n}{f(\xi_i)} p(\xi_i) w_i,\end{aligned} \tag{B.4}$$

where the integration interval $[c, d]$ is the support of the distribution $f(\xi)$ which has an existing quadrature rule, and ξ_i and w_i are the corresponding quadrature nodes and weights.

B.2 Polynomial Chaos Expansion and Estimation of the Required Number of Samples

In the polynomial chaos approach, a random process u with a single random variable ξ can be approximated as a truncated Fourier series,

$$u(\xi) \approx \sum_{j=0}^{P} u_j \Psi_j(\xi), \tag{B.5}$$

where Ψ_j are orthogonal polynomials corresponding to the distribution of the random input variable, and the coefficients u_j can be computed as

$$u_j = \frac{\langle u(\xi), \Psi_j(\xi)\rangle}{\langle \Psi_j(\xi), \Psi_j(\xi)\rangle}. \tag{B.6}$$

The n-th order moment of u can be expressed using a Gaussian quadrature formula as

$$\langle u(\xi)^n\rangle \approx \sum_{l=1}^{M} \left[\sum_{j=1}^{P} \left(\frac{\sum_{i=1}^{M} u(\xi_i)\Psi_j(\xi_i) w_i}{\langle \Psi_j, \Psi_j\rangle} \right) \Psi_j(\xi_l) \right]^n w_l. \tag{B.7}$$

Based on the properties of Gaussian quadrature formulae, a proposition is proposed by Yoon et al. [4,119] to estimate the required number of samples to compute the exact moments of the system response. For a single variable random process $u(\xi)$ represented by a polynomial of order up to q, at least M samples are required to compute the exact n-th order moment for a P-th order polynomial chaos approximation to u, and M is given as

$$M = \max\left(\frac{q+P+1}{2}, \frac{nq+1}{2}\right). \tag{B.8}$$

The mathematical reasoning for this proposition is the following:

1. To compute coefficient u_{P+1} using Eq. B.6, an integrand of order $q+P$ must be integrated, which is exact if $q+P \leq 2M-1$ or $M \geq (q+P+1)/2$ according to Eq. B.2.

2. By Eq. B.2, the n-th order moment of u computed using direct quadrature approach shown in Eq. B.3 is exact if $nq \leq 2M-1$ or $M \geq (nq+1)/2$.

3. If M is the maximum of $(q+P+1)/2$ and $(nq+1)/2$, both Eqs. B.3 and B.7 are equalities. Therefore, Eqs. B.3 and B.7 are equivalent, which indicates the n-th order moment obtained from direct quadrature and polynomial chaos expansion are equivalent.

4. From the three steps above, the proposed proposition can be derived.

APPENDIX C. PDF RECONSTRUCTION USING EQMOM

The basic idea of EQMOM is to write the PDF $p(\kappa)$ as a weighted sum of N non-negative kernel density functions [14, 121]:

$$f_N(\kappa) = \sum_{i=1}^{N} \rho_i \delta_\sigma(\kappa, \kappa_i), \tag{C.1}$$

where ρ_i and κ_i are the quadrature weights and abscissae used in EQMOM, and $\delta_\sigma(\kappa, \kappa_i)$ is a kernel density function related to the parameter σ, which is selected based on the nature of the distribution that needs to be reconstructed, especially based on the support of the distribution. In the rest of this appendix, the algorithms for EQMOM using different kernel density functions are discussed.

C.1 Beta EQMOM

The beta kernel function is defined as Eq. C.2 for $\zeta \in [0, 1]$ [121],

$$\delta_\sigma(\zeta, \zeta_i) = \frac{\zeta^{\lambda_i - 1} (1 - \zeta)^{\phi_i - 1}}{B(\lambda_i, \phi_i)} \tag{C.2}$$

where $\lambda_i = \zeta_i/\sigma$, $\phi_i = (1 - \zeta_i)/\sigma$, and $B(\lambda_i, \phi_i)$ is the beta function defined as $B(x, y) = \int_0^1 t^{x-1}(1-t)^{y-1}\mathrm{d}t$. The distribution of the system response can be then represented as

$$f_N(\zeta) = \sum_{i=1}^{N} \rho_i \delta_\sigma(\zeta, \zeta_i) = \sum_{i=1}^{N} \rho_i \frac{\zeta^{\lambda_i - 1} (1 - \zeta)^{\phi_i - 1}}{B(\lambda_i, \phi_i)}. \tag{C.3}$$

The n-th order integer moments of $\delta_\sigma(\zeta, \zeta_i)$ can be written in a recursion form:

$$m_n^{(i)} = \frac{\zeta_i + (n-1)\sigma}{1 + (n-1)\sigma} m_{n-1}^{(i)} \text{ for } n > 0, \tag{C.4}$$

and $m_0^{(i)} = 1$.

Thus the integer moments of the distribution function p can be expressed as

$$m_n = \sum_{i=1}^{N} \rho_i m_n^{(i)} = \sum_{i=1}^{N} \rho_i G_n(\zeta_i, \sigma),$$

with

$$G_n(\zeta_i, \sigma) = \begin{cases} 1 & n = 0 \\ \prod_{i=0}^{n-1} \dfrac{\zeta_i + i\sigma}{1 + i\sigma} & n \geq 1 \end{cases}. \tag{C.5}$$

A lower triangular system can be defined to find σ by rewriting these moments as

$$m_n = \eta_n m_n^* + \eta_{n-1} m_{n-1}^* + \ldots + \eta_1 m_1^*, \ \eta_n \geq 0 \tag{C.6}$$

where the non-negative coefficients η_n depend only on σ, and $m_n^* = \sum_{i=1}^{N} \rho_i \zeta_i^n$. The matrix form of the system is $\mathbf{A}(\sigma)\mathbf{m}^* = \mathbf{m}$, where $\mathbf{A}(\sigma)$ is a lower triangular matrix. The quadrature weights ρ_i and nodes ζ_i can be found from the first $2N$ moments $(m_0^*, \ldots, m_{2N-1}^*)$ using the moment-inversion algorithm, Wheeler algorithm [113, 120]. The parameter σ is found using an iterative procedure described in C.4. The scalar function defined to reflect the difference between the original moment m_{2N} and the approximated moment m_{2N}^* for beta EQMOM is

$$J_N(\sigma) = m_{2N} - \eta_{2N} m_{2N}^* - \eta_{2N-1} m_{2N-1}^* + \ldots - \eta_1 m_1^*. \tag{C.7}$$

A transformation and a normalization process are required in order to extend the approach presented above to the general bounded interval $[a, b]$. For such a purpose, let $\kappa = (b-a)\zeta + a$, where $\zeta \in [0, 1]$ with the distribution shown in Eq. C.3. Then the normalized distribution for κ in bounded interval $[a, b]$ is

$$f_N(\kappa) = \frac{1}{b-a} \sum_{i=1}^{N} \rho_i \frac{\left(\frac{\kappa - a}{b-a}\right)^{\lambda_i - 1} \left(\frac{b-\kappa}{b-a}\right)^{\phi_i - 1}}{B\left(\lambda_i, \phi_i\right)}. \tag{C.8}$$

C.2 Gamma EQMOM

A gamma distribution is selected as the kernel function for $\zeta \in \mathbb{R}_0^+$ [121]:

$$\delta_\sigma(\zeta, \zeta_i) = \frac{\zeta^{\lambda_i - 1}\, \mathrm{e}^{-\zeta/\sigma}}{\Gamma(\lambda_i)\sigma^{\lambda_i}}, \tag{C.9}$$

where $\lambda_i = \zeta_i/\sigma$. Using Eq. C.9, the approximated PDF of ζ can be expressed as

$$f_N(\zeta) = \sum_{i=1}^{N} \rho_i \delta_\sigma(\zeta, \zeta_i) = \sum_{i=1}^{N} \rho_i \frac{\zeta^{\lambda_i - 1}\, \mathrm{e}^{-\zeta/\sigma}}{\Gamma(\lambda_i)\sigma^{\lambda_i}}. \tag{C.10}$$

The n-th order integer moment of the kernel density $\delta_\sigma(\zeta, \zeta_i)$ is

$$m_n^{(i)} = \frac{\Gamma(\lambda_i + n)}{\Gamma(\lambda_i)} \left(\frac{\zeta_i}{\lambda_i}\right)^n. \tag{C.11}$$

As a consequence, the integer moments of p can be written as

$$m_n = \sum_{i=1}^{N} \rho_i \frac{\Gamma(\lambda_i + n)}{\Gamma(\lambda_i)} \sigma^n = \sum_{i=1}^{N} \rho_i G_n(\zeta_i, \sigma), \tag{C.12}$$

where

$$G_n(\kappa_i, \sigma) = \begin{cases} 1 & n = 0 \\ \prod_{i=0}^{n-1} (\zeta_i + i\sigma) & n \geq 1 \end{cases}. \tag{C.13}$$

The lower triangular system of equations used to find σ is defined as:

$$m_n = m_n^* + \sum_{i=1}^{N} \rho_i P_{n-1}(\zeta_i, \sigma), \tag{C.14}$$

where $m_n^* = \sum_{i=1}^{N} \rho_i \zeta_i^n$ and P_{n-1} is a homogeneous polynomial of order $n-1$. The parameter σ is then determined by solving the system in Eq. C.14 iteratively with the algorithm described in C.4. The scalar function for gamma EQMOM is

$$J_N(\sigma) = m_{2N} - m_{2N}^* - \sum_{i=1}^{N} \rho_i P_{2N-1}(\zeta_i, \sigma).$$

For cases where $\kappa \in [a, +\infty[$ instead of $\mathbb{R}_0^+$, a linear change of variables is applied so that the approach is extended to the general interval. This is achieved by letting $\kappa = \zeta + a$, where $\zeta \in \mathbb{R}_0^+$ with PDF in Eq. C.10. The final generalized PDF for κ on the semi-infinite interval $[a, +\infty[$ is

$$f_N(\kappa) = \sum_{i=1}^{N} \rho_i \frac{(\kappa - a)^{\lambda_i - 1}\, \mathrm{e}^{-(\kappa - a)/\sigma}}{\Gamma(\lambda_i)\sigma^{\lambda_i}}. \tag{C.15}$$

C.3 Gaussian EQMOM

For $\kappa \in \mathbb{R}$, a Gaussian distribution is selected as the kernel density function [14]:

$$\delta_\sigma(\kappa, \kappa_i) = \frac{1}{\sigma\sqrt{2\pi}} \exp\left[-\frac{(\kappa - \kappa_i)^2}{2\sigma^2}\right]. \tag{C.16}$$

The approximated PDF of κ can be written as Eq. C.17 using Eq. C.16:

$$f_N(\kappa) = \sum_{i=1}^{N} \rho_i \delta_\sigma(\kappa, \kappa_i) = \sum_{i=1}^{N} \frac{\rho_i}{\sigma\sqrt{2\pi}} \exp\left[-\frac{(\kappa - \kappa_i)^2}{2\sigma^2}\right]. \tag{C.17}$$

The n-th order integer moment of the kernel density $\delta_\sigma(\kappa, \kappa_i)$ can be calculated from the moment generation function:

$$m_n^{(i)} = M_n^{(i)}\Big|_{t=0} = \frac{\mathrm{d}^n M^{(i)}}{\mathrm{d}t^n}\bigg|_{t=0}, \tag{C.18}$$

where the moment generation function $M^{(i)}(t)$ for Gaussian distribution is defined as

$$M^{(i)}(t) = \exp\left(\kappa_i t + \frac{1}{2}\sigma^2 t^2\right).$$

The first five integer moments of the kernel density function ($n \leq 4$) are shown in Eq. C.19.

$$\begin{aligned} m_0^{(i)} &= 1 \\ m_1^{(i)} &= \kappa_i \\ m_2^{(i)} &= \kappa_i^2 + \sigma^2 \\ m_3^{(i)} &= \kappa_i^3 + 3\kappa_i\sigma^2 \\ m_4^{(i)} &= \kappa_i^4 + 6\kappa_i^2\sigma^2 + 3\sigma^4. \end{aligned} \tag{C.19}$$

Therefore, the integer moments of p can be written as a lower triangular system:

$$m_n = m_n^* + \sum_{i=1}^{N} \rho_i P_{n-1}(\kappa_i, \sigma), \tag{C.20}$$

where $m_n^* = \sum_{i=1}^{N} \rho_i \kappa_i^n$ and P_{n-1} is a homogeneous polynomial of order $n-1$. For $n \leq 4$, the lower triangular system is

$$\begin{aligned} m_0 &= m_0^* \\ m_1 &= m_1^* \\ m_2 &= m_2^* + \sigma^2 m_0^* \\ m_3 &= m_3^* + 3\sigma^2 m_1^* \\ m_4 &= m_4^* + 6\sigma^2 m_2^* + 3\sigma^4 m_0^*. \end{aligned} \tag{C.21}$$

By solving the system in Eq. C.20 iteratively using the algorithm in the next section, the parameter σ is determined. The scalar function for Gaussian EQMOM is

$$J_N(\sigma) = m_{2N} - m^*_{2N} - \sum_{i=1}^{N} \rho_i P_{2N-1}(\kappa_i, \sigma).$$

C.4 The Algorithm to Solve for σ

The following algorithm is used to solve the lower triangular systems shown in Eq. C.6, Eq. C.14, and Eq. C.20.

1. Guess the value of σ

2. Compute the moments m^*_n from the lower triangular system

$$\mathbf{m} = \mathbf{A}(\sigma)\mathbf{m}^*$$

3. Use the adaptive Wheeler algorithm to find weights ρ_i and abscissae κ_i from $\mathbf{m}^*$

4. Compute m^*_{2N} using weights and abscissae found in the last step

5. Compute the scalar function $J_N(\sigma)$

6. If $J_N(\sigma) \neq 0$, guess a new σ and iterate from step 1.

BIBLIOGRAPHY

[1] K. Agrawal, P. N. Loezos, M. Syamlal, and S. Sundaresan. The role of meso-scale structures in rapid gassolid flows. *Journal of Fluid Mechanics*, 445:151–185, 2001.

[2] R. Askey and J. A. Wilson. *Some basic hypergeometric polynomials that generalize Jacobi polynomials*. Number 319 in Memoirs of the American Mathematical Society. Providence, R.I., U.S.A.: American Mathematical Society, 1985.

[3] B. V. Asokan and N. Zabaras. Using stochastic analysis to capture unstable equilibrium in natural convection. *Journal of Computational Physics*, 208(1):134–153, September 2005.

[4] P. J. Attar and P. Vedula. On convergence of moments in uncertainty quantification based on direct quadrature. *Reliability Engineering & System Safety*, 111(0):119 – 125, 2013.

[5] A. A. Avidan. Fluid catalytic cracking. In J. R. Grace, A. A. Avidan, and T. M. Knowlton, editors, *Circulating Fluidized Beds*, chapter 13, pages 466–488. Blackie Academic & Professional, London, first edition, 1997.

[6] I. Babuška, F. Nobile, and R. Tempone. A stochastic collocation method for elliptic partial differential equations with random input data. *SIAM Review*, 52(2):317–355, 2010.

[7] P. Basu. Combustion of coal in circulating fluidized-bed boilers: a review. *Chemical Engineering Science*, 54(22):5547–5557, 1999.

[8] P. Basu. *Combustion and Gasification in Fluidized Beds*. Hoboken CRC Press, 2006.

[9] S. Benyahia, M. Syamlal, and T. J. O'Brien. *Summary of MFIX Equations 2012-1.* From URL https://mfix.netl.doe.gov/documentation/MFIXEquations2012-1.pdf, January 2012.

[10] R. B. Bird, W. E. Stewart, and E. N. Lightfoot. *Transport Phenomena.* John Wiley & Sons, New York, USA, 2007.

[11] J. P. Boyd. The rate of convergence of Hermite function series. *Mathematics of Computation*, 35:1309–1316, 1980.

[12] C. Brereton. Combustion performance. In J. R. Grace, A. A. Avidan, and T. M. Knowlton, editors, *Circulating Fluidized Beds*, chapter 10, pages 369–416. Blackie Academic & Professional, London, first edition, 1997.

[13] R. H. Cameron and W. T. Martin. The orthogonal development of non-linear functionals in series of Fourier-Hermite functionals. *Annals of Mathematics*, 48(2):385–392, 1947.

[14] C. Chalons, R. O. Fox, and M. Massot. A multi-Gaussian quadrature method of moments for gas-particle flows in a LES framework. In *Proceedings of the Summer Program*, pages 347 – 358. Center for Turbulence Research, Stanford University, 2010.

[15] Q.-Y. Chen, D. Gottlieb, and J. S. Hesthaven. Uncertainty analysis for the steady-state flows in a dual throat nozzle. *Journal of Computational Physics*, 204(1):378–398, 20 March 2005.

[16] Committee on Mathematical Foundations of Verification, Validation, and Uncertainty Quantification, Board on Mathematical Sciences and Their Applications, Division on Engineering and Physical Sciences, and National Research Council (US). *Assessing the Reliability of Complex Models: Mathematical and Statistical Foundations of Verification, Validation, and Uncertainty Quantification.* National Academies Press, 2012.

[17] B. J. Debusschere, H. N. Najm, A. Matta, O. M. Knio, R. G. Ghanem, and O. P. Le Maître. Protein labeling reactions in electrochemical microchannel flow: Numerical simulation and uncertainty propagation. *Physics of Fluids*, 15(8):2238–2250, 2003.

[18] N. G. Deen, M. van Sint Annaland, M. A. van der Hoef, and J. A. M. Kuipers. Review of discrete particle modeling of fluidized beds. *Chemical Engineering Science*, 62(1-2):28–44, January 2007.

[19] H. Dette and W. J. Studden. *The Theory of Canonical Moments with Applications in Statistics, Probability and Analysis*. Wiley, 1997.

[20] A. Donato and R. Pitchumani. QUICKER: Quantifying Uncertainty In Computational Knowledge Engineering Rapidly–A rapid methodology for uncertainty analysis. *Powder Technology*, 2014.

[21] D. A. Drew. Mathematical modeling of two-phase flow. *Annual review of fluid mechanics*, 15(1):261–291, 1983.

[22] R. J. Dry and C. J. Beeby. Applications of CFB technology to gas-solid reactions. In J. R. Grace, A. A. Avidan, and T. M. Knowlton, editors, *Circulating Fluidized Beds*, chapter 12, pages 441–465. Blackie Academic & Professional, London, first edition, 1997.

[23] H. Enwald, E. Peirano, and A.-E. Almstedt. Eulerian two-phase flow theory applied to fluidization. *International Journal of Multiphase Flow*, 22:21–66, December 1996.

[24] J. Faragher. Probabilistic methods for the quantification of uncertainty and error in computational fluid dynamics simulations. Technical Report DSTO-TR-1633, Australian Government, Department of Defence, Defence Science and Technology Organisation, 2004.

[25] J. H Ferziger and M. Peric. *Computational Methods for Fluid Dynamics*. Springer, 2002.

[26] B. Ganapathysubramanian and N. Zabaras. Modeling diffusion in random heterogeneous media: Data-driven models, stochastic collocation and the variational multiscale method. *Journal of Computational Physics*, 226(1):326–353, September 2007.

[27] B. Ganapathysubramanian and N. Zabaras. Sparse grid collocation schemes for stochastic natural convection problems. *Journal of Computational Physics*, 225(1):652–685, July 2007.

[28] X. Gao, L.-J. Wang, C. Wu, Y.-W. Cheng, and X. Li. Steady-state simulation of core-annulus flow in a circulating fluidized bed (CFB) riser. *Chemical Engineering Science*, 78(20):98–110, 2012.

[29] W. Gautchi. *Orthogonal Polynomials: Computation and Approximation*. Oxford University Press, USA, 2004.

[30] A. Gel, K. Chaudhari, R. Turton, and P. Nicoletti. Application of uncertainty quantification methods for coal devolatilization kinetics in gasifier modeling. *Powder Technology*, 265:66–75, 2014.

[31] A. Gel, R. Garg, C. Tong, M. Shahnam, and C. Guenther. Applying uncertainty quantification to multiphase flow computational fluid dynamics. *Powder Technology*, 242:27–39, July 2013.

[32] A. Gel, T. Li, B. Gopalan, M. Shahnam, and M. Syamlal. Validation and uncertainty quantification of a multiphase computational fluid dynamics model. *Industrial & Engineering Chemistry Research*, 52(33):11424–11435, 6 May 2013.

[33] S. J. Gelderbloom, D. Gidaspow, and R. W. Lyczkowski. CFD simulations of bubbling/collapsing fluidized beds for three Geldart groups. *AIChE journal*, 49(4):844–858, April 2003.

[34] T. Gerstner and M. Griebel. Numerical integration using sparse grids. *Numerical Algorithms*, 18(3-4):209–232, January 1998.

[35] R. Ghanem. Hybrid stochastic finite elements and generalized Monte Carlo simulation. *Journal of Applied Mechanics*, 65(4):1004–1009, 1 December 1998.

[36] R. Ghanem. Probabilistic characterization of transport in heterogeneous media. *Computer Methods in Applied Mechanics and Engineering*, 158(3):199–220, 1998.

[37] R. Ghanem and S. Dham. Stochastic finite element analysis for multiphase flow in heterogeneous porous media. *Transport in Porous Media*, 32(3):239–262, 1998.

[38] R. Ghanem and P. D. Spanos. *Stochastic Finite Elements: A Spectral Approach*. Springer-Verlag, New York, 1991.

[39] D. Ghiocel and R. Ghanem. Stochastic finite-element analysis of seismic soil-structure interaction. *Journal of Engineering Mechanics*, 128(1):66–77, January 2002.

[40] D. Gidaspow. *Multiphase flow and fluidization: continuum and kinetic theory descriptions*. Academic press, 1994.

[41] M. J. V. Goldschmidt, J. A. M. Kuipers, and W. P. M. van Swaaij. Hydrodynamic modelling of dense gas-fluidised beds using the kinetic theory of granular flow: effect of coefficient of restitution on bed dynamics. *Chemical Engineering Science*, 56(2):571–578, 2001.

[42] G. H. Golub and J. H. Welsch. Calculation of Gauss quadrature rules. *Mathematics of Computation*, 23:221–230, 1969.

[43] J. R. Grace and Hsiaotao Bi. Introduction to circulating fluidized beds. In J. R. Grace, A. A. Avidan, and T. M. Knowlton, editors, *Circulating Fluidized Beds*, chapter 1, pages 1–20. Blackie Academic & Professional, London, first edition, 1997.

[44] C. J. Greenshields, H. G. Weller, L. Gasparini, and J. M. Reese. Implementation of semi-discrete, non-staggered central schemes in a colocated, polyhedral, finite volume framework, for high-speed viscous flows. *International Journal for Numerical Methods in Fluids*, 63(1):1–21, 2010.

[45] F. Hernández-Jiménez, S. Sánchez-Delgado, A. Gómez-García, and A. Acosta-Iborra. Comparison between two-fluid model simulations and particle image analysis & velocimetry (piv) results for a two-dimensional gas–solid fluidized bed. *Chemical Engineering Science*, 66(17):3753–3772, 1 September 2011.

[46] S. Hosder, R. W. Walters, and R. Perez. A non-intrusive polynomial chaos method for uncertainty propagation in CFD simulations. In *In Proceedings of the 44th AIAA Aerospace Sciences Meeting*, volume 14, pages 10649–10667, 2006.

[47] L. Huyse. Free-form airfoil shape optimization under uncertainty using maximum expected value and second-order second-moment strategies. Technical report, ICASE Report 2001-18, 2001.

[48] L. Huyse. Solving problems of optimization under uncertainty as statistical decision problems. *AIAA Paper 2001-1519*, 2001.

[49] P. C. Johnson and R. Jackson. Frictional-collisional constitutive relations for granular materials, with application to plane shearing. *Journal of Fluid Mechanics*, 176:67–93, March 1987.

[50] O. M. Knio and O. P. Le Maître. Uncertainty propagation in CFD using polynomial chaos decomposition. *Fluid Dynamics Research*, 38(9):616–640, 2006.

[51] D. Kunii and O. Levenspiel. *Fluidization engineering*. Butterworth-Heinemann, Boston, 1991.

[52] W. A. Lane, C. B. Storlie, C. J. Montgomery, and E. M. Ryan. Numerical modeling and uncertainty quantification of a bubbling fluidized bed with immersed horizontal tubes. *Powder Technology*, 253:733–743, 2014.

[53] O. Le Maître, M. T. Reagan, B. Debusschere, H. N. Najm, R. G. Ghanem, and O. M. Knio. Natural convection in a closed cavity under stochastic, non-Boussinesq conditions. *SIAM Journal on Scientific Computing*, 26(2):375–394, 2004.

[54] O. P. Le Maître. Polynomial chaos expansion of a Lagrangian model for the flow around an airfoil. *Comptes Rendus Mécanique*, 334(11):693–699, 2006.

[55] O. P. Le Maître and O. M. Knio. A stochastic particle-mesh scheme for uncertainty propagation in vortical flows. *Journal of Computational Physics*, 226(1):645–671, 2007.

[56] O. P. Le Maître, O. M. Knio, H. N. Najm, and R. G. Ghanem. A stochastic projection method for fluid flow: I. basic formulation. *Journal of Computational Physics*, 173(2):481 – 511, 2001.

[57] O. P. Le Maître, O. M. Knio, H.N. Najm, and R. G. Ghanem. Uncertainty propagation using Wiener-Haar expansions. *Journal of Computational Physics*, 197(1):28–57, 2004.

[58] O. P. Le Maître and P. Knio. *Spectral Methods for Uncertainty Quantification*. Springer, 2010.

[59] O. P. Le Maître, H. N. Najm, P. P. Pebay, R. G. Ghanem, and O. M. Knio. Multi-resolution-analysis scheme for uncertainty quantification in chemical systems. *SIAM Journal on Scientific Computing*, 29(2):864–889, 2007.

[60] O. P. Le Maître, M. T. Reagan, H. N. Najm, R. G. Ghanem, and O. M. Knio. A stochastic projection method for fluid flow: II. random process. *Journal of Computational Physics*, 181(1):9 – 44, 2002.

[61] G. Lin, C.-H. Su, and G. E. Karniadakis. Predicting shock dynamics in the presence of uncertainties. *Journal of Computational Physics*, 217(1):260–276, September 2006.

[62] B. Lockwood and D. Mavriplis. Gradient-based methods for uncertainty quantification in hypersonic flows. *Computers & Fluids*, 85:27–38, 1 October 2013.

[63] Z. Lu and D. Zhang. A comparative study on uncertainty quantification for flow in randomly heterogeneous media using Monte Carlo simulations and conventional and KL-based moment-equation approaches. *SIAM Journal on Scientific Computing*, 26(2):558–577, 2004.

[64] C. K. K. Lun, S. B. Savage, D. J. Jeffrey, and N. Chepurniy. Kinetic theories for granular flow: inelastic particles in Couette flow and slightly inelastic particles in a general flowfield. *Journal of Fluid Mechanics*, 140:223–256, 1984.

[65] X. Ma and N. Zabaras. An adaptive hierarchical sparse grid collocation algorithm for the solution of stochastic differential equations. *Journal of Computational Physics*, 228(8):3084–3113, 1 May 2009.

[66] D. L. Marchisio and R. O. Fox. *Computational Models for Polydisperse Particulate and Multiphase Systems*. Cambridge Series in Chemical Engineering. Cambridge University Press, 2013.

[67] L. Mathelin and M. Hussaini. A stochastic collocation algorithm for uncertainty analysis. Technical Report NASA/CR-2003-212153, NASA, Langley Research Center, Hampton, VA, 2003.

[68] L. Mathelin, M. Hussaini, and T. Zang. Stochastic approaches to uncertainty quantification in CFD simulations. *Numerical Algorithms*, 38(1 – 3):209 – 236, 2005.

[69] L. Mathelin, M. Y. Hussaini, T. A. Zang, and F. Bataille. Uncertainty propagation for a turbulent, compressible nozzle flow using stochastic methods. *AIAA Journal*, 42(8):1669 – 1676, 2004. AIAA-5674-562.

[70] M. D. McKay, R. J. Beckman, and W. J. Conover. Comparison of three methods for selecting values of input variables in the analysis of output from a computer code. *Technometrics*, 21(2):239–245, 1979.

[71] L. R. Mead and N. Papanicolaou. Maximum entropy in the problem of moments. *Journal of Mathematical Physics*, 25(8):2404–2417, 1984.

[72] W. J. Morokoff and R. E. Caflisch. Quasi-Monte Carlo integration. *Journal of Computational Physics*, 122(2):218–230, 1995.

[73] H. N. Najm. Uncertainty quantification and polynomial chaos techniques in computational fluid dynamics. *Annual Review of Fluid Mechanics*, 41(1):35 – 52, 2009.

[74] V. A. B. Narayanan and N. Zabaras. Variational multiscale stabilized FEM formulations for transport equations: stochastic advection-diffusion and incompressible stochastic Navier-Stokes equations. *Journal of Computational Physics*, 202(1):94–133, 2005.

[75] National Energy Technology Laboratory small scale challenge problem (SSCP-I). https://mfix.netl.doe.gov/challenge/index.php. 2013.

[76] F. Nobile and R. Tempone. Analysis and implementation issues for the numerical approximation of parabolic equations with random coefficients. *International Journal for Numerical Methods in Engineering*, 80(6-7):979–1006, November 2009.

[77] F. Nobile, R. Tempone, and C. G. Webster. An anisotropic sparse grid stochastic collocation method for partial differential equations with random input data. *SIAM Journal on Numerical Analysis*, 46(5):2411–2442, 2008.

[78] F. Nobile, R. Tempone, and C. G. Webster. A sparse grid stochastic collocation method for partial differential equations with random input data. *SIAM Journal on Numerical Analysis*, 46(5):2309–2345, 2008.

[79] OpenCFD. *OpenFOAM - The Open Source CFD Toolbox - Programmer's Guide*. OpenCFD Ltd., United Kingdom, 2.2.0 edition, 2013.

[80] OpenCFD. *OpenFOAM - The Open Source CFD Toolbox - User's Guide*. OpenCFD Ltd., United Kingdom, 2.2.0 edition, 2013.

[81] A. Passalacqua and R. O. Fox. Advanced continuum modelling of gas-particle flows beyond the hydrodynamic limit. *Applied Mathematical Modelling*, 35(4):1616–1627, 2011.

[82] A. Passalacqua and R. O. Fox. Simulation of mono- and bidisperse gas-particle flow in a riser with a third-order quadrature-based moment method. *Industrial & Engineering Chemistry Research*, 52(1):187–198, 2013.

[83] A. Passalacqua, R. O. Fox, R. Garg, and S. Subramaniam. A fully coupled quadrature-based moment method for dilute to moderately dilute fluidparticle flows. *Chemical Engineering Science*, 65(7):2267–2283, 2010.

[84] S. V. Patankar. *Numerical Heat Transfer and Fluid Flow*. Hemisphere, Washington D. C., 1980.

[85] J. M. C. Pereira, J. P. Serra e Moura, A. R. Ervilha, and J. C. F. Pereira. On the uncertainty quantification of blood flow viscosity models. *Chemical Engineering Science*, 101:253–265, September 2013.

[86] R. Perez and R. W. Walters. An implicit compact polynomial chaos formulation for the Euler equations. In *Proc., 43rd AIAA Aerospace Sciences Meeting and Exhibit*, pages 2005–1406, 2005.

[87] B. D. Phenix, J. L. Dinaro, M. A. Tatang, J. W. Tester, J. B. Howard, and G. J. McRae. Incorporation of parametric uncertainty into complex kinetic mechanisms: Application to hydrogen oxidation in supercritical water. *Combustion and Flame*, 112(1-2):132 – 146, 1998.

[88] W. H. Press, S. A. Teukolsky, W. T. Vetterling, and B. P. Flannery. *Numerical recipes in C: the art of scientific computing*. Cambridge University Press, 1992.

[89] M. M. Putko, P. A. Newman, L. L. Green, and A. C. Taylor. Approach for input uncertainty propagation and robust design in CFD using sensitivity derivatives. *Journal of Fluids Engineering*, 124(1):60–69, 12 November 2001.

[90] M. T. Reagan, H. N. Najm, B. J. Debusschere, O. P. Le Maître, O. M. Knio, and R. G. Ghanem. Spectral stochastic uncertainty quantification in chemical systems. *Combustion Theory and Modelling*, 8(3):607–632, 2004.

[91] M. T. Reagan, H. N. Najm, R. G. Ghanem, and O. M. Knio. Uncertainty quantification in reacting-flow simulations through non-intrusive spectral projection. *Combustion and Flame*, 132(3):545 – 555, 2003.

[92] M. T. Reagan, H. N. Najm, P. P. Pébay, O. M. Knio, and R. G. Ghanem. Quantifying uncertainty in chemical systems modeling. *International Journal of Chemical Kinetics*, 37(6):368–382, June 2005.

[93] L. Reh. Challenges of circulating fluid-bed reactors in energy and raw materials industries. *Chemical Engineering Science*, 54(22):5359–5368, 1999.

[94] P. J. Roache. Quantification of uncertainty in computational fluid dynamics. *Annual Review of Fluid Mechanics*, 29(1):123 – 160, 1997.

[95] D. G. Schaeffer. Instability in the evolution equations describing incompressible granular flow. *Journal of Differential Equations*, 66(1):19–50, 1987.

[96] J. Sinclair. Hydrodynamic modeling. In J. R. Grace, A. A. Avidan, and T. M. Knowlton, editors, *Circulating Fluidized Beds*, chapter 5, pages 149–180. Blackie Academic & Professional, London, first edition, 1997.

[97] S. A. Smolyak. Quadrature and interpolation formulas for tensor products of certain classes of functions. In *Dokl. Akad. Nauk SSSR*, volume 4, page 123, 1963.

[98] C. Soize and R. G. Ghanem. Physical systems with random uncertainties: chaos representations with arbitrary probability measure. *SIAM Journal on Scientific Computing*, 26(2):395–410, 2004.

[99] M. Syamlal, W. Rogers, and T. J. O'Brien. *MFIX Documentation Theory Guide*. U.S. Department of Energy, Morgantown Energy Technology Center, Morgantown, WV, December 1993.

[100] F. Taghipour, N. Ellis, and C. Wong. Experimental and computational study of gas-solid fluidized bed hydrodynamics. *Chemical Engineering Science*, 60(24):6857–6867, December 2005.

[101] A. Tagliani. Hausdorff moment problem and maximum entropy: A unified approach. *Applied Mathematics and Computation*, 105(2):291–305, November 1999.

[102] M. Tartan and D. Gidaspow. Measurement of granular temperature and stresses in risers. *AIChE Journal*, 50(8):1760–1775, 2004.

[103] A. C. Taylor, L. L. Green, P. A. Newman, and M. M. Putko. Some advanced concepts in discrete aerodynamic sensitivity analysis. *AIAA Journal*, 41(7):1224–1229, July 2003.

[104] Y. Tsuji, T. Kawaguchi, and T. Tanaka. Discrete particle simulation of two-dimensional fluidized bed. *Powder Technology*, 77(1):79–87, October 1993.

[105] M. A. van der Hoef, M. van Sint Annaland, N. G. Deen, and J. A. M. Kuipers. Numerical simulation of dense gas-solid fluidized beds: a multiscale modeling strategy. *Annual Review of Fluid Mechanics*, 40:47–70, January 2008.

[106] M. A. van der Hoef, M. van Sint Annaland, and J. A. M. Kuipers. Computational fluid dynamics for dense gas-solid fluidized beds: A multi-scale modeling strategy. *Chemical Engineering Science*, 59(22-23):5157–5165, 2004.

[107] M. A. van der Hoef, M. Ye, M. van Sint Annaland, A. T. Andrews, S. Sundaresan, and J. A. M. Kuipers. Multiscale modeling of gas-fluidized beds. *Advances in Chemical Engineering*, 31:65–149, 2006.

[108] A. Vié, C. Chalons, R. O. Fox, F. Laurent, and M. Massot. A multi-gaussian quadrature method of moments for simulating high stokes number turbulent two-phase flows. *Center for Turbulence Research Annual Research Briefs*, 2011:309–320, 2011.

[109] R. Walters and L. Huyse. Uncertainty analysis for fluid mechanics with applications. Technical Report ICASE Report No. 2002-1; NASA/CR-2002-211449, Langley Research Center, Hampton, VA, 2002.

[110] X. Wan and G. E. Karniadakis. Multi-element generalized polynomial chaos for arbitrary probability measures. *SIAM Journal on Scientific Computing*, 28(3):901–928, 2006.

[111] C. G. Webster. *Sparse Grid Stochastic Collocation Techniques for the Numerical Solution of Parial Differential Equations with Random Input Data.* PhD thesis, Florida State University, 15 February 2007.

[112] C. Y. Wen and Y. H. Yu. Mechanics of fluidization. In *Chemical Engineering Progress Symposium Series*, volume 62, pages 100–111, 1966.

[113] J. C. Wheeler. Modified moments and Gaussian quadratures. *Rocky Mountain Journal of Mathematics*, 4(2):287–296, 1974.

[114] D. Xiu and J. S. Hesthaven. High-order collocation methods for differential equations with random inputs. *SIAM Journal on Scientific Computing*, 27(3):1118–1139, 2005.

[115] D. Xiu and G. E. Karniadakis. The Wiener-Askey polynomial chaos for stochastic differential equations. *SIAM Journal on Scientific Computing*, 24(2):619–644, 2002.

[116] D. Xiu and G. E. Karniadakis. Modeling uncertainty in flow simulations via generalized polynomial chaos. *Journal of Computational Physics*, 187(1):137–167, 2003.

[117] N. Yang, W. Wang, W. Ge, L. Wang, and J. Li. Simulation of heterogeneous structure in a circulating fluidized-bed riser by combining the two-fluid model with the emms approach. *Industrial & Engineering Chemistry Research*, 43(18):5548–5561, 2004.

[118] W.-C. Yang. *Handbook of fluidization and fluid-particle systems*. Marcel Dekker, New York, 2003.

[119] J. Yoon, P. J. Attar, and P. Vedula. Non-intrusive uncertainty quantification for hypersonic flight using direct quadrature. In *AIAA Guidance, Navigation, and Control Conference*, number AIAA 2010-8171, August 2010.

[120] C. Yuan and R. O. Fox. Conditional quadrature method of moments for kinetic equations. *Journal of Computational Physics*, 230(22):8216–8246, 10 September 2011.

[121] C. Yuan, F. Laurent, and R. O. Fox. An extended quadrature method of moments for population balance equations. *Journal of Aerosol Science*, 51:1–23, 2012.